Recovering The Optical Properties Of A Tissue Using Maximum *A Posteriori* Based Estimation

by

Amaria Zidouk

A thesis submitted to the
University of Birmingham
for the degree of
DOCTOR OF PHILOSOPHY

School of Computer Science
College of Engineering and Physical Sciences
University of Birmingham
January 2014

Abstract

The spectral reflectance of a biological tissue is known to be affected by its physical and optical properties such as thickness, chromophore concentrations and scattering coefficient. There exist numerous methods that aim to extract the optical parameters of a tissue by relating reflectance measurements to a theoretical model of light transport. During the parameter recovery process, assumptions are often made about the characteristics of the tissue. However, incorrect assumptions lead to inaccurate or even erroneous results.

We present a method based on the maximum *a posteriori* estimation technique to recover some optical properties of the biological tissue from reflectance measurements. The method provides correct results even in the presence of significant uncertainty in the underlying specification of the tissue. A light transport model of the inspected medium is developed and used in the estimation process. The analysis of the results obtained from simulated skin data and phantoms suggests that the proposed MAP based method is a good parameter recovery technique that provides accurate estimates and is robust against a high level of uncertainty in the tissue's model.

Acknowledgements

All praise be to Allah, the Beneficent, the Merciful.

Firstly, I would like to thank my parents who have always been supportive and encouraging, and without whom I would never have had the opportunity to complete this research. I would also like to thank my husband for his love, his continuous help and support as well as his much appreciated patience throughout this process.

I thank my supervisor, Dr. Iain B. Styles for his invaluable help and guidance, and for all he taught me during my studies. I also thank my thesis group members Prof. Ela Claridge and Prof. Jon Rowe for the feedback they provided during our meetings, Dr. Hancox for his invaluable support, and Dr. Dzena Hidovic-Rowe for providing me with all the images she used in her research.

Special thanks go to my beautiful aunt Fatima Hida for her love, help and faith in me, my brother Amine for cheering me up when I was down, and my parents-in-law for their love and encouragement. Finally, I would like to thank every friend and family member who has wished me luck along the way, and provided me with encouragement and support when these were most needed.

Contents

List of Figures

Chapter 1

Introduction

Optical techniques have often been used in medical diagnosis. A change in the skin's colour or appearance, for instance, was considered a sign of a number of diseases. The skin of an anaemic patient would become paler while an infected wound would appear as blue or purple. This is due to the fact that the colour of a tissue changes according to alterations in its internal structure. In fact, when light travels through a biological tissue, it undergoes absorption and scattering events that are closely dependent on the structure of the medium. When the light finally exits the medium, we can infer a number of information about the tissue's optical and physiological properties.

There exist many methods that use this knowledge to extract important information that could be used as part of the medical diagnosis process such as blood volume fraction and oxygenation (Kienle and Patterson, 1997; Gebhart et al., 2006; Wang et al., 2008; Palmer et al., 2006; Palmer and Ramanujam, 2006; Prahl, 1995a; Pfefer et al., 2003; Gualtieri and Pursi, 1990; Farrell et al., 1992a). These methods relate observable quantities, such as the amount of transmitted and reflected light, to parameters characterising the sample tissue such as the quantities of chromophores and scattering particles present. These techniques can be categorised into two classes: direct and indirect (Cheong et al., 1990; Tuchin, 2000).

Direct techniques are based on simple concepts such as the Beer-Lambert law and single scattering phase functions (Tuchin, 2000). They use simple analytic expression to relate the reflectance and transmittance spectra to optical parameters that do not depend on any specific model, namely: the *total attenuation* coefficient and the *effective attenuation*

coefficient (Cheong et al., 1990). As a result, the optical coefficients are obtained directly from the fraction of light absorbed or scattered by the sample. The Beer-Lambert, for example, relates the transmittance of light through a medium to the product of its attenuation coefficient and the distance travelled by light using a logarithmic dependence. The parameters characterising the tissue (thickness and attenuation coefficient) can therefore be directly calculated from the observed quantity (transmittance).

However, direct methods cannot be used for most biological tissues and fluids such as skin, brain and blood as they do not strictly fulfil the actual experimental conditions, or the actual structure of the medium (Cheong et al., 1990; Welch and Van Gemert, 1992; Duck, 1990; Kay, 1993; Tuchin, 2000). Consequently, direct techniques will not be considered for this research.

Indirect techniques make use of a combination of measured quantities and a theoretical model of light propagation that is more advanced than the concepts used in direct techniques. The model describes the physical properties of the biological tissue, such as the number of different layers, their thicknesses and refractive indices (Tuchin, 2000; Welch and Van Gemert, 1992; Prahl et al., 1993b). It also reflects knowledge about the various chromophores and scatterers present in the tissue. Such methods are very popular when the analysed tissue is thick enough for multiple scattering events to occur and physical measurements are obtainable. They can be further subdivided into two categories, namely iterative and non-iterative (Tuchin, 2000; Cheong et al., 1990).

Non-iterative indirect techniques, such as the Kubelka-Munk method (Cotton, 1998), are based on equations where the reflectance and transmittance spectra are described directly in terms of the evaluated parameters. Dissimilarly, iterative techniques use more complicated solutions to the transport equations such as Monte-Carlo (Wang and Jacques) and adding-doubling methods (Prahl et al., 1993a) where it is necessary to go through multiple iterations to approximate measurable quantities (such as transmittance and reflectance) from optical properties of the tissue (such as absorption and scattering coefficients).

Although non-iterative methods are often simpler and faster than their iterative counterparts, they are believed to be rigid. For example, The Kubelka-Munk method does not consider boundary reflectance even though it is always present as the refractive indices of the sample and its surrounding medium are often different. On the other hand, iterative methods are approximative and often slow due to their iterative nature, but more information about the tissue can be incorporated into the optical model employed. They can therefore provide more realistic results than the non-iterative techniques (Cheong et al., 1990).

1.1 Motivation

Although most of the aforementioned techniques are widely used and may provide accurate results, they suffer from a number of limitations. For instance, while direct methods can provide good results under certain conditions, they impose very strict constraints on the studied sample. For instance, the Beer-Lambert method can only be used if the attenuating medium is non-scattering which is untrue for biological tissues. Such constraints are therefore not always possible to respect and can lead to incorrect solutions.

Similarly, a drawback of indirect techniques is that they sometimes require approximations that are often invalid for biological tissues. For example, indirect models often assume approximative values for some tissue properties such as ranges for layer thicknesses. During this process, assumptions are made about the characteristics of the investigated tissue due to unknown inter-subject variations. These assumptions can lead to inaccurate or even incorrect results. Nevertheless, indirect methods are often preferred to their analytical counterparts because the constraints they impose are not as stringent as those required in direct approaches.

While both iterative and non-iterative indirect techniques were proven to be successful when studying a number of biological tissues (e.g. skin), we note that their outcomes are in need for improvements under certain conditions. In fact, the results of these techniques can lack accuracy when the available information about the structure of the biological

medium is not sufficient. For instance, while some tissues such as the human skin have been extensively studied, both *in vivo* and *ex vivo*, making their physical properties well understood and documented, other tissues are not so well characterised. For such media, creating a forward model is only possible through approximations of the tissue's properties (e.g. layers thicknesses) making uncertainty an inherent part of the model that the inversion algorithm has to successfully tolerate.

In addition, a number of methods used today are intended to recover the absorption and scattering coefficients of the biological medium. Though these parameters are useful, knowing the blood oxygenation levels or water content of a tissue, for example, might be more helpful from a diagnostician's perspective. Though numerous other methods provide estimates for these parameters, many do so using a second inversion process rather than a direct result of estimation using the measured reflectance or transmittance spectra. For instance, such methods may recover chromophore and scatterer concentrations from absorption and scattering coefficients, that were estimated from reflectance spectra, which induces further possible errors in the result.

Another issue that arises when solving inverse problems is whether or not an appropriate solution does exist. In fact, there may be no model that exactly fits the data due to the presence of noise. In addition, there is also the risk of fitting to the noise when only limited measurements are available. Even when solutions do exist, the mapping between the model and the data may not be one-to-one, resulting in more than one model producing the same reflectance data (Hidovic-Rowe, 2006). Consequently, it may be impossible to determine which solution to choose using classical parameter recovery methods. Finally, the process of recovering parameters can very often be unstable as small changes to measurements can lead to large changes in the estimated model. It is worth noting that this process can be stabilised by imposing additional constraints that bias the solution (i.e. regularisation).

To attend to these issues, we propose a Bayesian-based inversion method that estimates concentrations of the main chromophores present in a biological tissue despite uncertainty in its other underlying physical attributes. The method is tested using data from simulated

reflectance spectra, measurements obtained from gelatin phantoms, and hyper-spectral images of the human colon. The optical properties of interest are recovered directly from reflectance or transmittance measurements.

Throughout this thesis, we will use the term "light" to refer to diffuse white light in the visible to near-infra-red light ($400-700\,nm$). We will also use the term "optical properties" to refer to the concentrations of chromophores such as melanin and haemoglobin, as well as the concentration of scattering particles. More information about these properties is available in later chapters.

1.2 Problem Specification

This research has two main goals:

1. To retrieve the optical properties of a biological tissue from reflectance measurements. These properties include the concentrations of the chromophores present, blood oxygenation and reduced scattering coefficient*.

2. To succeed in retrieving the aforementioned values when the physical attributes of the said tissue are uncertain. That is, our method is aimed at coping with the uncertainty present in the tissue's specification and should behave well even when the physical characteristics of the biological tissue are not known exactly (e.g. layers thicknesses, optical coefficients of chromophores...etc.).

The absorption and scattering coefficient of a tissue can, in theory, be successfully retrieved when the physical properties are well defined. However, they may not perform as well when such properties are missing or imprecise. This is because such methods rely on the correctness and accuracy of the forward model used during the inversion process. They also rely on the accuracy of the parameters used in said model. In addition, these methods also fail when the mapping between the optical parameters of the tissue and the

*Formal definitions of these properties are available in Chapter 2

measured spectra is not one-to-one as described in Section 1.1. Finally, the existing inversion methods, that do not retrieve the previously mentioned optical parameters directly, are affected by the additional errors introduced in their calculations.

1.3 Proposed Solution

In order to address the problem, we propose to develop an inversion method based on the *Maximum A Posteriori* estimation technique. This method will be used to recover a number of parameters describing a biological tissue even if some of the physical properties of this tissue are not definite. We will work in two stages:

1. Feasibility study: the aim of this phase is to investigate the possibility of applying the theory of estimation to a simple, well defined version of our problem. We start by clearly specifying the problem in a form that can be solved by Bayesian estimation techniques. We then model a simple tissue where the physical and optical properties are predetermined. Next, we apply estimation to retrieve its unknown optical parameters. We choose the human skin to test our inversion method as an example of a tissue whose properties are well defined but not precisely known.

2. Application to biological tissue: during this stage, we apply our inversion method to measured spectra to account for the presence of noise and uncertainty. We use two sets of measurements: transmittance spectra collected from gelatin phantoms, and reflectance spectra recovered from multispectral images of the human colon.

1.4 Thesis Structure

This section describes the structure of this thesis and provides a brief description of each section.

I. Fundamentals of Tissue Optics: Introduces widely used concepts of tissue optics such as known solutions to the transport theory as well as a number of terms that are used throughout the thesis. We describe the Kubelka-Munk method, a technique

that provides a simple analytical solution to the radiation transport equation, and which relates the transmission (T) and reflectance (R) of light at a specific wavelength to the tissue's absorption and scattering. We also review the adding-doubling technique which quickly generates accurate estimates of light distributions in a biological medium. Finally, we introduce the Monte Carlo method and outline its advantages and limitation.

II. Model-Based Parameter Recovery: Puts the proposed solution in context. We first introduce the different methods traditionally used to recover tissue optical properties and review their performance. We then introduce classical and Bayesian estimation techniques and elaborate on how our proposed solution may address some of the issues related with the use of traditional parameter recovery methods. This chapter is hence divided into two sections. The first one reviews the existing literature about tissue parameter recovery. The second introduces estimation theory, mainly focusing on three techniques: Least squares, maximum likelihood and maximum *a posteriori*.

III. Application of the MAP based Estimation Method to Simulated Data: Human Skin In this chapter, we give a detailed description of the structure of the human skin. We describe how light reflectance is modelled in the skin and the various parameters required to construct such a model. We then apply our inversion method to reflectance spectra simulated using the aforementioned model. Finally, we analyse the results in comparison with classical estimation techniques, namely: least squares and maximum likelihood.

IV. Application to Gelatin Phantoms: We describe our first attempt at applying our inversion method to measured rather than simulated Data. We outline how we constructed a number of scattering and non-scattering phantoms using simple and commercially available materials. We then construct forward models of light transfer within these phantoms. Later, we collect transmittance spectra from these samples and recover the concentrations of absorbing and scattering particles using our inversion method.

V. Application to multispectral Images of the Human Colon: This section describes how our inversion method was applied to multispectral images of the colon. We first describe the tissue composition of the colon, and the parameters required for building a forward model of light reflectance. We then outline some of the changes that accompany the formation of colorectal adenocarcinomas in the human colon. These changes are used to support our claim that we may be able to differentiate between normal and abnormal tissue based on the recovered optical properties.

   We describe the imaging setup used to acquire the multispectral images of the colon, and how it has been modelled to allow us to recover reflectance spectra from image values. Note that this section builds on the findings described in (Hidovic-Rowe, 2006) who have developed the colon model as well as acquired the multispectral images that we use to test our inversion algorithm.

VI. Conclusions and Future Work: Summarises the results of the experiments and evaluates the performance of our estimator against traditional techniques. It also appraises the work completed so far by discussing its importance, its strengths and limitations. Finally, we suggest some avenues to improve and extend the current results.

Chapter 2

Fundamentals of Tissue Optics

2.1 Introduction

Biological tissues and fluids such as skin, brain and blood are inhomogeneous and considered to be strongly scattering in the visible to near-infra-red range. As light travels through these media, it can either be absorbed, transmitted, scattered or reflected. These phenomena are responsible for light beams decaying, broadening or being reflected back. The absorbed light is converted to heat while the reflected and transmitted light can be measured and analysed to reveal information about the internal structure of the tissue.

This interaction is described by the Radiation Transport Equation (2.1) (RTE), where $\phi(\mathbf{r},\mathbf{s})[W\,cm^{-2}sr^{-1}]$ is the radiance at point $\mathbf{r}$ in direction $\mathbf{s}$ ($|\mathbf{s}| = 1$), $\mu_a[cm^{-1}]$ and $\mu_s[cm^{-1}]$ are the absorption and scattering coefficients for the medium respectively; $P(\mathbf{s},\mathbf{s}')$ $[sr^{-1}]$ the scattering phase function and $Q(\mathbf{r},\mathbf{s})$ represents all sources of radiance within the boundary of the problem (Tuchin, 2000).

$$\mathbf{s}\cdot\nabla\phi(\mathbf{r},\mathbf{s}) = -(\mu_a+\mu_s)\phi(\mathbf{r},\mathbf{s}) + \mu_s(\mathbf{r})\int P(\mathbf{s},\mathbf{s}')\phi(\mathbf{r},\mathbf{s}')\mathrm{d}\mathbf{s}' + Q(\mathbf{r},\mathbf{s}); \tag{2.1}$$

Consequently, it can be claimed that the transport equation is governed by the absorption and scattering coefficient μ_a and μ_s'. A model of light propagation through a biological medium should be founded on the possible solutions of the RTE and constructed around these parameters. This section will give a brief introduction to the aforementioned quantities. Note that throughout this chapter, we will only consider light in the visible to near-infra-red range ($400 - 700\,nm$).

2.2 Absorption

The absorption of light into a biological tissue transforms the photons energy into heat. This process is normally quantified by the *absorption coefficient* μ_a which describes the extent to which energy is absorbed by the medium. The absorption coefficient depends on the wavelength and type of the tissue under study and can therefore provide valuable information about the chemical composition of a tissue. It can ultimately support in the diagnosis process, making photon absorption an important event in biomedical optics.

The absorption coefficient can be described by equation (2.2) wherein $\varepsilon_i(\lambda)$ is the molar extinction coefficient of the i^{th} absorber given as a function of wavelength λ and C_i its concentration.

$$\mu_a(\lambda) = \sum_i \varepsilon_i(\lambda)\mathrm{C}_i \tag{2.2}$$

Haemoglobin and water are the most commonly found absorbers in biological tissues. Haemoglobin can be found in two forms: oxygenated and de-oxygenated. As depicted by Figure 4.2, which represents the molar extinction coefficient (ε) of oxy- and deoxy-haemoglobin, they both absorb strongly in the blue and green regions of the spectrum. We can therefore approximate the absorption coefficient of blood as $\varepsilon_{\mathrm{Hb}}(\lambda)\mathrm{C}_{\mathrm{Hb}} + \varepsilon_{\mathrm{Hb0}}(\lambda)\mathrm{C}_{\mathrm{Hb0}}$.

With the the concentration of haemoglobin per unit volume of blood being reported as 150/64500 in Prahl (2007a) and S being the oxygen saturation, the concentrations of haemoglobin and oxy-haemoglobin can be calculated as $S * 150/64500$ and $(1 - S) * 150/64500$ respectively. Equation (2.3) is commonly used to calculate the absorption coefficient of blood where $ln(10)$ is a correction factor (Prahl, 2007a).

$$\mu_a^{Blood}(\lambda) = ln(10) * 150/64500 * [S\varepsilon_{\mathrm{HbO_2}}(\lambda) + (1 - S)\varepsilon_{\mathrm{Hb}}(\lambda)] \tag{2.3}$$

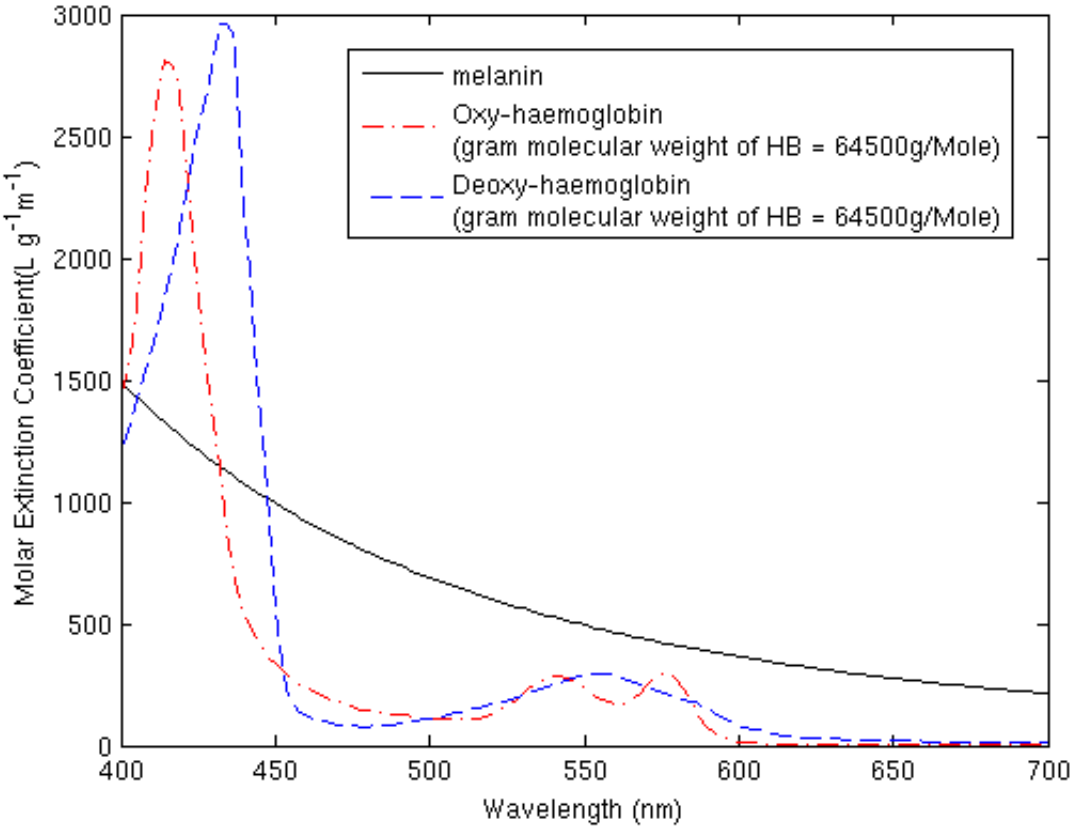

Figure 2.1: Molar extinction coefficient spectra for melanin, oxy- and deoxy-haemoglobin (Data from Prahl (2007a))

2.3 Scattering

Photon scattering occurs in media which contain particles of different refractive indices. When a photon collides with a particle whose refractive index is different from its surroundings, the photon is diverted from its original path. This contributes to the diffusion of light in the tissue. The factor that expresses the amount of light scattered per unit of distance is called the *scattering coefficient* μ_s.

Scattering can be categorised into two types according to the size of the scattering particles present in the tissue. *Rayleigh* scattering occurs when the particles in question are small in comparison to light wavelengths while *Mie* scattering is appropriate for larger particles. In a tissue where both types are present, the scattering coefficient can be calculated by equation (2.4).

$$\mu_s(\lambda) = \mu_s^{Rayleigh}(\lambda) + \mu_s^{Mie}(\lambda) \tag{2.4}$$

Scattering also has diagnostic value as it depends on the structure of a tissue and, as a result, the amount of reflected light (also affected by scattering) can be used to detect abnormalities in the tissue under study.

One quantity that is associated with scattering is the *scattering phase function*. The scattering phase function $P(\mathbf{s}, \mathbf{s}') = P(\theta)[sr^{-1}]$ describes the probability of a photon scattering at an angle θ relative to its original trajectory, where $\mathbf{s}, \mathbf{s}'$ are unit vectors in the directions of incident and scattered light respectively, and θ is the angle between them (Jacques, 1998). One of the most frequently used scattering phase functions is the Henyey-Greenstein function defined in equation (2.5). It was devised to mimic the angular dependence of light scattering by small particles to describe light scattering by interstellar dust clouds (Jacques, 1998; Henyey and Greenstein, 1941). The Henyey-Greenstein function was shown to reasonably agree with measured angular distribution in biomedical media as described in (Jacques et al., 1987).

$$p(\theta) = \frac{1 - g^2}{4\pi(1 + g^2 - 2gcos(\theta))^{\frac{3}{2})}} \quad \text{where} \quad \int_0^\pi P(\theta) 2\pi sin(\theta) \mathrm{d}\theta = 1 \tag{2.5}$$

Another quantity that is often used in conjunction with the scattering coefficient is g, the *anisotropy factor*. This parameter is often used to describe the average direction of scattering events: a value of 0 means the scattering is equally distributed in all directions (isotropic), a value closer to 1 implies strong forward scattering and a negative value implies backward scattering. The anisotropy factor is given as the average cosine of the scattering angle where $g = \int_0^\pi P(\theta) cos(\theta) 2\pi sin(\theta) \mathrm{d}\theta$ and $P(\theta)$ is the scattering phase function.

The scattering coefficient and the anysotropy factor can be combined to define another quantity, namely: the *reduced scattering coefficient* $\mu_s' = (1 - g)\mu_s$. Another approach

often used to describe the reduced scattering coefficient directly is that of Mourant et al. (1997) where μ_s' is a scaled power of wavelength λ as described in Equation (2.6) where α is the scaling factor and β depends on the size of the scattering agents.

$$\mu_s' = \alpha\lambda^{-\beta} \tag{2.6}$$

The equation is often used as an approximation to the reduced scattering coefficient as it has been shown that when the ratio of indices of refraction m (scattering particle to surrounding medium) is $1 < m < 1.1$ and the size x of the scattering particle is $5 < x < 50$, $\mu_s' \propto \lambda^{-0.37}$ in the range $350 - 950\,nm$ (Mourant et al., 1997). For values of the size parameter x that decrease below 5, the wavelength dependence of $\mu_s'(\lambda)$ approaches λ^{-4} which is the expected dependence for Rayleigh scattering (2.6). In the following section, we describe a number of methods that are often used to approximate solutions to the radiative transport equation.

2.4 Transport Theory

Although equation (2.1) can be easily comprehended in physical terms, solving it analytically is more challenging and can only be achieved for homogeneous media in regular geometries (Tuchin, 2000). As a result, there have been many attempts at providing approximate solutions such as the Kubelka-Munk theory and the diffusion approximation (Farrell et al., 1992b; Kienle et al., 1998). These methods however are limited because they can only be used in specific circumstances.

The following section provides a brief introduction to the diffusion approximation, and the Kubelka-Munk theory as possible solutions to the RTE. In Section 2.4.3, we describe a numerical solution based on the Monte-Carlo method which provides more accurate results and can be used for a wider range of media. We then give a brief introduction to some methods that are often used to model light transport in biological tissues, namely: the adding-doubling technique and the finite elements method.

2.4.1 The Diffusion Approximation

The radiative transport equation can be solved by making a number of assumptions about the behaviour of photons in the medium, therefore reducing the number of independent variables (Wang and Wu, 2007). These assumptions lead to the application of the diffusion theory to the RTE, and they are:

- Directional Broadening: The number of scattering events is much larger than that of absorption events. Similarly, a few absorption events will occur after a larger number of scattering events and the radiance becomes nearly isotropic.

- Temporal Broadening: The time for the current density to substantially change is significantly longer than the time needed to traverse one transport mean free path.

Note that both assumptions require the tissue to be predominantly scattering, and consequently, the reduced scattering coefficient is significantly larger than its absorption coefficient (Wang and Wu, 2007; Yoo et al., 1990). They also assume that the tissue thickness is of the order of at least a few transport mean free path (Yoo et al., 1990). Consequently, the diffusion approximation cannot be used for highly absorbing tissues such as the skin and the colon and is therefore unusable for our purposes.

2.4.2 The Kubelka-Munk Model

Many models rely on simple methods to solve the transport equation such as the two-flux Kubelka-Munk theory (Cotton, 1998). Within this method, light travelling through a tissue is divided into opposing diffuse fluxes: I, flux in the same direction as the incoming radiance, and J, the flux in the opposite direction. At a distance x from the surface, the change in flux over a distance $\mathrm{d}x$ for the two fluxes is:

$$\mathrm{d}I = -(\mu_a + \mu_s')I\mathrm{d}x + \mu_s' J\mathrm{d}x \quad \text{and} \tag{2.7}$$

$$\mathrm{d}J = (\mu_a + \mu_s')J\mathrm{d}x - \mu_s' I\mathrm{d}x \tag{2.8}$$

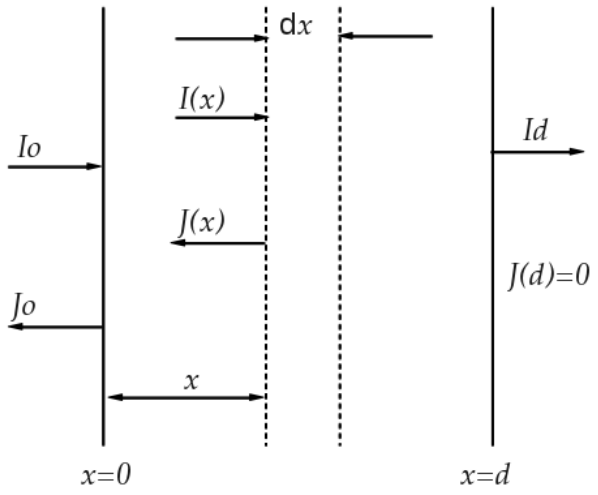

Figure 2.2: The Kubelka-Munk two flux model

Equations (2.7) and (2.8) have an exponential solution and by applying the boundary conditions $I(0) = I$ and $J(d) = 0$ shown in Figure 2.2, we can relate the transmittance T and reflectance R to the absorption μ_a and the reduced scattering μ'_s coefficients as shown in equations (2.9) and (2.10) where d is the tissue thickness (Nobbs, 1985; Egan and Hilgeman, 1979).

$$R = \frac{I_0}{J_0} = \frac{A(e^{Bd} - e^{-Bd})}{A^2 e^{Bd} - e^{-Bd}} \tag{2.9}$$

$$T = \frac{I_d}{I_0} = \frac{A^2 - 1}{A^2 e^{Bd} - e^{-Bd}} \quad \text{with} \tag{2.10}$$

$$A = \frac{\mu_a + \mu'_s + B}{\mu'_s} \quad \text{and} \quad B = \sqrt{\mu_a(\mu_a + 2\mu'_s)}$$

The Kubelka-Munk theory provides a simple analytical solution to the radiation transport equation which can be fruitful for understanding the basic principles of light propagation (Nobbs, 1985). This theory, however, makes two main assumptions: that the tissue contains particles small in comparison with the tissue's thickness so that multiple scattering events can occur, and that the illumination on the tissue is diffuse. This makes the theory suitable for tissues where the assumptions hold but unsuitable for others. To

counter these limitations, some revisions to the Kubelka-Munk theory were suggested.

In fact, the suitability of the Kubelka-Munk theory for modelling light propagation in biological tissues has been disputed by some authors such as Cheong et al. (1990) who states that in addition to the limitations imposed by the assumptions above, the general model only considers forward and backward flux of light which differs from what happens in practice. However, the Kubelka-Munk theory is particularly applicable to the human skin as reported in (Anderson et al., 1981b; Van Gemert et al., 1989; Cotton, 1998) who recommend it as a particularly good model in the visible range as its results proved to be very similar to those obtained by more elaborate models (Van Gemert et al., 1989; Reuter et al., 2013).

2.4.3 Monte Carlo Simulation for Multi-Layered Media

While the Kubelka-Munk theory provides an approximate solution to the radiative transfer equation (RTE), it is apparent that finding a solution with more accurate estimates is crucial for practical use. As solving the RTE analytically is highly difficult, and given the need for handling arbitrary boundary conditions, numerical methods such as finite elements model and Monte-Carlo became necessary alternatives (Tuchin, 2000).

The Monte Carlo method is widely used to solve the RTE in different scientific fields (Tuchin, 2000). In biomedical simulations, light is considered to be composed of photons, and the goal is to trace each of these photons while they propagate through the tissue. The simulation relies on the use of an accurate representation of the tissue characteristics such as the number of layers as well as the thickness d, refractive index n, absorption and scattering coefficients μ_a and μ_s; and anisotropy factor g for each layer. The propagation of photons is governed by a number of rules such as the step size of their movements and scattering angles which are generated stochastically (Wang and Jacques; Wang et al., 1995).

One software which uses this method to simulate light transport in multi-layered media is MCML (Wang and Jacques; Wang et al., 1995). The software is based on the random

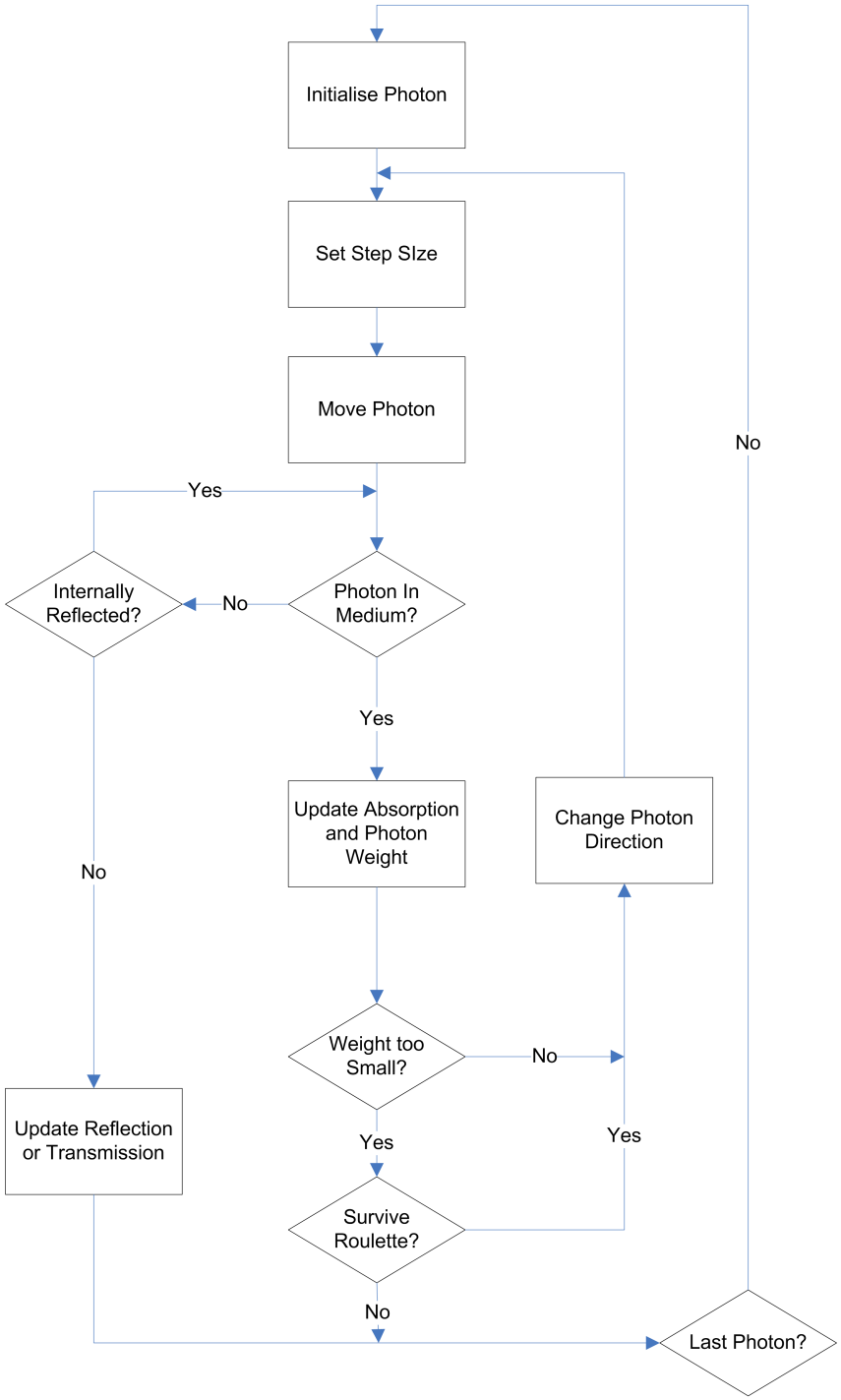

Figure 2.3: Flowchart of MCML
(Prahl et al., 1989)

walks that photons make as they travel through the medium. As described in (Prahl et al., 1989), the software starts by launching a photon into the tissue. When simulating diffuse irradiance, the direction of the photon is chosen randomly from all possible directions downwards. The photon is then moved. If it has left the tissue, then the possibility

of internal reflection is checked as follows: If the photon is not reflected internally, it is recorded as having escaped. Otherwise, the photon position is updated accordingly. In the latter case, a fraction of the photon is absorbed at each step which leads to this absorption event being recorded, and to the photon weight being adjusted accordingly. If the weight of the photon is deemed too small, the photon is either propagated or extinguished, in which case, a new photon is started. Otherwise, the photon is scattered. The process is repeated until the photon has either exited the tissue, or was extinguished at which case, a new photon is started (Prahl et al., 1989).

Photons histories are recorded as they are scattered or absorbed. The program takes the aforementioned optical properties of each layer of the tissue as an input and provides a probabilistic result representing the reflectance (Wang and Jacques; Tuchin, 2000; Prahl et al., 1989). Figure 2.3 provides a summary of the logic behind the MCML software as reported in (Prahl et al., 1989; Wang and Jacques).

MCML also considers the refractive index and thickness of each layer in order to calculate the reflectance (Wang and Jacques). Consequently, the software (and the method in general) can be used for any type of tissue as long as its optical parameters are known. Note that the accuracy of the results generally increases with the use of a large enough number of photons which could be millions or more depending on the tissue characteristics and required precision. Consequently, this method is computationally expensive as it simulates the propagation of a large number of photons. Another Monte-Carlo based method that may be used to overcome the long computational time is Monte Carlo Extreme (MCX), a method that uses GPU-based parallel computing to simulate fast photon transport (Fang and Boas, 2013).

2.4.4 Adding-Doubling Method

As suggested by its name, this technique involves two main steps. The first step consists of calculating the reflection and transmission for a thin homogeneous starting layer with the same optical properties as the tissue to be studied. Then, the reflection and transmission

of a layer twice as thick is calculated by superposing two identical layers and summing the contributions from each one of them (Prahl et al., 1993a; Prahl, 1993; de Hulst, 1980). For an arbitrarily large layer, this operation is repeated until the desired thickness is reached.

The adding method extends the doubling method to cater for layers with different optical properties, thereby allowing the simulation of light propagation of a multi-layered medium and/or one with internal reflection at boundaries. This is achieved by placing slabs with different optical properties adjacent to one another and adding their contribution to the value of reflectance (Prahl et al., 1993b).

The main disadvantage of this method is that it is restricted to layered media with uniform irradiation, and homogeneous layers. Although it is a limitation from a theoretical standpoint, it does not pose a problem in practise as most biological tissues can be considered to conform to those conditions (Prahl et al., 1993b). On the other hand, the adding-doubling method has a clear advantage over other methods such as the Kubelka-Munk technique in that it can easily handle boundary conditions. In fact, these can be implemented simply by adding a layer which mimics the reflection and transmission at a boundary.

Additionally, it is believed to be well-suited to iterative problems as it provides accurate total reflection and transmission calculations with relatively few integration points (Prahl et al., 1993b). Further information about the adding-doubling method and its origins is available in (Prahl et al., 1991, 1993a; Prahl, 1993, 1995b; Van de Hulst, 1962; Van de Hulst and Grossman, 1968; de Hulst, 1980; Wiscombe, 1976, 1977b,a).

2.4.5 Finite Elements Method

In addition to the methods listed above, there exists various other techniques that can be used to approximate a solution to the radiative transport equation such as the finite element method (FEM). The finite element method is widely used to solve partial differential equations in complex geometries and has been increasingly used in diffuse optical tomography ever since it was introduced by Arridge et al. (1993). The basic

idea behind FEM is to reduce a complex, continuous and heterogeneous problem such as modelling light transfer in a complex medium to a finite-dimensional system (Schweiger et al., 1995).

To that aim, the volume describing the tissue of interest is divided into a large number of small elements of known shape, and the potential is calculated for each element by linearising the problem within each element (Bagshaw et al., 2003). This allows us to accurately define regions with heterogeneous optical properties with the accuracy depending on the fineness of the mesh (Elisee, 2011). Consequently, a more realistic geometry can be included in the forward model and when FEM is combined with an appropriate inversion technique, the distribution of the optical parameters throughout the whole volume can be reconstructed. As a result, FEM has become a standard method for modelling complex geometries and inhomogeneous backgrounds such as the breast, brain and small animal imaging (Dehghani et al., 2003; Chaudhari et al., 2005; Srinivasan et al., 2005).

Finite element method has also been combined with other techniques in hybrid solution schemes. For instance, Tarvainen et al. (2006) developed a finite element model for the coupled radiative transfer equation and diffusion approximation. In their approach, the radiative transport equation was used as a forward model in sub-domains in which the assumptions of the diffusion approximation (DA) are not valid while the diffusion approximation was used elsewhere in the domain. The radiative transport equation and diffusion approximation were coupled through approximate boundary conditions between the RTE and DA sub-domains and their equations solved simultaneously using the finite element method. Their results were then compared with finite element solutions of the radiative transfer equation and the diffusion approximation and showed that coupled RTE-DA model gave very similar results to those obtained from using the RTE in the whole domain and better results than those obtained through the diffusion approximation (Tarvainen et al., 2006).

Arridge and Schweiger (1993) developed the TOAST (Time-resolved Optical Absorption and Scattering Tomography) algorithm to reconstruct the absorption and scattering

coefficients of a tissue given the time-dependent photon flux at its surface. The algorithm consists of two parts: a forward solver that uses the finite element method to simulate the propagation of light in a biological tissues, and an inverse solver that uses an iterative method to recover the absorption and scattering coefficients of the tissue from boundary measurements of light transmission (Arridge and Schweiger, 1993). A software suite written in C++ and based on this algorithm, Toast++, was later developed by Schweiger and Arridge (2014) to simulate near-infrared light travel in complex, highly scattering and heterogeneous media (Schweiger and Arridge, 2014).

Another software package, Near Infra-Red Fluorescence and Spectral Tomography (NIRFAST), which uses the finite element method to simulate light propagation in biological tissue was recently developed (Dehghani et al., 2009). It allows users to easily model standard single wavelength absorption and reduced scattering coefficients as well as multi-wavelength spectrally constrained and fluorescence models (Dehghani et al., 2009). As it is written in MATLAB, NIRFAST can also easily supports user extensions.

The main advantage of the finite element method over other numerical techniques is the ability to model very complex structures relatively easily while also including boundary effects. However, a well known limitation of FEM-based models is its failure to recover the optical properties of a tissue when dealing with low-scattering regions (Elisee, 2011; Firbank et al., 1996). Another limitation arises when dealing with thin multi-layered tissues as this requires the generation of a large number of small elements that may have strong discontinuities in optical properties due to the layered structure. This, in turn, leads to an increased computational cost (Elisee, 2011). Due to the thinness and multi-layered nature of the biological tissues of interest to this research, namely, the skin and colon, this method will not be used to model light transfer in either tissue.

2.5 Conclusion

As stated earlier, the parameter recovery process involves two main components: the forward model describing light transfer in the tissue, and the inversion method used to

actually recover the parameters. In this chapter, we described a number of methods that can be used to provide approximate solutions to the radiation transport equation. We introduced the diffusion approximation theory and how it is unsuitable for our purposes due to the fact that the tissues of interest to our research are highly absorbing. This was followed by a description of a simple analytical solution to the RTE, namely: The Kubelka-Munk method. We demonstrated how it is popular for certain biological tissues, such as the skin, but in general, is mainly used to provide crude estimates due to the stringent constraints it imposes on the tissue.

A Monte Carlo based method was then described and possible variations were suggested to overcome the computational cost of this technique. This was followed by a brief description of the inverse adding-doubling technique and the finite element method and how the latter is also unsuitable for our work due to the thinness and multi-layered nature of the biomedical tissues we study. The next chapter introduces a number of optimisation and estimation techniques that can be used in the second step of the parameter recovery process, along with a description of how they are used in biomedical optics.

Chapter 3

Model-Based Parameter Recovery

3.1 Introduction

As previously discussed, when light is reflected from a biological tissue, it holds important information about its internal structure such as anomalies in blood flow or oxygenation. This fact has motivated many attempts to answer some physiological questions using escaped light by quantifying some tissue properties including the concentrations of chromophores and scattering coefficients (Arridge and Hebden, 1997; Arridge, 1999; Gibson et al., 2005).

Though they vary in some aspects, most of these methods are based on a forward model of light travel through the tissue, and their aim is to minimise the difference between the measured spectra and data produced by the model. Simulated data is generated for different values of a parameter vector $\boldsymbol{\theta}$ that describes the biological tissue, and each spectra is compared with the measured data. Consequently, most algorithms aiming to recover the optical properties of a biological tissue rely on a common component: an optimisation algorithm that aims to minimise the difference between the modelled and measured spectra.

The next section provides a brief introduction to optimisation theory followed by descriptions of commonly used optimisation algorithms. We then describe a number of optimisation methods used in biomedical optics. Finally, we introduce three estimation techniques, namely: least-squares (LSQ), maximum likelihood (ML) and maximum *a posteriori* (MAP) methods.

3.2 Introduction to Optimisation Algorithms

An optimisation algorithm aims to find a value of the vector parameter $\boldsymbol{\theta}$ that describes the biological tissue, and minimises the difference between the data generated by the forward model and measured spectra. It is motivated by the fact that the result of the recovery process improves as the generated and measured spectra get closer. Consequently, most existing parameter recovery techniques that use forward models rely on two main ideas:

1. The forward model used to describe light interaction with the tissue is assumed to reflect all available information about the tissue.

2. The required parameters are those that minimise the difference between the measured spectra and the one generated by the forward model.

There exist various optimisation algorithms that can be used as part of the parameter recovery process. In this chapter, we describe a number of such optimisation algorithms and review some application-specific methods before introducing three estimation techniques that may be used to recover the optical properties of a biological tissue.

Prior to that, we provide concise definitions to a number of keywords, often used throughout this thesis. These definitions are adapted from those in (Weise, 2007).

Definition 3.2.1 (Problem Space)**.** The problem space Θ of an optimisation problem is the set of possible solutions $\boldsymbol{\theta}$.

Definition 3.2.2 (Search Space)**.** The search space $\mathbb{G}$ is the set of elements (called genotypes hereafter) searched during the optimisation algorithm.

Definition 3.2.3 (Solution Candidate)**.** A solution candidate is an element of the search space Θ of the optimisation problem.

Definition 3.2.4 (Single Objective Functions)**.** In the case of optimising a single criterion f, an optimum is either its maximum or minimum, depending on what we are looking for.

Definition 3.2.5 (Population)**.** A population $\mathbb{P}$ is the set of individuals p used during the optimisation process.

Definition 3.2.6 (Fitness)**.** The fitness value $v(\boldsymbol{\theta}^*) \in \mathbb{V}$ of an element $\boldsymbol{\theta}^*$ corresponds to its utility or priority in the subsequent steps of the optimisation process.

Definition 3.2.7 (Mutation)**.** Mutation is a process used to create a new element (genotype when used in genetic programming) by modifying an existing one. This process can either be randomised or deterministic depending on the application in which it is being used.

Definition 3.2.8 (Duplication)**.** This operation duplicate creates an exact copy of an existing element and often occurs to strengthen the presence of a given type of elements in a population.

Definition 3.2.9 (Crossover)**.** The crossover operation is used to create a new element by combining the characteristics of two existing ones.

3.3 Common Optimisation Algorithms

In this section, we describe a number of optimisation techniques that could be used as part of the parameter recovery process. We also describe their usage and limitations.

3.3.1 Hill Climbing

Hill climbing is one of the simplest optimisation algorithms to implement. As a result, it is widely used in areas such as artificial intelligence (Russel and Norvig, 2003). The algorithm consists of a loop, in which the currently known best estimate $\boldsymbol{\theta}^*$ is used to produce one offspring $\boldsymbol{\theta}_{new}$ by incrementally changing a single element of $\boldsymbol{\theta}^*$. If this new individual is better than its parent, it replaces it and the cycle restarts. The first solution candidate is usually random as the algorithm uses a parameter-less search operation to produce it (Russel and Norvig, 2003).

However, this algorithm suffers an important limitation: premature convergence. This occurs when the algorithm reaches a flat area of the search space where all nearby solutions are the same. The algorithm then stops running as it believes that it reached the optimal solution when the latter may exist in another area of the search space. Consequently, although the algorithm may always be able to find the local optimum, it may not always reach the global one. Nevertheless, the behaviour of the algorithm may be improved by implementing a few modification such as prohibiting the revisit of recently viewed elements or restarting the search at different parts of the search space. Other variants have been suggested such as the dynamic (Yuret and de la Maza, 1993) and stochastic hill climbing approaches (Russel and Norvig, 2003).

This method is sometimes used for the recovery of optical parameters but rarely those of a biological medium. A modified version of the hill-climbing technique was used to calculate the optical properties of thin metallic films from reflectance and transmittance measurements (Ward et al., 1969). Kutavichus *et al.* also used reflectance and transmittance spectra to calculate the optical parameters and thickness of weakly absorbing thin films. The authors used the hill climbing technique to provide accurate and unique solutions to the inverse problem (Kutavichus et al., 2006).

3.3.2 Gradient Descent

The gradient-descent technique -sometimes called steepest descent- is an optimisation method that aims to find the local minimum of a function f. As described in (Snyman, 2005; Nocedal and Wright, 1999), the algorithm works by starting at an initial guess $\boldsymbol{\theta}_0$ and iteratively taking small steps relative to the negative of the gradient γ at the current estimate $\boldsymbol{\theta}_i$ such that $\boldsymbol{\theta}_{i+1} = \boldsymbol{\theta}_i - \gamma \nabla f(\boldsymbol{\theta}_i)$ where ∇ is the step size. The step size can either be fixed or change at every iteration. The value of ∇ can be chosen by a number of methods such as Cauchy's and Barzilai and Borwein's as described in (Yuan, 2008). Note that the gradient-descent method can also be adapted to find the local maximum by taking the positive gradient of the function instead of the negative one.

In (Arridge and Schweiger, 1998), the authors demonstrated a simple means to calculate the gradient of an objective function directly, which allowed them to apply a gradient-based optimisation method. They used an objective function based on the sum of squared difference of the data to their forward model. They successfully reconstructed the absorption and scattering coefficients of simulated data, but suggested that further work was needed to evaluate their method on complex data such as neonatal head models (Arridge and Schweiger, 1998).

In fact, though effective when the optimisation problem is well defined, the rate of convergence of gradient descent is often below that of many other methods, as it follows a zigzagging path of decreasing step size (Snyman, 2005). Consequently, the method may not converge to a local minimum within an acceptable number of steps. Other methods, such as the conjugate gradient technique, could be used in such instances (Snyman, 2005). In addition, this method can only be used to find a local minimum which means that if the objective function is multimodal, this method may result in an incorrect estimate.

3.3.3 Gauss-Newton

The Gauss-Newton method could be seen as an adaptation of Newton's method for solving non-linear equations which states that (Fletcher, 2001):

$$\boldsymbol{\theta}_{i+1} = \boldsymbol{\theta}_i - \frac{f'(\boldsymbol{\theta}_i)}{f(\boldsymbol{\theta}_i)}$$

where the next estimate $\boldsymbol{\theta}_{i+1}$ is obtained using the current best estimate $\boldsymbol{\theta}_i$ iteratively and $f'(\boldsymbol{\theta}_i)$ is the first derivative of f. Unlike Newton's method, however, the Gauss-Newton algorithm can only be used to solve problems that involve minimising the sum of squares of residuals (Fletcher, 2001; Bjõrck, 1996).

Consequently, the method is often used to solve non-linear least squares problems where the aim is to find parameters that produce the best possible fit between modelled and measured data. As described in (Fletcher, 2001; Bjõrck, 1996; Nocedal and Wright, 1999), each step towards the optimal solution provided by the Gauss-Newton method is defined

as follows:

$$\boldsymbol{\theta}_{i+1} = \boldsymbol{\theta}_i + \Delta \qquad \text{with} \qquad \Delta = \frac{f'(\boldsymbol{\theta}_i)^{\mathrm{T}}\, f(\boldsymbol{\theta}_i)}{f'(\boldsymbol{\theta}_i)^{\mathrm{T}}\, f'(\boldsymbol{\theta}_i)}$$

$$\text{or using matrices} \quad \Delta = (\mathrm{J}_f^{\mathrm{T}}\mathrm{J}_f)^{-1}\mathrm{J}_f^{\mathrm{T}} f(\boldsymbol{\theta}_i)$$

Where $f = (f_1, ..., f_n)$ is the sum of squares of differences between simulated and measured data and J_f is the Jacobian of function f, and each entry of the Jacobian is defined in (3.1). The Gauss-Newton method suffers from a slow rate of convergence and may, sometimes, not converge at all if the initial guess $\boldsymbol{\theta}_0$ is not sufficiently close to the solution or when the matrix $\mathrm{J}_f^{\mathrm{T}}\mathrm{J}_f$ is ill-conditioned (Fletcher, 2001; Nocedal and Wright, 1999).

$$(\mathrm{J}_f)_{jk} = \frac{\partial f_j(\boldsymbol{\theta})}{\partial \theta_k} \tag{3.1}$$

3.3.4 Levenberg-Marquardt

The Levenberg-Marquardt algorithm aims to minimise a non-linear function over a parameter's space. It is used to minimise the least-square error (See Section 3.6.2) and is widely adopted in a broad spectrum of disciplines that require an efficient solution to general curve fitting problems (Levenberg, 1944; Marquardt, 1963). Levenberg-Marquardt combines the steepest descent and the Gauss-Newton methods as described in (Gavin, 2013). Although it might be slower than Gauss-Newton method when the objective function is well behaved, it is more robust because it will reach a local solution regardless of how far off it starts (Levenberg, 1944; Marquardt, 1963; Gill and Murray, 1978).

To achieve its goal, this algorithm iteratively attempts to minimise the sum of squared differences between the measured ($\mathbf{x}$) and modelled ($\mathrm{R}(\boldsymbol{\theta})$) spectra described as $\sum_{i=1}^{n}(\mathbf{x}_i - \mathrm{R}_i(\boldsymbol{\theta}))^2$. It begins with an initial value for the unknown parameter $\boldsymbol{\theta}$ which can either be based on an informed or uninformed guess. In each iteration, the value of $\boldsymbol{\theta}^*$ is replaced by an estimate $(\boldsymbol{\theta}^* + \delta)$ until the minimum of the sum of squares is reached. This is achieved if the reduction of sum of squares from the latest value of $(\boldsymbol{\theta}^* + \delta)$ falls below a predefined limit, causing the iterations to stop and the value of $\hat{\boldsymbol{\theta}} = \boldsymbol{\theta}^* + \delta$ to be returned as the

solution (Levenberg, 1944; Marquardt, 1963; Gill and Murray, 1978).

The Levenberg-Marquardt method is often used to recover the properties of biological tissues. For instance, Zonios *et al.* (Zonios et al., 2001) analysed diffuse reflectance spectra from skin in order to recover the concentration of haemoglobin and melanin, as well as the scattering coefficient of the skin. To that aim, they used the Levenberg-Marquardt method to minimise the squared difference between their model and experimental data for the entire wavelength range of $460-820$ nm. Their results seem promising as the haemoglobin content and scattering coefficient showed only small variations between different tissue types from white Caucasian to black African while the melanin content showed the greatest correlation with the tissue type (Zonios et al., 2001).

3.3.5 Evolutionary Algorithms

An important class of probabilistic metaheuristics is evolutionary algorithms. Despite being numerous, they are all considered to be either variations or extensions to Algorithm 3.1 which uses nature-inspired mechanisms such as duplication (Definition 3.2.8), crossover (Definition 3.2.9) and mutation (Definition 3.2.7) in order to iteratively refine a set of solution candidates (Weise, 2007).

Algorithm 3.1 Example Evolutionary Algorithm

1: **Data**: $\mathbb{P}$: the population, i: a counter, $Mate$: the mating pool, v: the fitness function
2: **Output**: Θ^*: The set of the best elements found
3: **begin**
4: $i := 0$
5: $\mathbb{P} := populate()$
6: **while** (!`terminate`()) **do**
7: $\quad Mate := select(\mathbb{P}, v)$
8: $\quad i := i + 1$
9: $\quad \mathbb{P} := reproduce(Mate)$
10: **end while**
11: **return** $getOptSolutions(\mathbb{P})$
12: **end**

The process starts with the creation of an initial (non-empty) population $\mathbb{P}$ of parameter vectors using the *populate*() function. Until the function *terminate* returns `true`, the

algorithm should repeatedly assign a fitness value to all candidate solutions and choose the candidates to put in the mating pool $Mate$ from $\mathbb{P}$ accordingly. The $reproduce(Mate)$ function generates a new population from the elements in the mating pool by means of duplication, crossover and mutation. Then, it replaces the population with the newly selected one.

After the termination criterion is reached, the optimal individuals p^* are extracted from $\mathbb{P}$, and the set of their corresponding solutions $\boldsymbol{\theta}^*$ is returned. Common termination criteria include finding the required solution; reaching a maximum number of iterations or allocated resources budget; or reaching a flat search area where a better solution could not be produced.

Genetic Algorithms

Genetic algorithms (Weise, 2007; Keller and Banzhaf, 1996; Stadler) form a branch of evolutionary algorithms where the elements of the search space are represented as arrays of elementary types (e.g. as binary strings). They are often used to solve optimisation and search problems in various areas such as bio-informatics (Gondro and Kinghorn, 2007), computer automated designs (Li et al., 2004) as well as finance and economics (Kearney et al., 2000).

Genetic algorithms use a number of techniques inspired by natural evolution, such as inheritance, mutation (Definition 3.2.7), duplication (Definition 3.2.8) and crossover (Definition 3.2.9). Like most iterative methods, genetic algorithms can become prohibitively expensive when the search space becomes too large (due to multiple mutations) or when the number of repeated fitness function evaluations grows too big. It is also often the case that genetic algorithms tend to converge towards a local optimum rather than a global one (Weise, 2007; Keller and Banzhaf, 1996; Stadler).

Cruzado *et al.* presented an iterative method that compared measure reflectance and transmittance spectra with data generated using MCML (Cruzado et al., 2013). This was aimed at recovering the optical properties of turbid media with slab geometry. The

authors used a genetic algorithm as a basis for their search procedure. They compared their results with those obtained using the Inverse Adding Doubling algorithm and found that, in general, both methods retrieve similar values. However, they also noted that one of the main disadvantages of this method was the computation time which is greatly affected by the properties of the sample and the number of photons used in MCML (Cruzado et al., 2013).

3.3.6 Neural networks

An artificial neural network is a computational paradigm inspired by biological nervous systems that can be used to solve computational problems such as optimisation (Aleksander and Morton, 1995). It consists of large number of "neurones" that are highly interconnected and that process information in parallel to solve problems. Unlike other methods, neural networks do not require a pre-set list of steps they need to follow in order to arrive at the required solution. Rather, they are trained on a predetermined set of examples and thus, adapt and learn how to solve similar problems (Aleksander and Morton, 1995).

Consequently, neural networks suffer from two main drawbacks. The first is the choice of training set. In fact, neural networks require a reasonably large training set that is carefully chosen to represent the problems to be solved, otherwise the network may not learn how to find the right solution. Secondly, as it does not follow a pre-determined set of instructions, the result can be unpredictable. Consequently, even if a solution is found, it may not be possible to prove that it is correct or to even understand it.

Neural networks can also be used as an optical parameter recovery technique. After an original attempt by Farrel *et al* (Farrell et al., 1992a), Kienle *et al* investigated the use of neural networks to recover the optical parameters from tissue phantoms as well as bovine (muscle, adipose and liver) and chicken (muscle) tissue (Kienle et al., 1996). During the course of their research, they also compared the results of using an approximative diffusion model to generate analytical expressions for the reflectance, against a more statistical ap-

proach, namely Monte-Carlo. Their results showed that although the analytical approach could reduce the processing time, relatively large errors were incurred in the process.

Consequently, it was established that a more statistical, albeit computationally expensive, method was more appropriate. Thus, the neural network was trained on the results of Monte-Carlo simulations with estimates containing larger errors in μ_a than μ_s' (13.6% vs. 2.6% in tissue phantoms). Their results also showed that using neural networks considerably reduced the computational time of retrieving optical parameters (Kienle et al., 1996). Neural networks were also used in (Jagajothi and Raghavan, 2009) in combination with laser reflectometry to recover the optical parameters and successfully detect abnormalities in human skin (Jagajothi and Raghavan, 2009).

3.4 Optimisation Methods in Biomedical Optics

Optical properties are typically obtained using solutions of the radiative transport equation that express such properties in terms of measurable quantities such as reflectance and transmittance. In this section, we describe a number of techniques targeted specifically at the area of biomedical optics and the recovery of optical parameters from spectra.

3.4.1 Hybrid Techniques Based on Inverse Monte-Carlo

An inverse Monte-Carlo technique is an iterative method that attempts to fit Monte-Carlo simulated data to measured reflectance or transmittance spectra. The simulated spectra is generated using a forward Monte-Carlo algorithm for a vector of given optical properties (μ_a, μ_s', g). The fit can then be obtained using any optimisation algorithm but is often achieved using non-linear techniques such as least squares estimation.

However, obtaining an accurate representation of optical spectra using Monte-Carlo requires the use of a large number of photons, making the forward simulation a computationally expensive operation. The iterative nature of the inversion process further increases the computational cost as multiple forward simulations are required to generate

the spectra that will be compared with measured data. This can therefore, hinder the use of such inverse Monte-Carlo techniques especially if the result of the inversion process is required in real-time.

Consequently, many hybrid techniques have emerged that use a combination of Monte-Carlo methods with other less expensive techniques to solve the inversion problem (Yaroslavsky et al., 1996). Such techniques incorporate a Monte-Carlo algorithm and an analytical method to provide accurate results while saving computation time. One such method uses Kubelka-Munk equations to obtain a crude first estimate of the optical properties of the sample. These values then become the initial guesses that will be used by the delta-Eddington method (Hammer and Schweitzer, 1976) to simulate spectra as part of the inversion part of the algorithm. This reduces the number of Monte-Carlo forward computations required and was proved to provide accurate results without the prohibitive cost of multiple Monte-Carlo simulations (Yaroslavsky et al., 1996; Salomatina and Yaroslavsky, 2008; Hammer et al., 1995).

Hammer *et al.* (Hammer et al., 1995) used the double integrating sphere technique with inverse Monte-Carlo simulations to calculate μ_a, μ_s and g from *in vitro* measurements of reflectance and transmittance on the ocular fundus. They were able to determine the anisotropy factor g for longer wavelengths and assumed the values to hold for the entire wavelength range. The results were reproducible for the same individual with $\pm 2\%$ variations in the parameters. However, the inter-individual difference reached $\pm 20\%$ for the absorption and scattering coefficients and $\pm 5\%$ for the anisotropy factor. This was due to the rigidity of the model as it did not cater for the individual differences in thicknesses and blood and water content (Hammer et al., 1995).

Hidovic and Rowe (2004) devised an error correction method that combines the speed of the Kubelka-Munk method and the accuracy of MCML to solve the inversion problem. They initially set the error correction model to be zero, and solve the inverse problem using the Kubelka-Munk model. They then run a Monte-Carlo based model near the solution obtained in the previous step and use this to update the error correction model.

They then attempt to solve the inverse problem again using the Kubelka-Munk model, plus the updated error model and repeat this process as many times as necessary (Hidovic and Rowe, 2004; Hidovic-Rowe et al., 2006). This hybrid method is used in our work and is described in details in Chapter 6 and Appendix B.

3.4.2 Inverse Adding Doubling (IAD)

The Inverse Adding-Doubling method consists of three main steps (Prahl, 1993). Firstly, an initial set of the optical properties is provided to the algorithm. For instance, if the parameters to be recovered are μ_a and μ'_s, then the forward algorithm is run with pre-set initial values for these parameters (μ_{a_0}, μ'_{s_0}). A careful choice of these guesses can lead to fewer iterations, and thus, a quicker convergence.

However, a poor starting point will often increase the possibility of the minimisation algorithm converging to a local rather than a global minimum. To deal with this possibility, the IAD algorithm provides the option of checking the acquired minimum against a pre-set tolerance threshold (Prahl, 1993). If the minimum exceeds the threshold, it is deemed incorrect, discarded and the iteration process is restarted.

The second step is to calculate the reflection and transmission using the forward adding-doubling method. Like other indirect methods however, the main problem with the recovery process stems from the fact that errors may be introduced at this stage. This is due to inaccuracies in the forward model caused by the use of crude estimates when the properties of the tissue are not well documented (Prahl, 1993).

Finally, the values calculated using the forward model are compared with the measured reflectance and transmittance, then the previous steps are repeated until a set of parameters that can generate the measured spectra is reached (Prahl, 1993). This set will subsequently be considered as the set of optical properties of the medium.

This method was initially suggested by Prahl (Prahl et al., 1991, 1993a,b). It was later used by Hammer and Schweitzer to calculate the concentrations of xanthophyll in the

retina; the melanin in the retinal pigment epithelium and choroid; and haemoglobin in the choroid from fundus reflection spectra (Hammer and Schweitzer, 1976). According to Prahl, "*the results obtained using the IAD method are accurate for all optical properties and can be made arbitrarily precise at the cost of increased computation time*" (Prahl et al., 1993b). In fact, the IAD method generates results with a maximum error value of 2-3% for most reflection and transmission quantities. Furthermore, the validity of the IAD method for samples where the absorption and scattering coefficients are close is worth noting as most other inversion methods (based on the diffusion approximation) fail in this situation (Prahl et al., 1993b).

3.5 Other Optical Parameter Recovery Methods

Other methods used to recover the optical parameters of biological tissues include iteratively improving the fit between time-resolved spectra and modelled data as demonstrated by Matcher *et al* in (Matcher et al., 1997). In (Corlu et al., 2003, 2005), Corlu *et al.* describe their technique for inverting continuous-wave data in multi-spectral diffuse optical tomography. Much work was also done to develop physics based approaches that make use of multi-spectral imaging, and the knowledge that the colouration of the medium varies with differing tissue histology (Claridge and Preece, 2003; Preece and Claridge, 2004; Preece et al., 2005; Styles et al., 2006). The aim of these methods is to estimate the quantities of chromophores at each pixel and show how they are distributed across the image. This can allow the early detection of anomalies in the tissue structure.

Patterson *et al* (Patterson et al., 1989, 1991) developed a simple model based on the diffusion approximation of the radiative transport equation which resulted in analytical expressions for temporal and spacial dependence of reflected and transmitted light. There results were in accordance with preliminary *in vivo* experiments and Monte-Carlo simulations. However, the only parameters recovered were μ_a and μ_s' rather than the chromophores concentrations and scattering anisotropy factor.

Some reports on the use of Monte-Carlo forward simulations with look-up table for parameter recovery appear in the literature. A Monte-Carlo model for light transport is used to generate simulated spectra using a set of all possible values of the optical parameters. These spectra are then stored as a look-up table and the measured spectra is iteratively compared with the stored data until a best fit is obtained. This method makes use of the accuracy of Monte-Carlo forward modelling while reducing the computational cost of multiple simulations in the inversion process. It was used by (Simpson et al., 1998) to retrieve the absorption and scattering coefficients, as well as the anisotropy factor of *ex-vivo* human skin and subcutaneous tissues from reflectance and transmittance measurements obtained using a single integrating sphere.

The accuracy of this method was shown to be acceptable for retrieving the optical parameters of different tissue types such as tissues from limbs, the head and the abdomen. This was checked for solid phantom data by comparing the coefficients produced using his method against the analysis of the time point spread function (TPSF). The retrieved scattering coefficients were in good agreement with a 5% variability while the absorption coefficient showed errors of up to 20% (Simpson et al., 1998).

While most existing method are successful in retrieving the absorption and scattering coefficient of tissues whose physical properties are well defined, they may not perform as well when such properties are missing or not precise. This is because such methods rely on the correctness and accuracy of the forward model used during the inversion process and assume a very low level of uncertainty.

In addition, estimating the unknown optical coefficients of a tissues is sometimes achieved by first recovering the absorption and scattering coefficients from reflectance and transmittance spectra. This is followed by fitting a linear combination of the extinction coefficients of known chromophore to the absorption spectra to recover the chromophore concentrations. This requires the absorption coefficient to be recovered at many wavelengths. A similar process is used to recover the scatterer size and density which are calculated through fitting the scattering coefficient estimated from measured spectra. This, in combination

with the uncertainty inherently present in the model used, could amplify errors while quantifying the parameters of the tissue.

In order to address these problems, we propose to develop an inversion method that provides estimates for the properties of a biological tissue even if some of its physical characteristics are not well known by using Bayesian estimation. Additionally, the optical properties of the tissue are estimated directly from reflectance and / or transmittance spectra. This is achieved by re-parameterising the model so that the unknown entities are the chromophore concentrations and scatterer size and density instead of the absorption and scattering coefficients. We thus have fewer values to recover, which leads to fewer measurements being required. The next section offers a brief introduction to some estimation techniques that could be used in the inversion process.

3.6 Introduction to Estimation Theory

Estimation theory is used as the basis of many signal processing systems such as radar systems, biomedicine and image analysis (Stewart, 1999; Kwee, 1999; De Pierro and Amagishi, 2001; Hanson, 1993). In these domains, the goal is often to estimate the values of certain parameters such as an object's position or a tissue's characteristics from measured data such as signals and images. An estimator may be thought of as a rule that assigns a value to the unknown parameter θ for each realisation of the data. In general, the unknown parameter is used to describe a set of properties that affect the distribution of the measured data. Thus, the goal of the estimator is to find the most probable value for θ that provides the best fit between measured and modelled data.

For the remainder of this section, we will need to define a few components that will be used in the choice and construction of our estimator. For the problems of interest in this thesis, the first component describes the observed data $\mathbf{x}$ which represent reflectance measurements as a vector of observation samples $\mathbf{x} = (x[\lambda_0], x[\lambda_1], \ldots, x[\lambda_{N-1}])^{\mathrm{T}}$ where $x[\lambda_i]$ is the measured reflectance at wavelength λ_i. Secondly, we may need to retrieve more than a single parameter. Consequently, θ will represent a scalar parameter (in case

of a single unknown) while $\boldsymbol{\theta}$ will represent a vector of all unknown parameters if there are more than one. We write $\boldsymbol{\theta} = (\theta_1, \theta_2, \ldots, \theta_m)^{\mathrm{T}}$ with θ_j describing the j^{th} unknown parameter.

As stated earlier, the goal of an estimator is to find the most probable value for θ given a realisation of $\mathbf{x}$. That is, the value of θ that maximises $p(\mathbf{x};\theta)$, the probability density function (PDF) parameterised by θ and defined as $p(\mathbf{x};\theta) = p(\mathbf{x}|\theta)p(\theta)$ where $p(\mathbf{x}|\theta)$ is a conditional PDF that abstracts the knowledge provided by the data $\mathbf{x}$ conditioned on knowing θ and $p(\theta)$ is the prior abstracting our knowledge about θ before $\mathbf{x}$ is observed.

One of the main requirements for our method is for the PDF to be robust, i.e., slight alterations to our forward model will not severely affect the performance of the estimator. The rest of this section describes a number of popular estimation techniques that can be used to recover parameter values.

3.6.1 Minimum Variance Unbiased Estimation (MVU)

An intuitive estimator is one that minimises the mean-squared error, that is, the expected squared deviation of the estimated parameter value from the true one. For a scalar parameter, the mean-square error is defined by (3.2):

$$\begin{aligned} mse(\hat{\theta}) &= E[(\hat{\theta} - \theta)^2] \\ &= var(\hat{\theta}) + bias^2(\theta) \qquad \text{where} \qquad (3.2) \\ var(\hat{\theta}) &= E(\hat{\theta} - E(\hat{\theta}))^2 \qquad (3.3) \\ bias(\theta) &= E(\hat{\theta}) - \theta \qquad (3.4) \end{aligned}$$

However, such estimators do not generally exist as they depend on the bias (3.4), which is a function of θ. As a consequence, the optimal value of the estimator will depend on θ, making the estimator unrealisable. One possible alternative is to find an estimator that minimises the variance (3.3) with the bias being set to zero. Such methods are called Minimum Variance Unbiased estimators (MVUs).

An estimator $\hat{\theta}$ is called unbiased if its bias is zero for all values of the unknown parameter θ. In other words, for any value of θ in the range $[a, b]$, our estimator will yield the true value of θ (on average). It is important to note that although bias will always result in a poor estimator, an unbiased one is not necessarily good, but it is guaranteed to reach the true value of the unknown parameter (on average).

$$E(\hat{\theta}) = \theta \qquad \text{for} \quad a < \theta < b$$

However, minimum variance unbiased estimators do not always exist as it is often the case that no single estimator can have a minimum variance for all values of θ. Nevertheless, there exist methods that would enable us to find such estimators when they exist such as the Cramer-Rao Lower Bound and the concept of sufficient statistics. These methods will not be used in this thesis but further information about these concepts can be found in (Kay, 1993; Gibson, 2005; Olive; Faris, 2009).

3.6.2 Least Squares Estimation (LSE)

As stated in 3.6.1, designing an estimator might be reduced to minimising the discrepancy between the estimate and the true value of the parameter θ (Kay, 1993). An alternative to this method is the Least Squares Estimation. This method uses a forward model of the studied system, and attempts to minimise the squared difference between the observed data $\mathbf{x}$ and the noiseless data $\mathbf{x}'$ produced by the model (Kay, 1993).

When applied to our problem, we use a forward model of light propagation within the biological tissue we wish to study and aim to minimise the squared difference between the measured reflectance R or transmittance T and the data produced by our forward model. Because the model will depend on the unknown parameter θ, we choose the realisation of θ that makes the value $\mathbf{x}'$ produced by the model closest to the observed data $\mathbf{x}$. This can be abstracted by the *LSE* criterion as:

$$LSE\,(\theta) = \sum_{i=1}^{N} (x[\lambda_i] - \mathbf{x}'(\theta, \lambda_i))^2 \tag{3.5}$$

and the value of θ that minimises $LSE(\theta)$ is the LS estimate (Kay, 1993).

Although no claims can be made about its optimality, as this depends on the quality of the forward model, this method is widely used (particularly in signal processing) due to its ease of implementation. For linear models, this method can also be easily extended to a vector parameter by describing $\mathbf{x}'$ as $\mathbf{x}' = \mathrm{M}\boldsymbol{\theta}$ with M being a known $N \times m$ matrix often referred to as the *observation matrix* (Kay, 1993).

When applied to our inversion problem, however, we note that the model $\mathbf{x}'(\boldsymbol{\theta})$ can not be expressed directly in terms of $\mathrm{M}\boldsymbol{\theta}$, as it is non-linear. The minimisation of *LSE* can thus only be achieved iteratively. The minimisation process can be completed using any of the techniques described in sections 3.3.3, 3.3.4 and 3.3.5.

3.6.3 Maximum Likelihood

When MVU estimators do not exist or cannot be found, the most popular alternative is the Maximum Likelihood estimation method (Kay, 1993). This method is mostly used to obtain practical estimators instead of focusing on optimal ones. The likelihood function, upon which this method is based, is the PDF viewed as a function of θ with a fixed value of $\mathbf{x}$. Because an actual realisation of $\mathbf{x}$ is used, the likelihood function varies according to the outcome of the measurement process such that two different outcomes of the same experiment will lead to two different likelihood functions (Kay, 1993).

The maximum likelihood estimator (Kay, 1993; MacKay, 2003) is defined as the value of $\hat{\theta}$ that maximise the $p(\mathbf{x};\theta)$ for a realisation $\mathbf{x}_0$ of $\mathbf{x}$. This maximisation will be performed over the allowable range of θ. When the PDF is evaluated for an actual realisation $\mathbf{x}_0$, the value of $p(\mathbf{x} = \mathbf{x}_0;\theta)$ for each θ will give us the probability of observing $\mathbf{x}$ in the region centred around $\mathbf{x}_0$ assuming the given value of θ (Kay, 1993; MacKay, 2003).

$$\hat{\theta} = argmax\, p(\mathbf{x};\theta) \tag{3.6}$$

Due to its practicality, most estimators are based on the maximum likelihood principle. In addition, it is believed that for large data records, a maximum likelihood estimator is both efficient and unbiased, making it an "*optimal*" estimator (Kay, 1993). Another advantage of the MLE is that for a given data set, it can always be found numerically. This is because the maximum likelihood estimator finds the maximum of a known function (the likelihood function) (MacKay, 2003). However, because the likelihood function is based on a realisation of $\mathbf{x}$, a change in the data set will undoubtedly lead to a change in estimator. Consequently, the use of a new set of data will require running the maximisation algorithm (often based on a grid search) again (Kay, 1993).

Although both the least-squares and maximum-likelihood methods will provide good estimators, it is believed that their accuracy could be improved by incorporating any prior knowledge one might have about the unknown parameter. For example, when trying to estimate the thickness of a biological tissue, we might know that it falls within a known interval. Thus, any good estimator will only produce estimates within this range. However, the unknown parameter θ (in all previous methods) was assumed to be a deterministic variable, an assumption that makes it hard to incorporate any prior knowledge that we might have about θ into our estimator (Jagajothi and Raghavan, 2009; Kay, 1993).

To address these issues, we will consider an example of the Bayesian approach to estimation, namely the maximum *a posteriori* method where the parameter θ will be thought of as a random variable, making it possible to assign a prior PDF $p(\theta)$ to it. As suggested by the name, Bayesian estimation is inspired by Bayes theorem which describes the posterior probability of a hypothesis θ in terms of the prior probabilities of θ and observed data $\mathbf{x}$, and the likelihood of $\mathbf{x}$ given θ (Jagajothi and Raghavan, 2009).

3.6.4 Maximum *A Posteriori* Method (MAP)

The maximum *a posteriori* estimator for θ in terms of $\mathbf{x}$ is $MAP_\theta = argmax\, p(\theta|\mathbf{x})$ with $p(\theta|\mathbf{x})$ described by equation (3.7) (Hanson, 1993; Kay, 1993). The posterior PDF $p(\theta|\mathbf{x})$ refers to the PDF of θ *after* the data has been observed when $p(\theta) = \int p(\mathbf{x}, \theta) d\mathbf{x}$ represents

the prior PDF

$$p(\theta|\mathbf{x}) = \frac{p(\mathbf{x}|\theta)p(\theta)}{p(\mathbf{x})} = \frac{p(\mathbf{x}|\theta)p(\theta)}{\int p(\mathbf{x}|\theta)p(\theta)d\theta} \tag{3.7}$$

As shown in equation (3.7), the goal of *MAP* is to maximise the posterior probability density function. It can also be observed that the maximisation of $p(\theta|\mathbf{x})$ can be achieved by maximising $p(\mathbf{x}|\theta).p(\theta)$ or equivalently, maximising $ln\ p(\mathbf{x}|\theta) + ln\ p(\theta)$.

$$\hat{\theta} = argmax(p(\mathbf{x}|\theta).p(\theta)) \tag{3.8}$$

To extend this method to the vector case $\boldsymbol{\theta}$, it suffices to define the estimator $\hat{\boldsymbol{\theta}}$ as a vector $(\hat{\theta}_0, \hat{\theta}_1, \hat{\theta}_2, ..., \hat{\theta}_{m-1})^{\mathrm{T}}$ with $\hat{\theta}_i = argmax\ p(\theta_i|\mathbf{x})$ and $i = 0, 1, 2..., m-1$ (Kay, 1993) which will also minimise the cost function C($\boldsymbol{\theta}$, $\hat{\boldsymbol{\theta}}$) which determines the cost of an estimate $\hat{\boldsymbol{\theta}}$ when the truth is $\boldsymbol{\theta}$ (Kay, 1993).

Nevertheless, using this estimator removes an important advantage belonging to the scalar parameter case. This advantage is that to numerically determine the estimator, one needs only to maximise $p(\mathbf{x}|\theta)p(\theta)$. However, $p(\theta_i|\mathbf{x})$ can only be calculated by equation (3.9) (Kay, 1993) making integration necessary to maximise the PDF, and thus losing an important advantage of maximum *a posteriori*.

$$p(\theta_i|\mathbf{x}) = \int \dots \int p(\boldsymbol{\theta}|\mathbf{x})d\theta_{i+1}...d\theta_m \tag{3.9}$$

Another version of the MAP estimator for vector parameters, which attends to this issue, can be described by equation (3.10). The posterior PDF for the vector parameter is directly maximised, and thus eliminating the need for integration to obtain PDFs for each component of $\boldsymbol{\theta}$.

$$\begin{aligned} \hat{\boldsymbol{\theta}} &= argmax\, p(\boldsymbol{\theta}|\mathbf{x}) \\ &= argmax\, p(\mathbf{x}|\boldsymbol{\theta})p(\boldsymbol{\theta}) \end{aligned} \tag{3.10}$$

3.7 Applications of Estimation Theory in Biomedical Imaging

Estimation theory is often used in medical image analysis to various goals such as noise reduction, image reconstruction and parameter recovery. For instance, maximum likelihood is often used in emission tomography to construct images with superior noise characteristics. One of the earliest application of estimation in medical image analysis was to single photon emission tomography by Geman and McClure who reconstructed a profile of isotope intensity from observations of photon emissions (Geman and McClure, 1985). Geman and McClure experimented with an expectation maximisation (EM) algorithm (Dempster et al., 1977) to find the maximum likelihood estimates; and maximum *a posteriori* (Geman and McClure, 1985).

Also in emission tomography, DePierro and Yamagishi (De Pierro and Amagishi, 2001) proposed an extension to the ordered subsets expectation maximisation algorithm developed by Hudson and Larkin based on the expectation maximisation algorithm (Hudson and Larkin, 1994). The aim was to solve the maximum *a posteriori* model for emission tomography (De Pierro and Amagishi, 2001).

In 1999, Doornbos *et al* measured the *in vivo* human tissue optical properties and chromophore concentrations from diffuse reflection measurements using the diffusion approximation to the RTE and a non-linear least-square fitting algorithm (Doornbos et al., 1999; Press et al., 1989). Fitting the data resulted in the calculation of the absorption and reduced scattering coefficients. The singular value decomposition and related (covariance) algorithms (Press et al., 1989) were then used to estimate the chromophore concentrations.

Williams *et al* also used estimation techniques to recover tissue parameters in (Williams and Noble, 2004; Williams et al., 2005). They initially recovered the parameters of interest using Bayesian Factor Analysis - Markov Random Field method (Williams and Noble, 2004). Williams *et al* then used maximum a Posteriori to analyse myocardial blood flow and reserve by estimating the two quantitative perfusion indices (Williams et al., 2005).

Their results were used to identify abnormalities in the different regions of the myocardium, and their accuracy was improved by the inclusion of the prior information obtained from the BFA model.

3.8 Conclusion

In this chapter, we described how parameter recovery could be reduced to an optimisation problem where the aim is to minimise the difference between modelled and measured spectra. We also introduced a number of optimisation algorithms that can be used to recover a tissue's parameters and outlined the various limitations of using these algorithms. Finally, we briefly introduced three estimation techniques, namely: least-squares, maximum likelihood and maximum *a posteriori* methods and described how they can be used to solve parameter recovery problems.

In the remainder of this thesis, we apply a method based on the maximum *a posteriori* technique to simulated reflectance spectra, transmittance and reflectance data from gelatin phantoms as well as multi-spectral images of the human colon and analyse the results to evaluate the potential of our technique for parameter recovery in tissues where uncertainty is high.

Chapter 4

Application to Simulated Data: Human Skin

4.1 Introduction

The skin is probably one of the most investigated biological tissues as demonstrated by the large number of related literature (Anderson et al., 1981a; Bashkatov et al., 2011; Cotton et al., 1999, 1997; Dawson et al., 1980; Meglinski and Matcher, 2003; Sandby-Moller et al., 2003; Jacques, 1998; Ryan, 1991; Simpson et al., 1998; Van Gemert et al., 1989; Yudovsky and Pilon, 2011; Zonios et al., 2001). There exist numerous optical models aimed at studying the quantification and spacial distribution of the skin's component.

It is also a medium that has often been used to illustrate the effectiveness of parameter-recovery methods due to the ease of access to samples of different types (normal, lesions and cancerous tissues). However, the characteristics of human skin can vary enormously amongst individuals from colour to thickness, which introduces uncertainty when recovering its optical properties. It is, thus, a good example of a biological medium that can be used to demonstrate the potency of our estimation technique.

This chapter describes how we use the human skin to demonstrate the feasibility and accuracy of our inversion method. We first give a detailed description of the structure of the human skin. We also describe how light reflectance is modelled in the skin and the various parameters required to construct such a model. We then apply our inversion method to reflectance spectra simulated using the aforementioned model. Finally, we analyse

the results in comparison with classical estimation techniques, namely: least squares and maximum likelihood.

4.2 Structure of the Human Skin

As shown on Figure 4.1, skin is essentially a collection of three layers: The epidermis, dermis and hypodermis (Anderson et al., 1981a). The epidermis can be further divided into a stratum corneum and a living epidermis. The stratum corneum contains dead cells and no absorbing agents and is thus responsible for specular reflection. Any light that was not reflected at the skin-air interface is scattered forward into the remaining layers.

The living epidermis contains melanocytes and keratin fibres making epidermal absorption mainly dependent on melanin absorption. The light that does not get absorbed or reflected in this layer is transmitted to the dermis (Ryan, 1991).

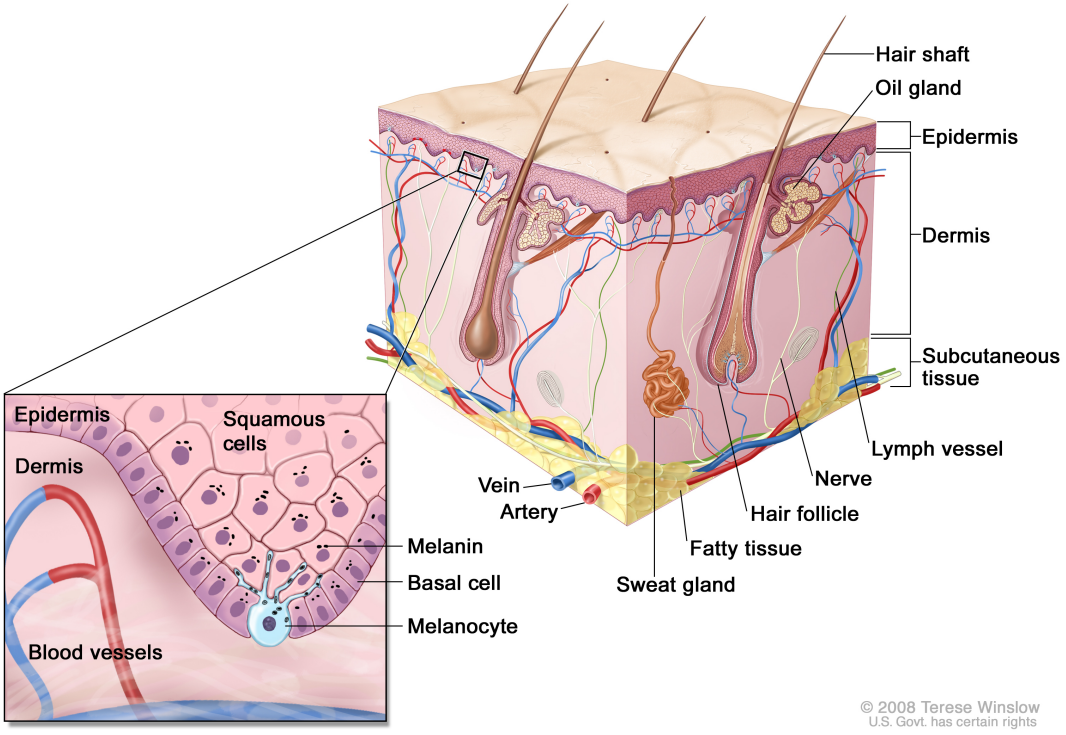

Figure 4.1: The Cutaneous Layers (Quade, 2008)

The dermis mainly consists of connective tissue and blood vessels; and can be divided into papillary and reticular regions (Cotton et al., 1997). The papillary dermis consists of loose areolar connective tissue and is separated from the reticular dermis by a thin superficial vascular network. The reticular region is composed of dense irregular connective tissue, and receives its name from the dense concentration of collagenous, elastic, and reticular fibres that weave throughout it (Cotton et al., 1997; Ryan, 1991). The dermis is separated from the hypodermis, a layer containing cells responsible for fat storage, by a vascular networks of larger blood vessels (Ryan, 1991).

In vitro, bloodless dermis was found to be highly scattering due to the presence of collagen fibres and none of the incident light was absorbed (Anderson et al., 1981a). Consequently, haemoglobin and oxyhaemoglobin are believed to be the main absorbing agents in the dermis *in vivo*. The light that is not absorbed by haemoglobin is either scattered forward towards the hypodermis or backward towards the epidermis. In the latter case, some of it is absorbed by melanin pigment where the remaining exits from the stratum corneum. This results in the brown colour of the skin. However, the light that reaches the hypodermis will either be absorbed or travel through this thick layer. Consequently, it will not contribute to the amount of light reflected, and the hypodermis can thus be ignored (Meglinski and Matcher, 2003).

As a result, we take epidermal melanin and dermal haemoglobin and oxy-haemoglobin to be the only absorbing agents present in our medium in the visible light range. This makes the parameter to be estimated $\boldsymbol{\theta} = (\mathrm{C}_{\mathrm{HB}*}, \mathrm{C}_{\mathrm{Mel}})^{\mathrm{T}}$ where $\mathrm{C}_{\mathrm{HB}*}$ and $\mathrm{C}_{\mathrm{Mel}}$ represent the concentrations of haemoglobin and melanin per unit volume of tissue. Note that the terms “concentration” and “volume fraction” will be used interchangeably throughout this thesis.

Figure 4.2 shows the extinction coefficients of skin pigments as reported in (Cotton et al., 1997; Prahl, 2007a). Also in the visible spectral range, the collagen fibres in the dermis and keratohyalin granules are responsible for most of the scattering that occurs inside the skin (Meglinski and Matcher, 2003). In fact, the scattering in the epidermis is

much lower than dermal scattering due the comparatively small thickness of the epidermis, and is thus ignored (Matcher, 2001).

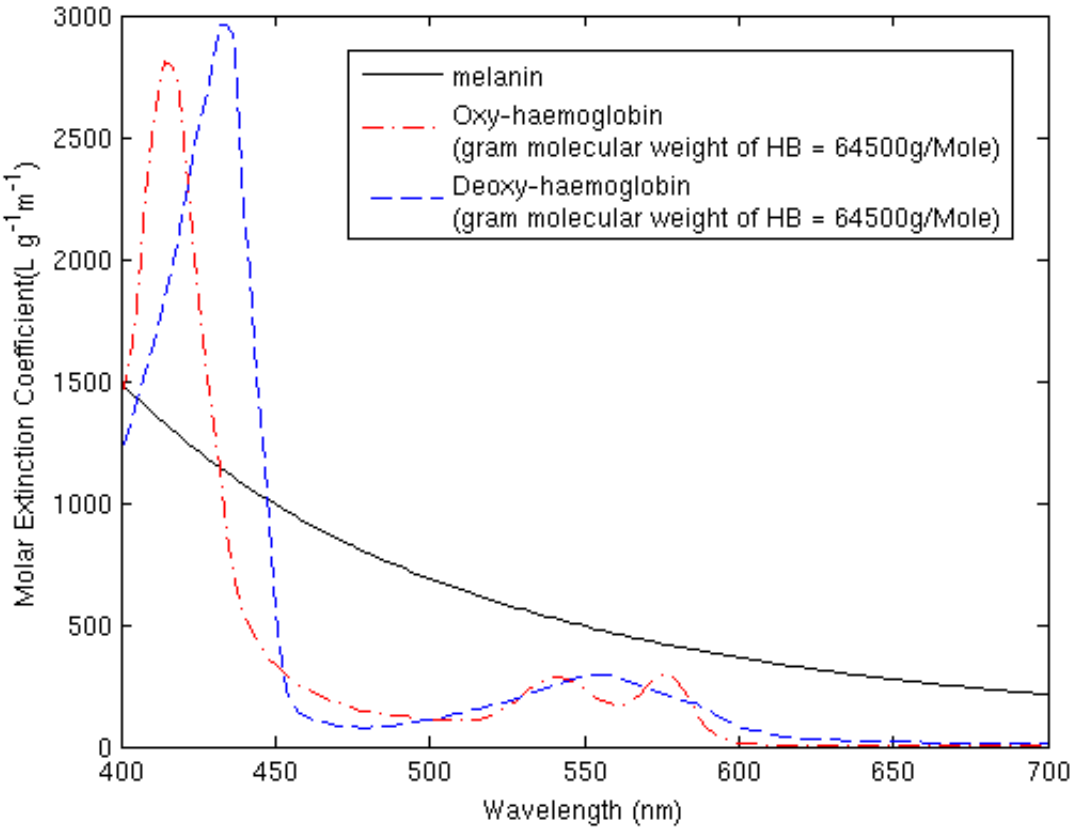

Figure 4.2: Molar extinction coefficient spectra for melanin, oxy- and deoxy-haemoglobin (Data from Prahl (2007a))

4.3 The Forward Model

Using our knowledge of the multi-layered structure of the skin, we develop a model of light propagation by considering some of the various instances present in the literature. One such model of colour formation in the skin, based on the Kubelka-Munk theory for inhomogeneous materials, was developed by Cotton (Cotton et al., 1997; Cotton, 1998; Cotton et al., 1999; Claridge et al., 2003). It presumes that the skin consists of four layers: stratum-corneum, epidermis, papillary dermis and reticular dermis. In this model, the first layer is responsible for specular reflectance, the second and third for melanin

and blood absorption respectively; and the last for general scattering. Cotton's model was successfully used for physics-based interpretation of images of pigmented skin legions (Claridge et al., 2003).

Meglinski and Matcher also developed a skin model as part of their parameter recovery technique, which was described in (Meglinski and Matcher, 2003). Their model uses a wavelength-independent scattering coefficient and wavelength dependent haemoglobin and water absorption coefficients. The spatial distribution of blood, melanin and water (as the main absorbents) within the different layers are taken into account to accurately model light propagation in skin. Unlike Cotton's model, these coefficients are converted to reflectance intensity using a Monte-Carlo based method. The resulting reflectance curves are then fitted using a multi-linear regression algorithm in order to recover the optical properties of interest (Matcher, 2001).

When investigating the possible effects of photon behaviour on spectral images of the human skin, Binzoni *et al.* also described a model of the human skin. They used a Monte-Carlo based algorithm to convert the absorption and scattering coefficients into diffuse reflectance spectra. The model is described in details in (Binzoni et al., 2008). Binzoni's model is heavily based on Meglinski and Matcher's (Meglinski and Matcher, 2003) with the main difference being the inclusion of the hypodermis and its scattering coefficient.

We therefore combine the findings of the aforementioned works, by modelling the skin as the multi-layered structure described in Meglinski and Matcher's and Binzoni *et al.* works. We then apply the Kubelka-Munk method to convert the optical properties into reflectance spectra. We choose this model due to its simplicity and the fact that it has been shown to be suitable for modelling light travel in the human skin as reported in (Anderson et al., 1981b; Van Gemert et al., 1989; Cotton, 1998). However, such a simplified skin model can only be used under some assumptions. Firstly, we accept that the skin can be modelled as a collection of a fixed number of layers, six in this instance. Secondly, we assume that each layer is homogeneous.

Unlike the models described in (Binzoni et al., 2008) and (Meglinski and Matcher, 2003), we take the scattering coefficient of the skin to be wavelength-dependent and consists of both Mie and Rayleigh scattering components. The physical properties of each layer are described in Table 4.1 where $d\,(\mu\text{m})$ is the layer thickness, $\text{C}_{\text{HB}*}$ is the haemoglobin concentration, S is the oxygen saturation, C_{Mel} is the melanin concentration, g is the anisotropy factor and n is the refractive index for each later.

Layer	$d\,(\mu\text{m})$	$\text{C}_{\text{HB}*}$	S	C_{Mel}	g	n
Stratum corneum	20	0.00	0.00	0.00	0.86	1.50
Living epidermis	80	0.00	0.00	C_{Mel_0}	0.80	1.34
Papillary dermis	160	$\text{C}_{\text{HB}*_0}$	0.98	0.00	0.90	1.40
Upper blood dermis	100	$\text{C}_{\text{HB}*_0}$	0.98	0.00	0.95	1.34
Reticular dermis	1400	$\text{C}_{\text{HB}*_0}$	0.98	0.00	0.80	1.40
Deep blood dermis	100	$\text{C}_{\text{HB}*_0}$	0.98	0.00	0.95	1.38

Table 4.1: Skin Model Parameters as summarised by Binzoni et al. (2008). $\text{C}_{\text{HB}*_0}$ and C_{Mel_0} represent the haemoglobin and melanin concentrations for the skin layers. Note that no single value is given as $\text{C}_{\text{HB}*_0}$ and C_{Mel_0} will be varied to simulate various sets of reflectance data while all other parameters remain fixed.

In the remainder of this section, we will describe the absorption and scattering coefficients of individual layers, and the various equations used to derive these parameters. Throughout this chapter, all optical coefficients and reflectance/transmittance spectra is assumed to be given for wavelengths between 300 nm and 800 nm.

4.3.1 Absorption

As stated in Section 4.2, the stratum corneum is free of absorbing agents with the exception of water. Binzoni et al. (2008) found that the absorption coefficient for the stratum corneum μ_a^{sc} can be calculated by Equation (4.1) where $\text{C}_{\text{H}_2\text{O}} = 5\%$ and $\mu_a^{\text{H}_2\text{O}}$ are the volume fraction and absorption coefficient of water, respectively. We take μ_a^{base} to represent the absorption coefficient of skin free of any absorbents. Binzoni et al. (2008) show that this quantity can be estimated at each wavelength λ as $\mu_a^{\text{base}}(\lambda) = 7.84 \times$

$10^8\lambda^{-3.255}\,\mathrm{cm}^{-1}$.

$$\mu_a^{\mathrm{sc}}(\lambda) = ((0.1 - 3 \times 10^{-5}\lambda) + 0.125\mu_a^{\mathrm{base}}(\lambda))(1 - \mathrm{C}_{\mathrm{H_2O}}) + \mathrm{C}_{\mathrm{H_2O}}\mu_a^{\mathrm{H_2O}}(\lambda) \tag{4.1}$$

The remaining layers can each be abstracted as a base layer with an absorption coefficient μ_a^{base}, with a certain concentration of haemoglobin and/or melanin ($\mathrm{C}_{\mathrm{HB}*}$ and $\mathrm{C}_{\mathrm{Mel}}$ respectively). The absorption coefficient μ_a^{k} of layer k can therefore be described as the sum of the absorption coefficients of its components, and calculated by Equation (4.2) where μ_a^{Hb}, $\mu_a^{\mathrm{HbO_2}}$ and μ_a^{mel} represent the absorption coefficients of haemoglobin, oxyhaemoglobin and melanin, respectively.

$$\begin{aligned}\mu_a^{\mathrm{k}}(\lambda) = & \quad \mu_a^{\mathrm{blood^k}}(\lambda) + \mu_a^{\mathrm{melanin^k}}(\lambda) \quad + \mu_a^{\mathrm{base}}(\lambda) \\ = & \quad ln(10).\mathrm{C}_{\mathrm{HB}*}^{\mathrm{k}}\left((1 - S^{\mathrm{k}})\mu_a^{\mathrm{Hb}}(\lambda) + S^{\mathrm{k}}\mu_a^{\mathrm{HbO_2}}(\lambda)\right) + \mathrm{C}_{\mathrm{Mel}}^{\mathrm{k}}\mu_a^{\mathrm{mel}}(\lambda) \quad + \mu_a^{\mathrm{base}}(\lambda)\end{aligned} \tag{4.2}$$

As the data available in the literature only provides values for the extinction coefficients of oxy- and deoxy-haemoglobin, these are converted to absorption coefficients using Equation (4.3) where 64500 g/mole is the molecular weight of haemoglobin, and 150 g/L is the standard concentration of haemoglobin per litre of blood in the skin (Prahl, 2007a).

$$\mu_a^{\mathrm{Hb}*} = \frac{150\,(\mathrm{g/l})}{64500\,(\mathrm{g/mole})} \cdot \varepsilon_{\mathrm{Hb}*} \tag{4.3}$$

The values for $\varepsilon_{\mathrm{Hb}}$ and $\varepsilon_{\mathrm{HbO_2}}$ are available from the Oregon Medical Laser Center's website (Prahl, 2007a) as look-up tables. The absorption coefficient of melanin is calculated as described by Prahl (2007b) using $\mu_a^{\mathrm{mel}}(\lambda) = 1.70 * 10^{12}\lambda^{-3.48}(\mathrm{cm}^{-1})$ as this was shown to be a close approximation to the melanin absorption coefficient recorded using an in-vivo optical fibre spectrometer (Prahl, 2007b).

4.3.2 Scattering

As stated in Section 4.1, the thinness of the epidermis makes the details of the epidermal scattering coefficient of minor importance in the visible light range. Consequently, dermal scattering can be used to describe skin scattering in this instance (Binzoni et al.,

2008). We use Equation (4.4) to describe the reduced scattering coefficient for both the living epidermis and the dermis while we calculate the reduced scattering coefficient of the stratum corneum as $\mu_s'^{sc} = 10^3 * (1 - g_{sc})\,\mathrm{cm}^{-1}$ where $g_{sc} = 0.86$ (Meglinski and Matcher, 2003). Note that although the scattering coefficient of the stratum corneum normally decreases between 450 and 700 nm, we accept the value cited by Meglinski and Matcher (2003) as an approximation that would simplify the forward model without having a large effect on our results.

$$\begin{aligned} \mu_s'(\lambda) &= \mu_s'^{Rayleigh}(\lambda) + \mu_s'^{Mie}(\lambda) && \text{where} \\ \mu_s'^{Mie}(\lambda) &= 2 * 10^5 \lambda^{-1.5} && (\mathrm{cm}^{-1}) \\ \mu_s'^{Rayleigh}(\lambda) &= 2 * 10^{12} \lambda^{-4} && (\mathrm{cm}^{-1}) \end{aligned} \tag{4.4}$$

Next, we convert the individual layer's absorption and reduced scattering coefficients to diffuse reflectance spectra for the whole medium. To that aim, we extend the Kubelka-Munk equations in Section 2.4.2 to cater for the multi-layered structure of the skin. As described by Dawson *et al.* (Dawson et al., 1980), this can be achieved for a four-layered structure, described in Figure 4.3, by assuming a two flux model in which light from layer i is either reflected back, or transmitted forward to layer $i + 1$ such that the intensity of the reflected light is given by Equation (4.5) where I_o is the initial intensity of light.

$$I = I_o(R_1 + T_1^2 R_2 + T_1^2 T_2^2 R_3 + T_1^2 T_2^2 T_3^2 R_4) \tag{4.5}$$

Consequently, we use the following equations developed by Cotton (Cotton, 1998), which, in a multi-layered structure, provide the reflectance and transmittance coefficients of a layer recursively:

$$R_{12\ldots n} = R_{12\ldots n-1} + \frac{T_{12\ldots n-1}^2 R_n}{1 - R_{12\ldots n-1} R_n} \tag{4.6}$$

$$T_{12\ldots n} = \frac{T_{12\ldots n-1} T_n}{1 - R_{12\ldots n-1} R_n} \tag{4.7}$$

We take $R_{12..i}$ and $T_{12..i}$ to be the reflectance and transmittance intensities of the combined layers up to layer i. R_i, T_i, A_i and B_i are the quantities defined in Section 2.4.2

updated for each layer. These equations are used to generate the diffuse reflectance spectra with predetermined values for $\boldsymbol{\theta}$. A white Gaussian noise of a signal-to-noise ratio of 50 is then added to the simulated spectra to mimic the noise that is always present in real measurements, yet keep the strength of the signal high enough to ensure that our results are not skewed by noise.

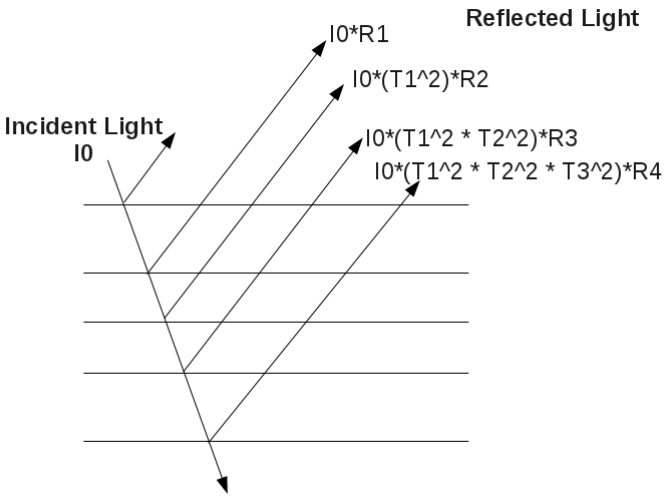

Figure 4.3: Reflected light by each layer of the skin(Dawson et al., 1980)

4.4 The Inversion Algorithm

We aim to recover the volume fractions of melanin and haemoglobin in skin from simulated diffuse reflectance spectra. We use three estimation methods: Least squares, maximum likelihood and maximum *a posteriori* estimation techniques and compare their accuracy and stability. In addition to adding Gaussian noise to our reflectance spectra, we also introduce uncertainty in a single known parameter of the model. We choose the epidermal thickness to be the uncertain parameter as it is the property with the widest range of possible values, and thus the most variability in real life [20 - 150μm] (Yudovsky and Pilon, 2011). This is achieved by modelling the epidermal thickness using a normal distribution with mean $\overline{d}_{\text{epi}} = 0.008$ cm and a standard deviation of $\sigma_d = 8\text{e}^{-4}$ cm. The thicknesses of the remaining layers are set to the values provided in Table 4.1.

The recovery process is performed for various values of volume fractions of melanin and haemoglobin. Consequently, we generate reflectance spectra for discrete values of C_{HB*} and C_{Mel} ranging between 0.5% and 9.5%, and for each value of d_{epi} drawn from the aforementioned distribution. We will, henceforth, refer to simulated reflectance spectra by $\mathbf{x}_0$ and to the noiseless spectra generated by the forward model as part of the inversion process by $R_i(\boldsymbol{\theta})$. The process of generating the simulated spectra for each tuple $(d_{epi}, C_{HB*}, C_{Mel})$ is depicted in Figure 4.4 and this is repeated for discrete wavelengths between 300 and 800 nm at 2 nm intervals. In order to be able to use the Kubelka-Munk method, we assume that the light source is diffuse. We then estimate $\boldsymbol{\theta}$ using the LSQ, ML and MAP techniques.

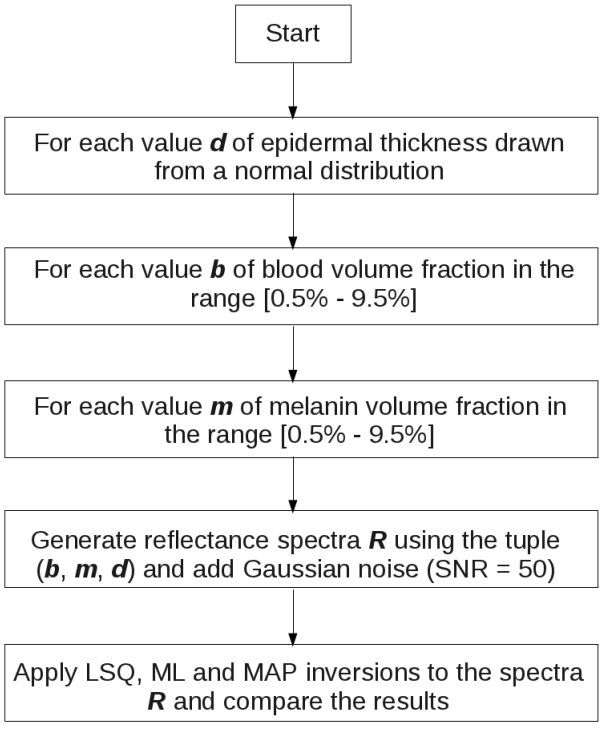

Figure 4.4: Flowchart of the experimental process

Unlike the classical estimators (LSQ and ML), the Bayesian approach requires the use of a prior in order to calculate the posterior probability distribution of the unknown

parameter $\boldsymbol{\theta}$. This is an essential part of the parameter recovery operation as it allows us to include as much information about the tissue as possible. When considering the skin, the literature indicates that both the absorption coefficients and the pigments volume fractions are often retrieved from reflectance data.

However, the volume fractions of pigments cannot always be recovered directly from reflectance spectra in the case of other biological tissues. Consequently, these volume fractions are often assumed to have constant values to aid the recovery of μ_a rather than estimated directly. When these volume fractions are retrieved from the absorption coefficient, other assumptions about the remaining properties of the tissue are introduced. Consequently, obtaining usable and reasonable prior information becomes very difficult, and more importantly, prone to errors.

As a result, we propose not to rely on the available literature to determine the prior distribution of haemoglobin and melanin volume fractions in the skin. Rather, we generate the prior data in two different ways and compare the results of the estimation process when using each set of prior information. This will allow us to verify the effect of changing the prior distribution on the result of the estimation process.

The first method uses results from the classical estimation techniques as one set of prior data. When using this method, we have very limited control over the variability of the prior data points. The second set of prior data is generated by assuming a mean $\bar{\boldsymbol{\theta}}$ between $[0.5\%, 0.5\%]$ and $[9.5\%, 9.5\%]$ and standard deviation $\sigma_{\boldsymbol{\theta}} = 30\%$ to represent a normal distribution $\sim N(\bar{\boldsymbol{\theta}}, \sigma^2_{\boldsymbol{\theta}})$. Because the unknown parameters (blood and melanin concentrations in this instance) are independent variables, their joint probability distribution, and thus $p(\boldsymbol{\theta})$ can be calculated by equation (4.8) where $p(\theta_i)$ is the prior probability distribution of parameter θ_i calculated using σ^2 and μ the variance and mean of the prior data collected from previous experiments.

$$p(\boldsymbol{\theta}) = \prod_{i=1}^{m} p(\theta_i) \quad \text{with} \quad p(\theta_i) = \frac{1}{\sqrt{2\pi\sigma^2}} \exp\left[-\frac{(\theta_i - \mu)^2}{2\sigma^2}\right] \tag{4.8}$$

Let $p(\theta_i)$ represent the probability distribution of the i^{th} component of $\boldsymbol{\theta}$ (in this case either $\mathrm{C}_{\mathrm{HB}*}$ or $\mathrm{C}_{\mathrm{Mel}}$). As the prior knowledge in this experiment is essentially the results of previous estimation process, the previous equation can be expanded as:

$$p(\boldsymbol{\theta}) = \frac{\exp\left[-\frac{(\mathrm{C}_{\mathrm{HB}*}-\mu_{\mathrm{HB}*})^2}{2\sigma^2{}_{\mathrm{HB}*}}\right]}{\sqrt{2\pi\sigma_{\mathrm{HB}*}}^2} \cdot \frac{\exp\left[-\frac{(\mathrm{C}_{\mathrm{Mel}}-\mu_{\mathrm{mel}})^2}{2\sigma^2{}_{\mathrm{mel}}}\right]}{\sqrt{2\pi\sigma_{\mathrm{mel}}}^2} \tag{4.9}$$

In addition to the effects of uncertainty on the quality of the estimators, we also investigate the effect that the amount of prior data can have on the parameter recovery process. Consequently, we execute the inversion algorithm with two sets of prior data points of sizes ($size_{\mathrm{p}}$ =)10 and 100. Finally, we suggest some modifications to the maximised function in maximum likelihood and maximum *a posteriori* . This is to reduce the time and complexity of the calculations required in these methods. These modifications are explained in details in the following section.

4.4.1 Maximum Likelihood

As described in Chapter 3, the maximum likelihood method aims to recover the value of $\boldsymbol{\theta}$ that maximises the probability density function (PDF) described by Equation (4.10).

$$p(\mathbf{x};\boldsymbol{\theta}) = \frac{1}{(2\pi\sigma^2)^{\frac{N}{2}}} \exp\left[-\frac{1}{2\sigma^2}\sum_{n=1}^{N}(x_n - \mathrm{R}_i(\boldsymbol{\theta}))^2\right] \tag{4.10}$$

However, maximising the PDF is equivalent to maximising $\ln\left(p(\mathbf{x};\boldsymbol{\theta})\right)$ which can be obtained using equation (4.11)

$$\begin{aligned}\ln\left(p(\mathbf{x};\boldsymbol{\theta})\right) &= \ln\left(\frac{1}{(2\pi\sigma^2)^{\frac{N}{2}}} \exp\left[-\frac{1}{2\sigma^2}\sum_{n=1}^{N}(x_n - \mathrm{R}_n(\boldsymbol{\theta}))^2\right]\right) \\ &= \ln\left(\frac{1}{(2\pi\sigma^2)^{\frac{N}{2}}}\right) - \frac{1}{2\sigma^2}\sum_{n=1}^{N}(x_n - \mathrm{R}_n(\boldsymbol{\theta}))^2\end{aligned} \tag{4.11}$$

Because $\frac{1}{(2\pi\sigma^2)^{\frac{N}{2}}}$ is not dependant on $\boldsymbol{\theta}$, we conclude that maximising the natural logarithm of the probability density function is equivalent to minimising $\frac{1}{2\sigma^2}\sum_{n=1}^{N}(x_n - \mathrm{R}_n(\boldsymbol{\theta}))^2$

Consequently, the optimisation process can be reduced to the following equation:

$$\hat{\boldsymbol{\theta}} = \arg\max_{\boldsymbol{\theta}} \left[\ln\left(p(\mathbf{x};\boldsymbol{\theta})\right)\right] = \arg\min_{\boldsymbol{\theta}} \left[\frac{1}{2\sigma^2}(x_n - \mathrm{R}_n(\boldsymbol{\theta}))^2\right] \tag{4.12}$$

4.4.2 Maximum *A Posteriori*

Similarly, the maximum *a posteriori* estimate can be obtained by maximising the natural logarithm $\arg\max_{\boldsymbol{\theta}} \left(\ln\left(p(\mathbf{x}|\boldsymbol{\theta}) \times p(\boldsymbol{\theta})\right)\right)$, which is equivalent to maximising the sum of logarithms $\ln\left(p(\mathbf{x}|\boldsymbol{\theta})\right) + \ln(p(\boldsymbol{\theta}))$. Expanding $\ln\left(p(\boldsymbol{\theta})\right)$ would result is Equation 4.13 as detailed below:

$$\begin{aligned}
\ln\left(p(\boldsymbol{\theta})\right) &= \ln \prod_{i=1}^{m} p(\theta_i) \\
&= \ln\left(\prod_{i=1}^{m} \frac{1}{\sqrt{2\pi\sigma^2_{\theta_i}}} \exp\left[-\frac{(\theta_i - \mu_{\theta_i})^2}{2\sigma^2_{\theta_i}}\right]\right) \\
&= \sum_{i=1}^{m} \ln\left(\frac{1}{\sqrt{2\pi\sigma^2_{\theta_i}}} \exp\left[-\frac{(\theta_i - \mu_{\theta_i})^2}{2\sigma^2_{\theta_i}}\right]\right) \\
&= m \times \ln\left(\frac{1}{\sqrt{2\pi\sigma^2_{\theta_i}}}\right) - \sum_{i=1}^{m}\left[\frac{(\theta_i - \mu_{\theta_i})^2}{2\sigma^2_{\theta_i}}\right]
\end{aligned} \tag{4.13}$$

Finally, we substitute Equation (4.11) and Equation 4.13 in the formula $\ln\left(p(\mathbf{x}|\boldsymbol{\theta})\right) + \ln(p(\boldsymbol{\theta}))$ and we obtain:

$$\begin{aligned}
&\ln\left(p(\mathbf{x}|\boldsymbol{\theta})\right) + \ln(p(\boldsymbol{\theta})) = \\
&\ln\left(\frac{1}{(2\pi\sigma^2)^{\frac{N}{2}}}\right) - \frac{1}{2\sigma^2}\sum_{n=1}^{N}(x_n - \mathrm{R}_n(\boldsymbol{\theta}))^2 + m \times \ln\left(\frac{1}{\sqrt{2\pi\sigma^2_{\theta_i}}}\right) - \sum_{i=1}^{m}\left[\frac{(\theta_i - \mu_{\theta_i})^2}{2\sigma^2_{\theta_i}}\right] = \\
&\ln\left(\frac{1}{(2\pi\sigma^2)^{\frac{N}{2}}}\right) + m \times \ln\left(\frac{1}{\sqrt{2\pi\sigma^2_{\theta_i}}}\right) - \left[\frac{1}{2\sigma^2}\sum_{n=1}^{N}(x_n - \mathrm{R}_n(\boldsymbol{\theta}))^2 + \sum_{i=1}^{m}\frac{(\theta_i - \mu_{\theta_i})^2}{2\sigma^2_{\theta_i}}\right]
\end{aligned} \tag{4.14}$$

As the term $\left[\ln\left(\frac{1}{(2\pi\sigma^2)^{\frac{N}{2}}}\right)+\sum_{i=1}^{m}\ln\left(\frac{1}{\sqrt{2\pi\sigma_{\theta_i}}^2}\right)\right]$ is not dependant on $\boldsymbol{\theta}$, the maximisation process can safely ignore this term, and consequently, the maximum *a posteriori* estimator can be simplified as

$$MAP_{\boldsymbol{\theta}} = \arg\min_{\boldsymbol{\theta}} \left[\frac{1}{2\sigma^2}\sum_{n=1}^{N}(x_n - \mathrm{R}_n(\boldsymbol{\theta}))^2 + \sum_{i=1}^{m}\frac{(\theta_i-\mu)^2}{2\sigma_{\theta_i}^2}\right] \tag{4.15}$$

Consequently, we use equations (3.5), (4.12) and (4.15) as the objective functions to be minimised in order to estimate the unknown parameter $\boldsymbol{\theta}$ using LSQ, ML and MAP respectively. We use the Global Optimization Toolbox (MathWorks) to complete the minimisation process, which uses the Levenberg-Marquardt algorithm described in Section 3.3.4.

To generate the set of priors based on previous estimation results, we use Algorithm 4.1 which outlines the data and steps required to estimate the parameter $\boldsymbol{\theta}$ using the maximum likelihood and least-squares methods. Note that we also use the true epidermal thickness of the simulated skin samples when generating the reflectance spectra. This is done for 100 values of d_{epi} for each value of $\boldsymbol{\theta}$. For the inversion step, however, we always assume that $d_{epi} = \overline{d}_{epi}$ in order to include uncertainty in our model. Once the estimation using ML and LSQ is completed, we follow the procedure described in Algorithm 4.2 to estimate $\boldsymbol{\theta}$ using the various prior sets generated previously.

Algorithm 4.1 Estimation Process Using ML and LSQ

Data:
$\overline{d}_{epi}$: mean thickness, used as assumed sample thickness during the estimation process
$\sim N(\overline{d}_{epi}, \sigma^2_{d_{epi}})$: distribution of true thicknesses,
$\mathrm{RANGE}_{\mathrm{C}_{\mathrm{HB}*}} = [0.5 : 0.5 : 9.5\%]$: Range of possible values of $\mathrm{C}_{\mathrm{HB}*}$,
$\mathrm{RANGE}_{\mathrm{C}_{\mathrm{Mel}}} = [0.5 : 0.5 : 9.5\%]$: Range of possible values of $\mathrm{C}_{\mathrm{Mel}}$,
$\mathrm{RANGE}_{\lambda} = [300 : 2 : 800]$ nm: Range of wavelengths used,
$runKM(\lambda, d, \theta)$: function to calculate the reflectance spectra at wavelength range λ, thickness d and parameter vector $\boldsymbol{\theta}$,
σ^2: Variance of the measured spectra (or in this case, the variance of $runKM(\lambda, \theta)$ + noise
begin
for all $\mathrm{C}_{\mathrm{HB}*} \in \mathrm{RANGE}_{\mathrm{C}_{\mathrm{HB}*}}$ **do**
  for all $\mathrm{C}_{\mathrm{Mel}} \in \mathrm{RANGE}_{\mathrm{C}_{\mathrm{Mel}}}$ **do**
    $\boldsymbol{\theta} := (\mathrm{C}_{\mathrm{HB}*}, \mathrm{C}_{\mathrm{Mel}})^T$
    for all $d_{epi} \in \sim N(\bar{d}_{epi}, \sigma^2_{d_{epi}})$ **do**
      $\mathrm{R}_{\mathrm{simulated}} := runKM(\mathrm{RANGE}_{\lambda}, d_{epi}, \boldsymbol{\theta}) + \mathrm{noise}$
      $\hat{\boldsymbol{\theta}}_{\mathrm{ML}} = \arg\min_{\boldsymbol{\theta}} \left[\frac{1}{2\sigma^2} \sum_{n=1}^{N} (\mathrm{R}_{\mathrm{simulated}} - runKM(\mathrm{RANGE}_{\lambda}, \boldsymbol{\theta}))^2 \right]$
      $\hat{\boldsymbol{\theta}}_{\mathrm{LSQ}} = \arg\min_{\boldsymbol{\theta}} \left[\sum_{n=1}^{N} (\mathrm{R}_{\mathrm{simulated}} - runKM(\mathrm{RANGE}_{\lambda}, \boldsymbol{\theta}))^2 \right]$
    end for
  end for
end for
end

Algorithm 4.2 Estimation Process using MAP

Data:
$\bar{d}_{epi}$: mean thickness, used as assumed sample thickness during the estimation process
$\sim N(\bar{d}_{epi}, \sigma^2_{d_{epi}})$: distribution of true thicknesses,
$\mu_{\mathrm{C_{HB*}}}$, $\sigma_{\mathrm{C_{HB*}}}$: theoretical mean and standard deviation of prior haemoglobin volume fractions,.
$\mu_{\mathrm{C_{Mel}}}$, $\sigma_{\mathrm{C_{Mel}}}$: theoretical mean and standard deviation of prior melanin volume fractions,
$\mu^{\mathrm{ML}}_{\mathrm{C_{HB*}}}$, $\sigma^{\mathrm{ML}}_{\mathrm{C_{HB*}}}$: mean and standard deviation of haemoglobin volume fractions estimated using ML,
$\mu^{\mathrm{ML}}_{\mathrm{C_{Mel}}}$, $\sigma^{\mathrm{ML}}_{\mathrm{C_{Mel}}}$: mean and standard deviation of melanin volume fractions estimated using ML,
$\mu^{\mathrm{LSQ}}_{\mathrm{C_{HB*}}}$, $\sigma^{\mathrm{LSQ}}_{\mathrm{C_{HB*}}}$: mean and standard deviation of haemoglobin volume fractions estimated using LSQ,
$\mu^{\mathrm{LSQ}}_{\mathrm{C_{Mel}}}$, $\sigma^{\mathrm{LSQ}}_{\mathrm{C_{Mel}}}$: mean and standard deviation of melanin volume fractions estimated using LSQ
$\mathrm{RANGE}_{\mathrm{C_{HB*}}} = [0.5 : 0.5 : 9.5\%]$: Range of possible values of $\mathrm{C_{HB*}}$,
$\mathrm{RANGE}_{\mathrm{C_{Mel}}} = [0.5 : 0.5 : 9.5\%]$: Range of possible values of $\mathrm{C_{Mel}}$,
$\mathrm{RANGE}_{\lambda} = [300 : 2 : 800]$ nm: Range of wavelengths used,
$runKM(\lambda, d, \theta)$: function to calculate the reflectance spectra at wavelength range λ, thickness d and parameter vector $\boldsymbol{\theta}$,
σ^2: Variance of the measured spectra (or in this case, the variance of $runKM(\lambda, \theta) +$ noise
begin
for all $\mathrm{C_{HB*}} \in \mathrm{RANGE}_{\mathrm{C_{HB*}}}$ **do**
  for all $\mathrm{C_{Mel}} \in \mathrm{RANGE}_{\mathrm{C_{Mel}}}$ **do**
    $\boldsymbol{\theta} := (\mathrm{C_{HB*}}, \mathrm{C_{Mel}})^T$
    for all $d_{epi} \in \sim N(\bar{d}_{epi}, \sigma^2_{d_{epi}})$ **do**
      $\mathrm{R_{simulated}} := runKM(\mathrm{RANGE}_{\lambda}, d_{epi}, \boldsymbol{\theta}) + \mathrm{noise}$
      $$\hat{\boldsymbol{\theta}}_{\mathrm{MAP}} := \arg\min_{\boldsymbol{\theta}} \left[\frac{1}{2\sigma^2} \sum_{n=1}^{N} (\mathrm{R_{simulated}} - runKM(\mathrm{RANGE}_{\lambda}, \boldsymbol{\theta}))^2 + \frac{(\theta_1 - \mu_{\mathrm{C_{HB*}}})^2}{2\sigma^2_{\theta_{\mathrm{C_{HB*}}}}} + \frac{(\theta_2 - \mu_{\mathrm{C_{Mel}}})^2}{2\sigma^2_{\theta_{\mathrm{C_{Mel}}}}} \right]$$
      $$\hat{\boldsymbol{\theta}}^{\mathrm{ML}}_{\mathrm{MAP}} := \arg\min_{\boldsymbol{\theta}} \left[\frac{1}{2\sigma^2} \sum_{n=1}^{N} (\mathrm{R_{simulated}} - runKM(\mathrm{RANGE}_{\lambda}, \boldsymbol{\theta}))^2 + \frac{(\theta_1 - \mu^{\mathrm{ML}}_{\mathrm{C_{HB*}}})^2}{\left(\sqrt{2}\sigma^{\mathrm{ML}}_{\mathrm{C_{HB*}}}\right)^2} + \frac{(\theta_2 - \mu^{\mathrm{ML}}_{\mathrm{C_{Mel}}})^2}{\left(\sqrt{2}\sigma^{\mathrm{ML}}_{\mathrm{C_{Mel}}}\right)^2} \right]$$
      $$\hat{\boldsymbol{\theta}}^{\mathrm{LSQ}}_{\mathrm{MAP}} := \arg\min_{\boldsymbol{\theta}} \left[\frac{1}{2\sigma^2} \sum_{n=1}^{N} (\mathrm{R_{simulated}} - runKM(\mathrm{RANGE}_{\lambda}, \boldsymbol{\theta}))^2 + \frac{(\theta_1 - \mu^{\mathrm{LSQ}}_{\mathrm{C_{HB*}}})^2}{\left(\sqrt{2}\sigma^{\mathrm{LSQ}}_{\mathrm{C_{HB*}}}\right)^2} + \frac{(\theta_2 - \mu^{\mathrm{LSQ}}_{\mathrm{C_{Mel}}})^2}{\left(\sqrt{2}\sigma^{\mathrm{LSQ}}_{\mathrm{C_{Mel}}}\right)^2} \right]$$
    end for
  end for
end for
end

4.5 Results and Discussion

Using Algorithm 4.1 and Algorithm 4.2, we estimate the unknown parameter $\boldsymbol{\theta}$ using LSQ, ML and MAP estimation techniques. At the completion of the experiment, we note that both the maximum likelihood and the least-squares estimators produce relatively good results with the mean values of estimates being close to the expected values of $\boldsymbol{\theta}$. Figure 4.5 summarises the results of estimating $\boldsymbol{\theta}$ when $C_{HB*} = 8.0\%$ and C_{Mel} varies between 2% and 8%; and when $C_{Mel} = 2\%$ and C_{HB*} varies between 2 and 8%. We also observe that the standard deviation of estimates of C_{HB*} varies between 1.20% and 25.7% for LSQ; and 0.39% and 25.7% for ML. The results are similar for C_{Mel} where the standard deviation of the estimates varies between 0.28% and 18.2% when using LSQ; and 0.23% and 22.1% when using ML.

In contrast, we note that the distribution of MAP estimates is much narrower than that of ML and LSQ estimates. In fact, the standard deviations have a maximum value of 0.002% for C_{HB*} estimates even when only 10 prior data points are used, as shown on Figure 4.6 and Figure 4.7. Moreover, we observe that the mean estimates produced by MAP are often closer to the expected value of $\boldsymbol{\theta}$ than ML and LSQ results. However, the results are slightly different when considering estimates of C_{Mel}. Although the mean MAP estimates of C_{Mel} are more accurate than those produced by ML and LSQ, they are less so than C_{HB*} estimates. Furthermore, the distributions of the results are slightly wider for C_{Mel} with a maximum value of 0.09%.

As shown in Algorithm 4.2, we also run the MAP estimator with an independent set of prior data that was not generated from the results of other estimators. This allows us to easily control the mean and variance of the data points used and therefore investigate the effect of this variations on the estimator. This is depicted in Algorithm 4.2: Lines 4, 5, 21, 22. We note that the results are very similar to those obtained by using previous estimates as priors. We then increase the variance of the prior data to a value higher than seen in the previously used prior datasets by setting $30\% \leq \sigma_{\boldsymbol{\theta}} \leq 60\%$.

We observe that the results are still as close to the expected values as those obtained from estimates based prior data sets. However, the error level was higher than previously observed for MAP estimates, but still much smaller than noted in ML and LSQ estimations results. Table 4.2 summarises the error levels of MAP estimates when the standard deviation of the prior data is increased. Note that when the prior data distribution is wide (40%), the error level of the MAP estimates is significantly higher than that recorded for smaller prior distributions (5 and 15%). This strongly suggests that the width of the prior distribution can have a significant impact on the result of the MAP estimation process.

Prior Standard Deviation	Haemoglobin			Melanin		
	$\text{MIN}_{\text{error}}$ (%)	$\text{MEAN}_{\text{error}}$ (%)	$\text{MAX}_{\text{error}}$ (%)	$\text{MIN}_{\text{error}}$ (%)	$\text{MEAN}_{\text{error}}$ (%)	$\text{MAX}_{\text{error}}$ (%)
5%	3.44	3.84	4.23	3.29	3.87	5.43
15%	5.79	9.60	13.44	6.64	9.38	12.84
40%	7.17	22.47	99.57	11.17	30.12	97.82

Table 4.2: Error levels recorded for varying values of standard deviations of prior data. Note that the error level increases with larger variability in prior data. This suggests that a wider prior can lead to a decrease in the accuracy of the MAP estimation method.

In addition to evaluating the MAP estimator against the ML and LSQ methods, we examine the effects of varying the prior data on our estimator's accuracy. To that aim, the experimental process described in Algorithm 4.2 is repeated for two prior data sizes: 10 and 100. The prior data is generated as described in Section 4.4.2. Figure 4.6 and Figure 4.9 depict the results of the estimation process when the size of the prior data is 10 and 100 respectively.

When using only 10 prior data points, we can see, in Table 4.4 and Table 4.5, that the mean estimates produced by MAP are still closer to the expected value of $\boldsymbol{\theta}$ than ML and LSQ. The distribution of the results is also much narrower than that of LSQ and

ML as depicted by Figure 4.6. After increasing the prior data size to 100 data points, we note that the standard deviations of MAP estimates show a slight increase to 0.003% as a maximum value for $\sigma(C_{HB*})$ but remain much lower than the non-Bayesian estimates. The same remains true for C_{Mel} MAP estimates where the standard deviation is slightly higher with a maximum value of 0.15% as depicted in Table 4.3. Figure 4.8 and Figure 4.9 show a sample of the results of estimating $\boldsymbol{\theta}$ with a prior data set of size 100.

$Size_p$	θ_i	LSQ	ML	MAP
10	C_{HB*}	$[2.33 - 14.1\%]$	$[2.30 - 14.8\%]$	$[0 - 0.005\%]$
	C_{Mel}	$[2.49 - 21.7\%]$	$[2.52 - 25.9\%]$	$[0 - 0.14\%]$
100	C_{HB*}	$[2.33 - 14.1\%]$	$[2.30 - 14.8\%]$	$[0 - 0.007\%]$
	C_{Mel}	$[2.49 - 21.7\%]$	$[2.52 - 25.9\%]$	$[0 - 0.15\%]$

Table 4.3: Standard Deviations of Estimation Results

Furthermore, we note that for both C_{HB*} and C_{Mel}, the mean estimates provided by 10 priors were more accurate than those produced using 100 prior data points. When investigating this further, we observed that the standard deviation of the 10 data points sample was smaller than that of the full 100 points sample. This confirms that the quantity of prior data is not the main factor affecting the quality of the Bayesian estimation. Rather, the distribution of the prior data has a much more important effect on the quality of the Bayesian estimator.

4.6 Conclusion

In this chapter, we showed how a technique based on a combination of the maximum *a posteriori* method and a Kubelka-Munk based forward model can be used to recover the parameters of a tissue from reflectance spectra. The reflectance spectra was simulated for various values of $\boldsymbol{\theta}$ and d_{epi}. $\boldsymbol{\theta}$ was estimated using three different methods, namely: least-squares, maximum likelihood and maximum *a posteriori*. The results of the estimations were compared and we observed that the MAP estimates were often more accurate than their ML and LSQ counterparts. We also observed that the MAP results were more stable than those generated by ML and LSQ as demonstrated by the very small standard deviation ($\leq 0.15\%$).

We also investigated the effects of prior data on the results of our estimator. This was achieved by varying both the number of data points and their standard deviation. We concluded that the number of data points in the prior does not affect the results of the estimation process. We also showed that varying the standard deviation of the prior data can have an effect on the accuracy of the MAP estimator. This was demonstrated by a slight increase in the results' standard deviation when the variance of the prior data is increased. We therefore suggest that the presence of uncertainty in both the known (d_{epi}) and unknown (C_{HB*} and C_{Mel}) parameters does not dramatically decrease the accuracy of MAP in comparison with ML and LSQ.

Our findings suggest that this method is promising and can be used to accurately recover the parameters of a biological tissue whose properties are well defined. However, the effects of increasing the level of uncertainty in the model on our estimator need to be investigated further. Following the encouraging results that we observed with simulated reflectance data, we apply our estimation method to actual spectral measurements as described in the following chapters.

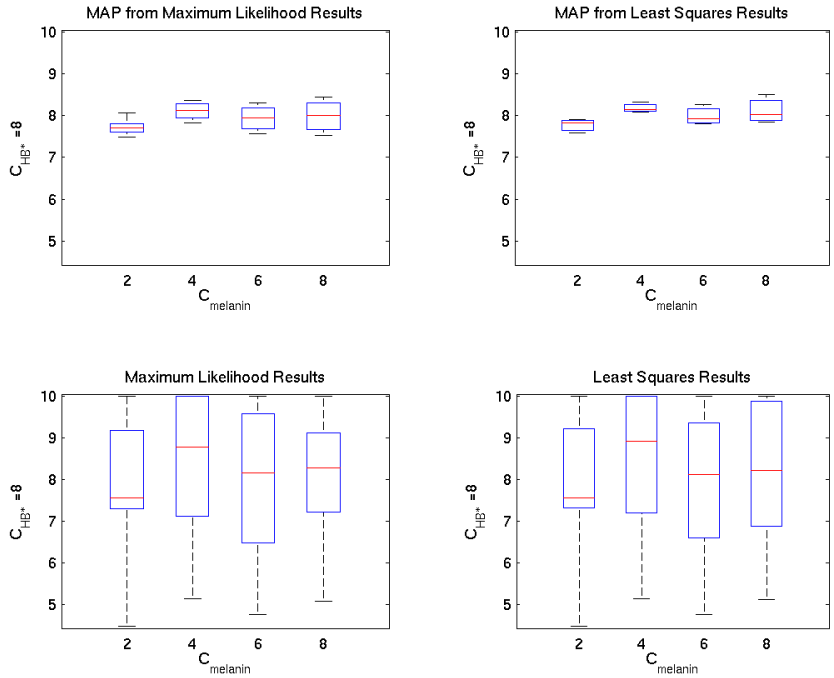

(a) $C_{HB*} = 8.0$

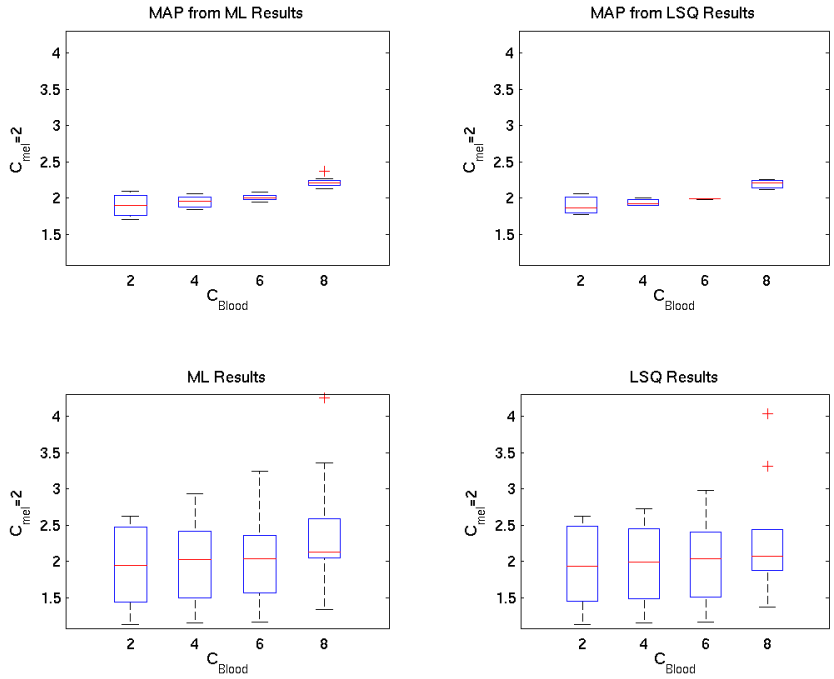

(b) $C_{Mel} = 2.0$

Figure 4.5: These plots represent the results of recovering $\boldsymbol{\theta}$ using LSQ, ML, and the MAP based estimator. The plots entitled MAP from ML and MAP from LSQ illustrate the MAP estimates obtained using prior data sets from ML and LSQ estimates respectively. The results are displayed with one parameter fixed (C_{HB*} in 4.5a and C_{Mel} in 4.5b) while varying the other in order to show the estimates produced for different values of θ. Each box outlines the estimates $\hat{\boldsymbol{\theta}}$ for a 100 values of d_{epi} (drawn from a normal distribution with a standard deviation of 20%) and a single combination (C_{HB*}, C_{Mel}) using five attributes. The top and bottom of each box represent the 75^{th} and 25^{th} percentile while the band near the middle of the box denoted the median estimate. The whiskers denote the minimum and maximum of all estimates.

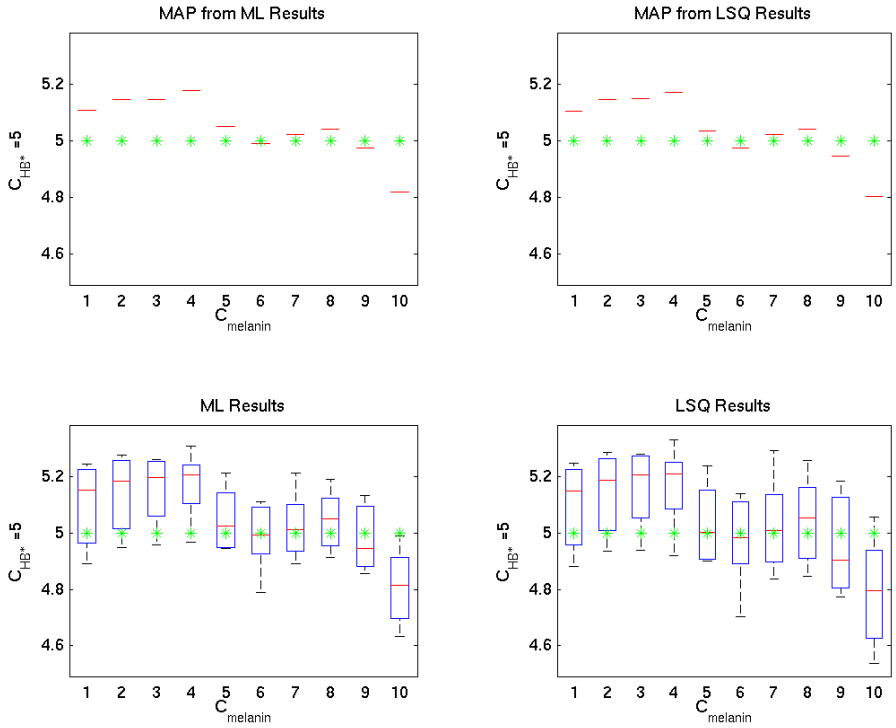

Figure 4.6: Estimation result when $C_{HB*} = 5.0\%$ and C_{Mel} is varied between 1 and 10. The estimation process is run with a prior data size of 10. The plots represent (from bottom-left to upper-right): Estimation results from ML, LSQ, MAP with prior data from ML and LSQ estimates respectively. Each box outlines the estimates $\hat{\boldsymbol{\theta}}$ for a 100 values of d_{epi} (drawn from a normal distribution with a standard deviation of 20%) and a single combination (C_{HB*}, C_{Mel}) using five attributes. The top and bottom of each box represent the 75^{th} and 25^{th} percentile while the band near the middle of the box denoted the median estimate. The whiskers denote the minimum and maximum of all estimates. Note that the box plots for MAP results appear as a single red line due to the results' standard deviation being very close to 0.

C_{HB*}	LSQ			ML			MAP_{LSQ}			MAP_{ML}		
	MEAN	$STD(\%)$		MEAN	$STD(\%)$		MEAN	$STD(\%)$		MEAN	$STD(\%)$	
		MIN	MAX		MIN	MAX		MIN	MAX		MIN	MAX
0.5	0.51	1.66e+00	1.91e+01	0.51	9.69e-01	2.00e+01	0.50	0.00e+00	0.00e+00	0.50	0.00e+00	0.00e+00
1.0	1.01	1.80e+00	1.16e+01	1.01	1.30e+00	1.19e+01	1.00	0.00e+00	0.00e+00	1.01	0.00e+00	0.00e+00
1.5	1.51	2.01e+00	9.03e+00	1.51	1.51e+00	9.03e+00	1.51	0.00e+00	0.00e+00	1.51	0.00e+00	0.00e+00
2.0	2.02	2.11e+00	7.83e+00	2.02	1.61e+00	7.60e+00	2.01	0.00e+00	0.00e+00	2.01	0.00e+00	0.00e+00
2.5	2.52	2.23e+00	7.18e+00	2.52	1.74e+00	6.76e+00	2.51	0.00e+00	0.00e+00	2.51	0.00e+00	0.00e+00
3.0	3.02	2.34e+00	6.81e+00	3.02	1.84e+00	6.23e+00	3.01	0.00e+00	0.00e+00	3.01	0.00e+00	0.00e+00
3.5	3.53	2.45e+00	6.60e+00	3.52	1.93e+00	5.88e+00	3.51	0.00e+00	0.00e+00	3.52	0.00e+00	0.00e+00
4.0	4.03	2.53e+00	6.49e+00	4.03	1.99e+00	5.65e+00	4.01	0.00e+00	2.49e-03	4.02	0.00e+00	0.00e+00
4.5	4.54	2.60e+00	6.44e+00	4.53	2.03e+00	5.49e+00	4.52	0.00e+00	2.21e-03	4.52	0.00e+00	0.00e+00
5.0	5.04	2.65e+00	6.41e+00	5.03	2.06e+00	5.42e+00	5.02	0.00e+00	1.99e-03	5.02	0.00e+00	1.99e-03
5.5	5.54	2.67e+00	6.40e+00	5.54	2.06e+00	5.34e+00	5.52	0.00e+00	1.81e-03	5.52	0.00e+00	1.81e-03
6.0	6.05	2.67e+00	6.40e+00	6.04	2.02e+00	5.29e+00	6.02	0.00e+00	1.66e-03	6.03	0.00e+00	1.66e-03
6.5	6.55	2.64e+00	6.39e+00	6.54	1.98e+00	5.24e+00	6.52	0.00e+00	1.53e-03	6.53	0.00e+00	1.53e-03
7.0	7.05	2.59e+00	6.37e+00	7.04	1.91e+00	5.21e+00	7.02	0.00e+00	1.42e-03	7.03	0.00e+00	1.42e-03
7.5	7.55	2.51e+00	6.35e+00	7.55	1.82e+00	5.17e+00	7.52	0.00e+00	1.33e-03	7.53	0.00e+00	1.33e-03
8.0	8.05	2.41e+00	6.31e+00	8.05	1.71e+00	5.14e+00	8.02	0.00e+00	1.25e-03	8.04	0.00e+00	1.24e-03
8.5	8.55	2.28e+00	6.24e+00	8.55	1.58e+00	5.11e+00	8.52	0.00e+00	1.17e-03	8.54	0.00e+00	1.17e-03
9.0	9.04	2.14e+00	5.17e+00	9.05	1.42e+00	4.27e+00	9.02	0.00e+00	1.11e-03	9.04	0.00e+00	1.11e-03
9.5	9.52	1.84e+00	4.85e+00	9.53	1.27e+00	3.36e+00	9.52	0.00e+00	1.05e-03	9.53	0.00e+00	1.05e-03

Table 4.4: The results of estimating $\boldsymbol{\theta}$ following the process described in Algorithm 4.2. The table shows $\text{C}_{\text{HB}*}$ estimates using LSQ, ML and MAP. The estimation process used a prior data set of size 10.

C_{MEL}	LSQ			ML			MAP_{LSQ}			MAP_{ML}		
	MEAN	$STD(\%)$		MEAN	$STD(\%)$		MEAN	$STD(\%)$		MEAN	$STD(\%)$	
		MIN	MAX		MIN	MAX		MIN	MAX		MIN	MAX
0.5	0.48	7.06e-01	1.73e+01	0.48	4.55e-01	2.11e+01	0.49	0.00e+00	0.00e+00	0.49	0.00e+00	0.00e+00
1.0	0.97	3.18e-01	8.13e+00	0.98	3.58e-01	8.21e+00	0.98	0.00e+00	1.02e-02	0.99	0.00e+00	1.02e-02
1.5	1.48	1.89e-01	8.07e+00	1.49	1.82e-01	8.07e+00	1.49	0.00e+00	1.34e-02	1.49	0.00e+00	1.34e-02
2.0	1.97	1.79e+00	8.06e+00	1.97	2.84e-01	8.00e+00	1.98	0.00e+00	2.02e-02	1.98	0.00e+00	2.02e-02
2.5	2.52	3.21e+00	8.04e+00	2.52	1.46e+00	7.96e+00	2.51	0.00e+00	3.18e-02	2.51	0.00e+00	2.78e-02
3.0	3.04	4.40e+00	8.00e+00	3.03	2.68e+00	7.86e+00	3.03	3.30e-03	3.63e-02	3.03	3.30e-03	3.63e-02
3.5	3.53	5.00e+00	8.18e+00	3.53	3.34e+00	8.03e+00	3.53	5.66e-03	4.53e-02	3.53	2.83e-03	4.25e-02
4.0	4.03	5.67e+00	8.15e+00	4.04	4.04e+00	7.96e+00	4.02	7.45e-03	4.97e-02	4.03	4.96e-03	4.71e-02
4.5	4.55	6.20e+00	8.16e+00	4.56	4.65e+00	7.95e+00	4.53	1.10e-02	5.52e-02	4.54	8.81e-03	5.29e-02
5.0	5.11	6.71e+00	8.13e+00	5.12	5.24e+00	7.88e+00	5.09	1.57e-02	5.90e-02	5.10	9.81e-03	5.49e-02
5.5	5.63	6.98e+00	8.23e+00	5.65	5.58e+00	7.97e+00	5.62	1.78e-02	6.41e-02	5.63	1.42e-02	6.04e-02
6.0	6.09	7.29e+00	8.31e+00	6.12	5.94e+00	8.02e+00	6.10	2.13e-02	6.89e-02	6.12	1.63e-02	6.37e-02
6.5	6.53	7.24e+00	8.44e+00	6.55	6.12e+00	8.15e+00	6.54	2.45e-02	7.34e-02	6.56	1.98e-02	6.86e-02
7.0	6.95	7.53e+00	8.52e+00	6.96	6.39e+00	8.20e+00	6.95	2.88e-02	7.62e-02	6.96	2.30e-02	7.04e-02
7.5	7.47	7.92e+00	8.56e+00	7.48	6.73e+00	8.24e+00	7.45	3.22e-02	7.92e-02	7.46	2.55e-02	7.37e-02
8.0	8.01	8.04e+00	8.62e+00	8.02	6.96e+00	8.33e+00	8.00	3.50e-02	8.38e-02	8.01	2.87e-02	7.74e-02
8.5	8.51	8.32e+00	8.59e+00	8.54	7.28e+00	8.32e+00	8.50	3.88e-02	8.47e-02	8.53	3.17e-02	7.97e-02
9.0	9.01	8.39e+00	8.62e+00	9.05	7.40e+00	8.35e+00	9.01	4.22e-02	8.76e-02	9.05	3.53e-02	8.17e-02
9.5	9.35	6.90e+00	7.10e+00	9.40	6.23e+00	6.76e+00	9.36	2.99e-02	5.88e-02	9.39	2.56e-02	5.43e-02

Table 4.5: The results of estimating $\boldsymbol{\theta}$ following the process described in Algorithm 4.2. The table shows C_{Mel} estimates using LSQ, ML and MAP. The estimation process used a prior data set of size 10.

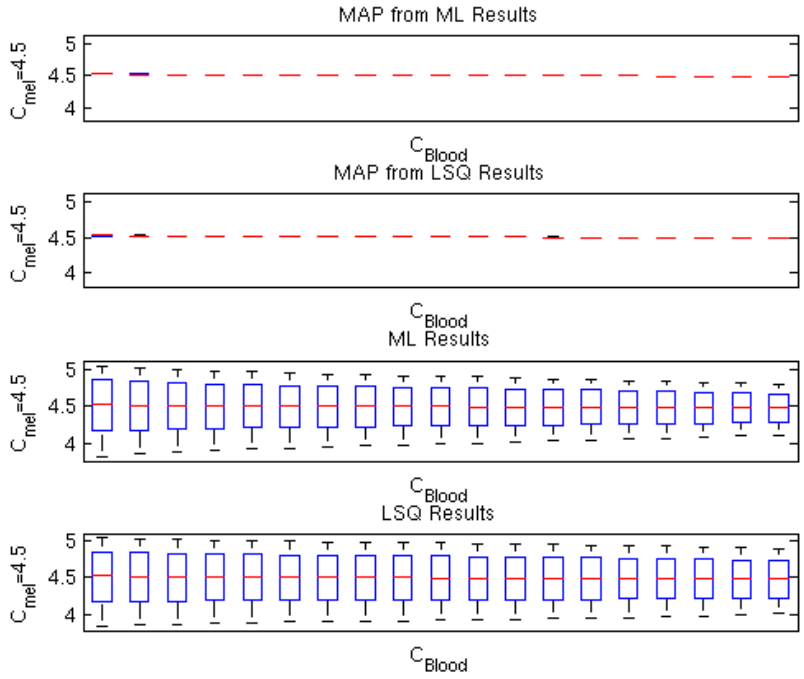

Figure 4.7: Estimation result when $C_{Mel} = 4.5\%$ and C_{HB*} is varied between 0.5 and 9.5. The estimation process is run with a prior data size of 10. The plots represent (from bottom to top) estimation results from LSQ, ML, MAP with prior data from LSQ and ML estimates respectively.

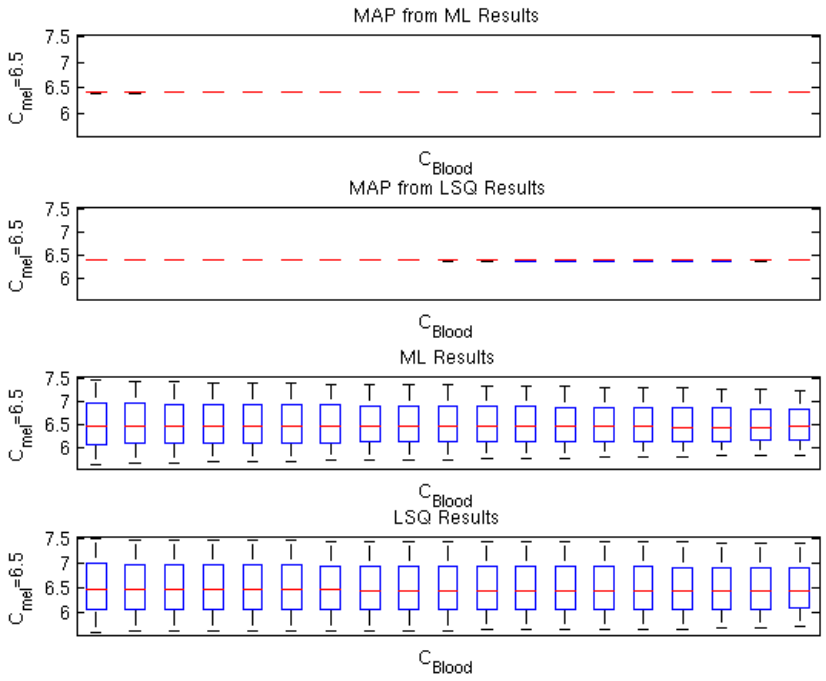

Figure 4.8: Estimation result when $C_{Mel} = 6.5\%$ and C_{HB*} is varied between 0.5 and 9.5. The estimation process is run with a prior data size of 100.

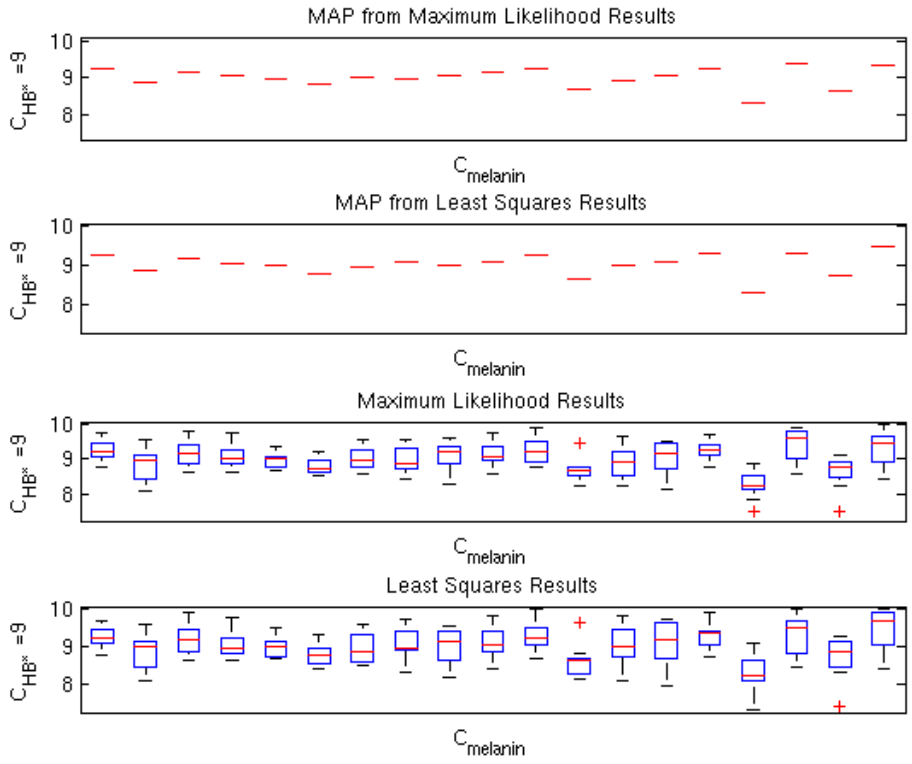

(a) $C_{HB*} = 9\%$

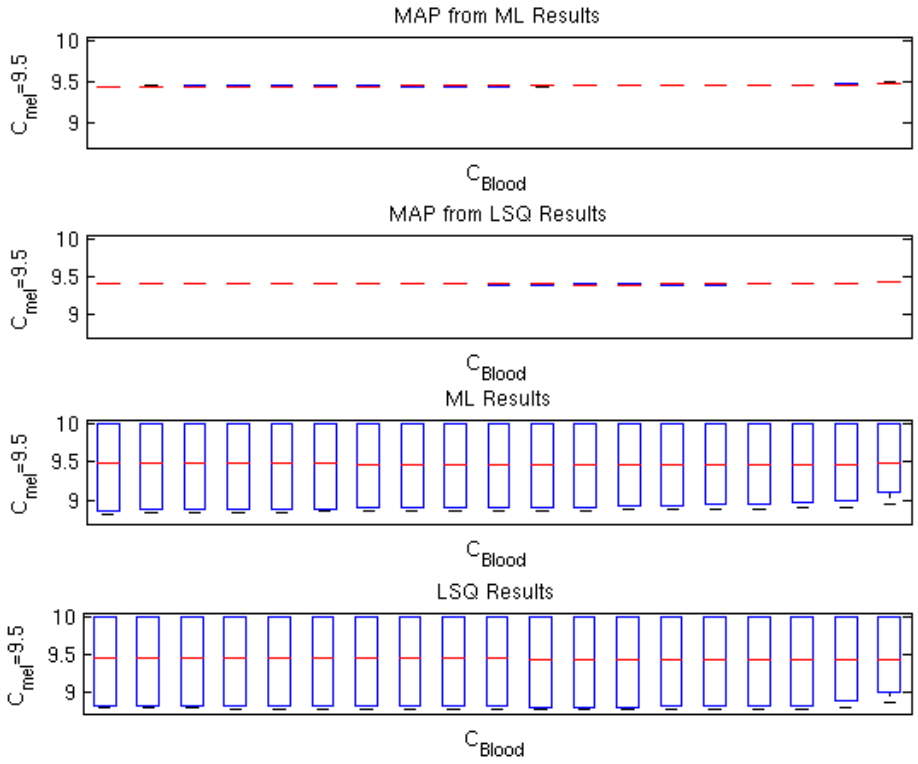

(b) $C_{Mel} = 9.5\%$

Figure 4.9: Estimation results when $C_{HB*} = 9\%$ (4.9a) and $C_{Mel} = 9.5\%$ (4.9b). The estimation process is run with a prior data size of 100. Note that even when the estimation results of ML and LSQ vary widely as shown in 4.9b, the variance of MAP estimates remains very small as demonstrated by their appearance as a flat red line or a very thin box in Figure 4.9b

Chapter 5

Application to Gelatin Phantoms

5.1 Introduction

In Chapter 4, we demonstrated that our inversion algorithm succeeded in retrieving the pigments volume fractions from simulated skin data. The next step would be to investigate the performance of our estimator when applied to data acquired from a biological tissue. However, we are not able to completely control the level of uncertainty in the forward model representing said tissue. We therefore use an intermediate step where apply the same inversion method in a controlled experimental setting. This allows us to develop a forward model whose level of complexity and introduced uncertainty can be controlled.

To that aim, we apply the inversion method described in Chapter 4 to gelatin phantoms of known properties. This allows us to control the quantity of absorbing and scattering agents in the phantoms, as well as the uncertainty level present in the forward model. This chapter describes how the phantoms were constructed, as well as the results of our estimation technique on actual measurements taken on scattering and non scattering gelatin phantoms.

5.2 Non-Scattering Phantoms

We prepare phantoms with different quantities of absorbing agents to mimic a single layer turbid medium. We use a gel of known composition as a base and commercially available blue (SKU: 130010427), red (currently unavailable) and natural red (SKU: 130010443)

food colourants (Dr. Oetker, Bielefeld, Germany) as the main absorbing agents. Note that the two red dyes were never combined in any of the phantoms we prepared. We take the phantoms to be described by a finite set of parameters, namely: the thickness of the sample d, the concentration of gelatin $\mathrm{C_{gel}}$, the concentrations of food dyes $\mathrm{C_b}$, $\mathrm{C_{red}}$ and the extinction coefficients $\varepsilon^{\mathrm{red}}$, $\varepsilon^{\mathrm{blue}}$, $\varepsilon^{\mathrm{gel}}$ of the red and blue colourants; and gelatin respectively.

As there are no scatterers present in the phantoms, we assume that the only reflected light is the result of specular reflection caused by the difference in refractive indices between the gel and the petri dish/air. As such, we use the transmitted signal as our measured data. Let $\mathrm{T}(\lambda_i, \boldsymbol{\theta})$ be the transmittance calculated with tissue parameters $\boldsymbol{\theta}$ at wavelength λ_i. We use the Beer-Lambert law to model light transport in our samples. Let $\mathrm{T}(\lambda, \boldsymbol{\theta}) = e^{-\mathrm{abs}(\lambda,\boldsymbol{\theta})*d}$ where $\mathrm{abs}(\lambda, \boldsymbol{\theta}) = \mu_a^{\mathrm{gel}}(\lambda) + \sum_{i=1}^{n} \theta_i \varepsilon_i(\lambda)$, and θ_i and $\varepsilon_i(\lambda)$ are the concentration and extinction coefficient of the i^{th} dye.

As part of the estimation process, we define the unknown parameter $\boldsymbol{\theta} = (\mathrm{C_{HB*}}, \mathrm{C_{Mel}})^{\mathrm{T}}$ to be the vector representing the chromophore concentrations in the samples. All other parameters are assumed known and are provided to the estimator as predefined input arguments. The known parameters are therefore: the thickness of the sample d, the concentration of gelatin $\mathrm{C_{gel}}$, and the extinction coefficients $\varepsilon^{\mathrm{red}}$, $\varepsilon^{\mathrm{blue}}$, $\varepsilon^{\mathrm{gel}}$ of the red and blue colourants; and gelatin respectively.

In order to acquire the transmittance spectra, light from a high intensity halogen light source (ThorLabs, OSL1-EC) is passed through a long-pass coloured glass filter (ThorLabs, FGL435). This blocks light of wavelengths lower than 435 nm, thus suppressing the known fluorescence of the dyes. The light is then directed towards the sample platform by a highly reflective mirror (ThorLabs, CM1-P01). All light transmitted by the phantom is then collected by a CCD spectrometer and the spectra is recorded for wavelengths between 450 and 700 nm. This setup is described in Figure 5.1.

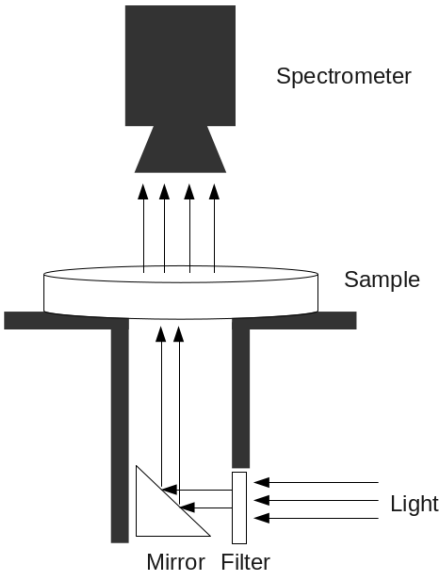

Figure 5.1: Transmittance Spectra Acquisition Setup

The extinction coefficients ε^{red}, $\varepsilon^{\text{nat}-\text{red}}$, $\varepsilon^{\text{blue}}$, ε^{gel} of the colourants and gelatin were extracted from absorbance spectra of various solutions containing water and a single dye. The absorbance spectra was measured using a computer driven Cary 50 UV-VIS spectrophotometer and are shown in Figure 5.2a and Figure 5.2b. As the liquid samples only contain water and dye, we take the absorbance of the solutions to be $\mu_a^{\text{solution}} = \mu_a^{\text{H2O}} + \mu_a^{\text{dye}}$. The absorption coefficients of the dyes are thus calculated as $\mu_a^{\text{dye}} = \left(\mu_a^{\text{solution}} - \mu_a^{\text{H2O}}\right)$. We then apply regression analysis to the absorption coefficients in order to extract the extinction coefficients of the dyes. We prepared various solutions containing different volume fractions of dyes, and thus obtained a number of possible extinction coefficients due to noise in the measurements. We thus apply regression to get the extinction coefficients shown in Figure 5.3 which depicts the extinction coefficients of gelatin and food dyes used in the phantoms.

Figure 5.4 represents the gelatin phantoms' transmittance spectra. As illustrated by Tables 5.1 and 5.2, the transmittance was measured for different thicknesses and concentrations of dyes. The concentration of gelatin, however, remained relatively constant ($\approx 28.5 \pm 0.19$ g/L (0.68 %))

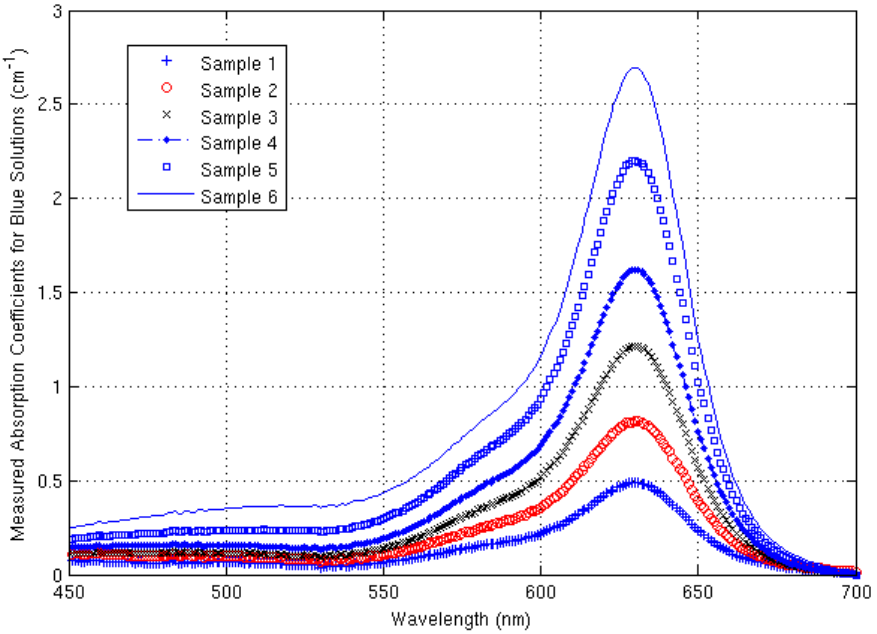

(a) Blue Samples

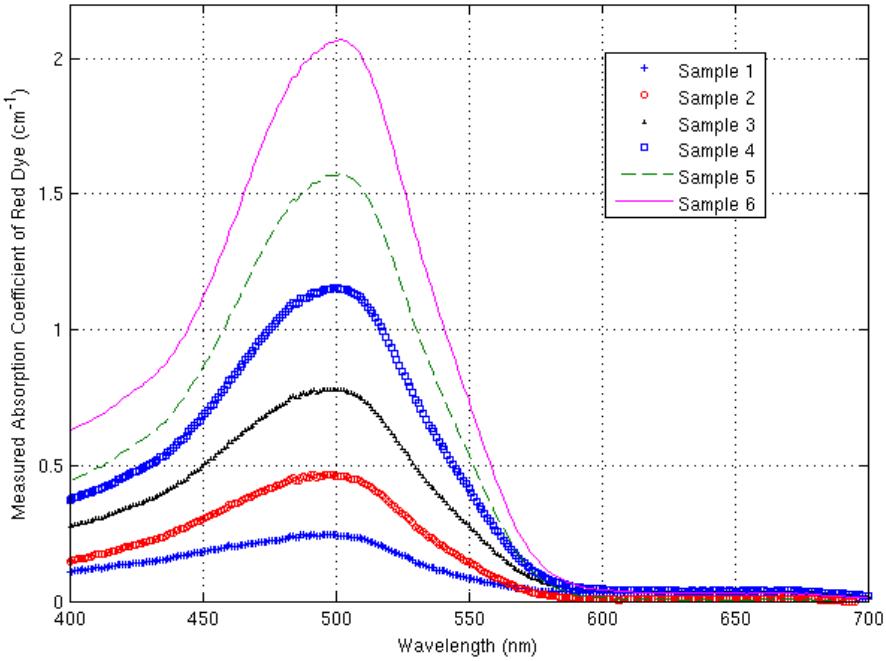

(b) Red Samples

Figure 5.2: The plots show the absorption coefficients of the blue 5.2a and red 5.2b dye solutions as recorded using the Cary 50 UV-VIS spectrophotometer. A number of solutions were prepared with varying volume fractions of dyes. The absorption coefficients were later used to calculate the extinction coefficients of the dyes.

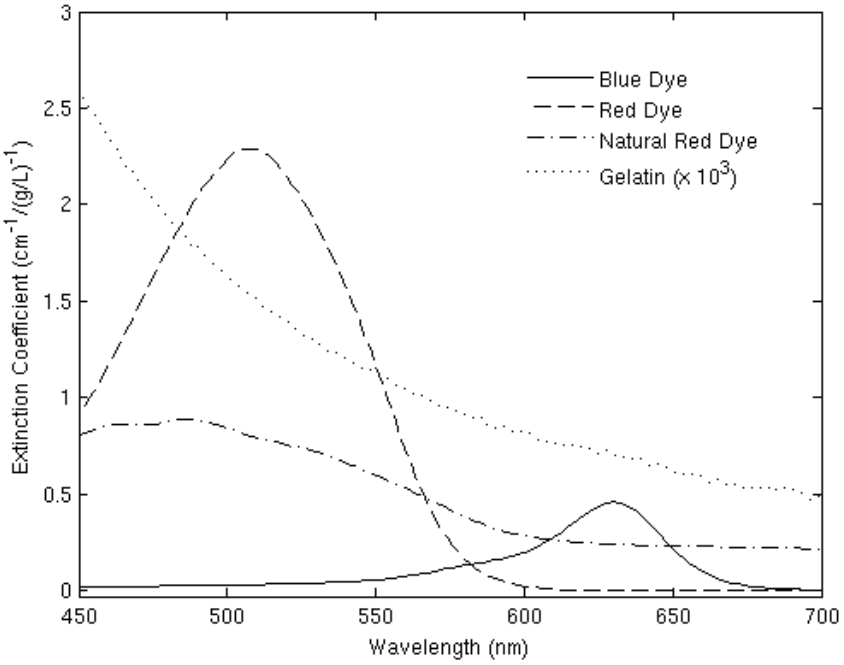

Figure 5.3: Extinction Coefficients of Gel Base and Food Dyes as calculated by the regression analysis performed on absorbance spectra

We prepare 30 gelatin phantoms containing different quantities of dyes, and of different thicknesses. The phantoms are classified by the number of dyes mixed in with the base solution into three categories: samples with blue dye only, samples with red dye only and samples with both blue and red food colourants. Tables 5.1, 5.2 and 5.3 describe the specifications of all samples used in our experiments. Note that the samples NR9, NR10 and NR11 from Table 5.2 contain natural red dye while the other samples described in Table 5.2 include red dye instead.

We assume that the thickness d and concentration of gelatin in the base solution C_{gel} are uncertain. This uncertainty is introduced artificially in the parameter d by sampling the thicknesses of the phantoms from a normal distribution with mean 4.58 mm and standard deviation 1.07 mm (23.33%) as these were the mean and standard deviation of our samples set. Uncertainty is also present in our measurements of the extinction coefficients ε_{blue}, ε_{red} and ε_{gel} as these values were approximated from multiple measurements using regression analysis. This is demonstrated by a standard deviation in the calculated ex-

tinction coefficients ranging between 5.86 and 90.83% for blue dye, and 0.73 and 91.9% for red dye. We use the following values for our uncertain parameters: $\mu_d = 4.58$ mm, $C_{gel} =$ 30 g/L as these are the actual mean thickness and gelatin concentration of our gelatin phantoms.

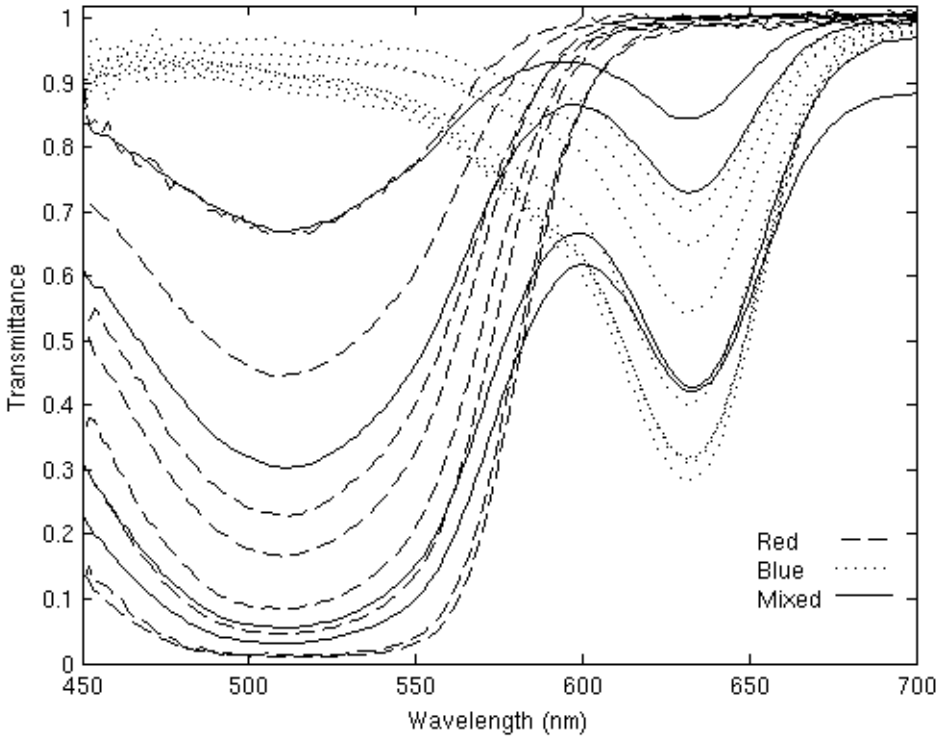

Figure 5.4: Transmittance spectra collected from the gelatin phantoms we prepared. The data is normalised to the signal transmitted through an empty petri dish. As illustrated by Table 5.1, Table 5.2 and Table 5.3, the transmittance was measured for different thicknesses and concentrations of dyes. The concentration of gelatin, however, remained relatively constant ($\approx 28.5 \pm 0.19$ g/L (0.68%))

In addition, we define the prior dataset as a normally distributed random variable with mean $\boldsymbol{\theta}_p$ and a standard deviation $\sigma_{p\{\boldsymbol{\theta_p}\}}$ with $\boldsymbol{\theta}_p$ being the vector representing the mean concentrations of colourants in samples within a chosen sample subset and $\sigma_{p\{\boldsymbol{\theta_p}\}}$ the standard deviation within the same subset. For instance, we take $\boldsymbol{\theta}_p = 2.5227$ g/L and $\sigma_{p\{\boldsymbol{\theta_p}\}} = 1.3365$ g/L (53%) if we aim to estimate the concentration of dye in all samples with blue dye only. The variance of the noise signal is evaluated using the signal to noise

Sample	d (mm)	C_{gel}(g/L)	C_b(g/L)
B1	3.941	28.59	0.8119
B2	3.928	28.59	2.3417
B3	3.909	28.59	3.1623
B4	3.835	28.59	3.1623
B5	4.925	28.40	0.7913
B6	3.576	28.40	1.7952
B7	4.441	28.40	2.6468
B8	2.878	28.40	4.7665
B9	4.441	28.40	2.6468
B10	2.878	28.40	4.7665
B11	3.494	28.63	1.5569
B12	4.724	28.63	1.5569
B13	3.433	28.63	1.5569
B14	3.494	28.63	4.1923
B15	4.724	28.63	4.1923
B16	3.433	28.63	4.1923

Table 5.1: Parameters describing gelatin phantoms that only contain a gel base and blue dye.

Sample	d(mm)	C_{gel}(g/L)	C_{red}(g/L)
R1	3.273	28.59	0.2626
R2	3.435	28.59	0.9490
R3	4.272	28.59	1.4104
R4	4.802	28.59	2.6433
R5	4.574	28.40	0.4043
R6	4.801	28.40	0.9341
R7	4.881	28.40	1.5620
R8	5.010	28.40	2.7908
NR9	4.753	28.63	0.5493
NR10	6.277	28.63	0.5493
NR11	3.702	28.63	0.5493

Table 5.2: Parameters describing gelatin phantoms that only contain a gel base and red dye.

Sample	d (mm)	C_{gel}(g/L)	C_b(g/L)	C_{red}(g/L)
M1	3.906	28.40	0.5478	0.1643
M2	4.695	28.40	0.8023	0.5464
M3	5.786	28.40	2.2240	1.2555

Table 5.3: Parameters describing gelatin phantoms that contain a gel base and a mixture of blue and red dyes

ratio. The SNR was estimated through repeated measurements of transmittance spectra as $\text{SNR} = \dfrac{\mu}{\sigma_{noise}}$ where μ is the mean recorded signal and σ_{noise} is the deviation within the set of repeated measurements. This was found to have an average of 75, 40 and 15 for blue, red and mixed samples respectively;

Results and Discussion

In order to evaluate the results of our estimator, we compare them against a more classical method that could also be used to solve the problem at hand, namely least-squares. In fact, the forward model we used (Beer-Lambert) is simple, and clearly defined, making LSQ an appropriate choice for the purpose of estimating the unknown parameter $\boldsymbol{\theta}$. We note that the transmittance spectra computed from MAP and LSQ estimates match

the measured data as demonstrated by Figure 5.5. This figure shows the transmittance spectra computed when $\boldsymbol{\theta} = (2.34 \text{ g/L}, 0)$ and $\boldsymbol{\theta} = (0, 0.9490 \text{ g/L})$ in 5.5a and 5.5b respectively.

As can be seen from Figure 5.5, the spectra computed from our estimates are very close to the expected values of $\boldsymbol{\theta}$. After further analysis of the data, however, we note two significant findings. Firstly, although the measured transmittance spectra and those computed from the LSQ and MAP estimates are often identical, the estimates provided by MAP are often closer to the expected values of $\boldsymbol{\theta}$ than their LSQ counterpart as illustrated by Figure 5.6.

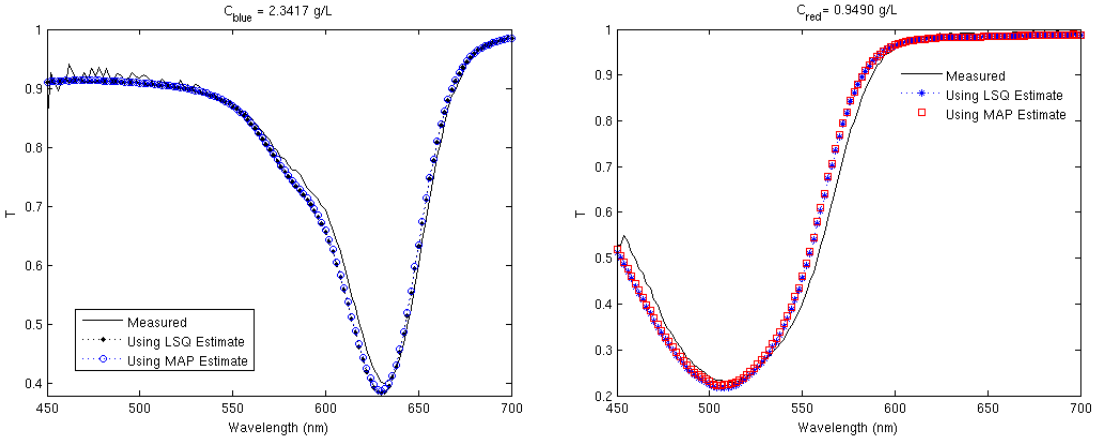

(a) Gelatin Phantom Containing Blue Dye (b) Gelatin Phantom Containing red Dye

Figure 5.5: These plots represent examples of measured transmittance spectra (solid line) against the spectra calculated using LSQ and MAP estimates.

In addition, we note that the advantages of using a Bayesian estimator are clearer when dealing with values that lead to the signal analysed being very low or when more than one value can be mapped to the measured signal. Sample R4 provides a good example as $\hat{\theta}^{red}_{\text{LSQ}} = 3.6939$ and $\hat{\theta}^{red}_{\text{MAP}} = 2.1508$ when $\theta^{red} = 2.64$ g/L. The difference between the actual value of $\boldsymbol{\theta}$ and the LSQ estimate can also be seen in Figure 5.6. The results of the experiment support the claim that using a Bayesian estimation method could improve the accuracy of the estimate. For samples M1, M2 and M3, we note that MAP provides

slightly better estimates than LSQ as depicted by Figure 5.7.

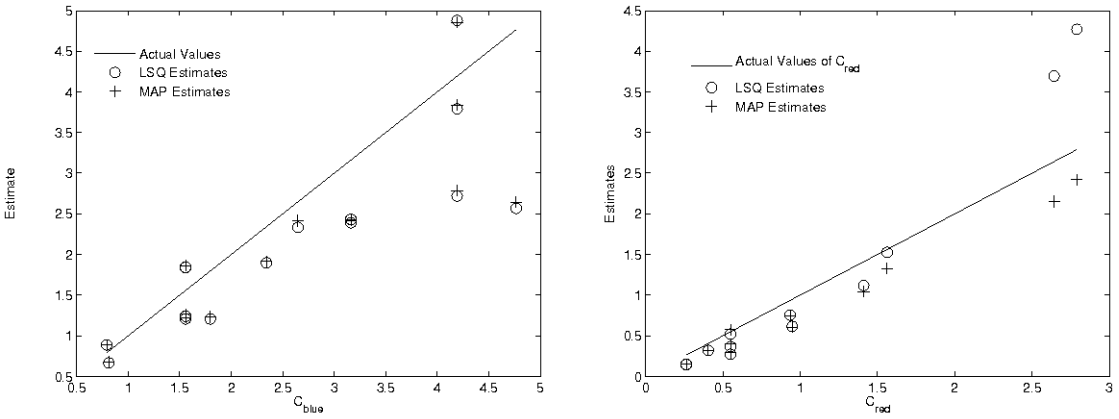

(a) Estimation Results: Blue Samples

(b) Estimation Results: Red Samples

Figure 5.6: This figure aims to evaluate the results of MAP and LSQ estimation in comparison with the actual values of $\boldsymbol{\theta}$. Figure 5.6a depicts the results of estimating the concentration of blue dye in sample B1-B11 while Figure 5.6b shows the estimates of red dye concentrations in samples R1-NR11. Note that for larger volume fractions of blue and red dyes, the estimates recorded using LSQ and MAP are less accurate than those obtained for smaller concentrations. This is due to the transmitted signal being weak at these high concentrations due to the relatively large absorbance of the samples.

Finally, we observe that the results of the MAP estimator on the gelatin phantoms are not as accurate as those obtained from the simulated data. This is due to two major factors. Firstly, we acknowledge that the levels of noise and uncertainty present in our system are much higher than those introduced in the simulated data. The collected transmitted signal includes an inherent level of errors, which comes from multiple sources. These include the light redirection using the mirror, the distance between the sample and light collection apparatus and the values used for the extinction coefficients of the various absorbing agents.

Secondly, the prior information used by the MAP estimator does not provide a significant advantage to the estimator over other classical methods. This is because the distribution of the prior data is very wide. In fact, all the prior data sets used in the estimation process have large ranges with standard deviations ranging between 65 and 88% of the

chromophore concentrations. In addition, the volume fractions of dyes used to prepare the samples often fell within the tails of the distribution rather than closer to the mean.

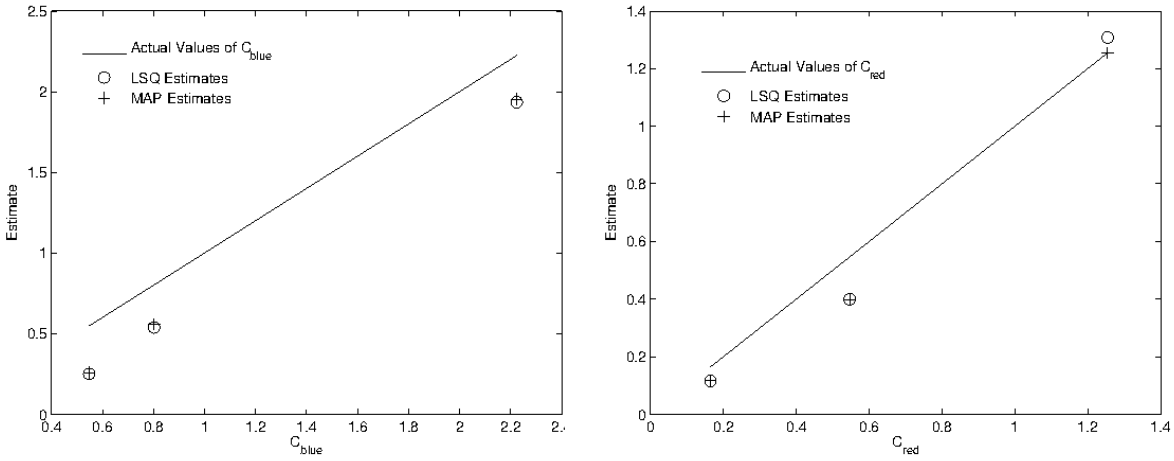

(a) Estimates of C_b for Samples M1,M2 and M3

(b) Estimates of C_{red} for Samples M1,M2 and M3

Figure 5.7: These plots represent the results of the estimation process using samples containing both red and blue dye (M1, M2 and M3). The difference between Map and LSQ estimates is smaller than that noted in samples with a single dye. This is mainly due to the weakness of the transmitted signal as the presence of two dyes in the phantoms leads to a large fraction of the light being absorbed.

Consequently, the prior probability is always low, regardless of whether or not the actual value of the unknown parameter is in close proximity to the mean of the prior data set. Therefore, the wider the prior distribution is, the closer MAP's estimate will be to the results of classical estimation techniques. A possible solution is to gather as much information about the unknown parameter as possible, thus making the prior distribution sharper.

5.3 Scattering Phantoms

We prepare another set of gelatin phantoms, similar to the ones described in Section 5.2, but with the addition of milk as a known scattering medium. We use the same apparatus depicted in Figure 5.1 to collect the transmitted light from the scattering phantoms. We use the Kubelka-Munk method described in Section 2.4.2 to calculate the phantoms

transmittance spectra from estimated optical parameters. To that aim we require a number of input parameters, namely:

- Volume fractions of red and blue dyes.
- Extinction coefficients of dyes.
- Absorption coefficient of the gelatin solution.
- Reduced scattering coefficient of milk
- Refractive index of the sample.
- Sample thickness.

We use the same extinction coefficients and gelatin absorption coefficient that were used to estimate the parameters of the non-scattering phantoms and use commercially available skimmed milk as a scattering medium. We thus use a MATLAB program developed by Matzler (Matzler, 2002) to calculate the scattering cross section using Mie theory. This is then used in equation (5.1) to calculate the scattering coefficient where ρ_i is the density of scattering particles i and σ_i is the scattering cross section which depends on the size and shape of the particles i, as well as the refractive index of the scattering particles and medium (Mourant et al., 1997).

$$\mu_{s_i}(\lambda) = \rho_i.\sigma_i(\lambda) \tag{5.1}$$

Figure 5.8a and Figure 5.8b show the reduced scattering coefficient of milk as calculated using Matzler's program as well as the reduced scattering coefficients of various milk samples as reported in (Qin and Lu, 2007). During sample preparation, only a small quantity of milk ($\sim$ 8 g) is mixed with the gelatin solution which greatly reduces the number of scattering particles in our samples. Consequently, we cannot directly use the reported values of milk reduced scattering coefficient as they do not correctly reflect the milk content in the samples. We therefore use Matzler's program to estimate the reduced scattering coefficient of the diluted milk solution. The following section describes how the

reduced scattering coefficient of milk was determined.

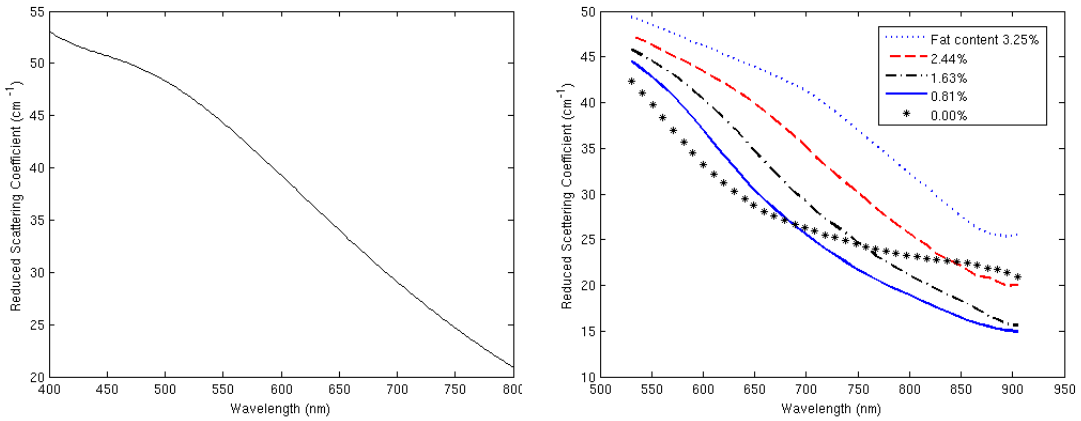

(a) (b)

Figure 5.8: Reduced scattering coefficients of milk obtained from two different sources. (a): The reduced scattering coefficient is calculated using Matzler's program. This value was generated for a sample containing 100% skimmed milk. As reported on the milk container, 100 ml of milk contains 0.3g of fat and 3.6g of protein. These values are consequently used to construct the volume fractions of scattering particles in milk. (b): Values reported by Qin in and obtained directly from the authors.

5.3.1 Scattering Properties of Milk

As described by Qin in (Qin and Lu, 2007), fat globules and casein micelles are believed to be the main contributors to light scattering in milk. Milk also contains whey proteins, however, they are far too small to have a substantial effect on scattering events in milk (Qin and Lu, 2007). As mentioned earlier, we use commercially available skimmed milk that contains 0.3 g of fat and 3.6 g of protein per 100 ml of milk. To model the volume fractions of fat and protein in our samples, we first calculate w_{fat} and w_{casein}, the weights of fat and casein within our samples using the following equations:

$$w_{fat} = w_{milk} * \frac{0.3\,\mathrm{g}}{100\,\mathrm{ml}} \qquad w_{casein} = w_{milk} * 0.76 * \frac{3.6\,\mathrm{g}}{100\,\mathrm{ml}} \tag{5.2}$$

Note that we use the factor 0.76 to calculate the weight of casein, as casein micelles form about 76% of the protein volume fraction of milk (Frisvad et al., 2007; Fox and McSweeny, 1998). We can now transform these quantities to volume fractions using the

following equations, where $\rho_{fat} = 0.915$ g/ml is the density of milk fat, $\rho_{protein} = 1.11$ is the density of milk protein and $\rho_{milk} = 1.03$ is the density of milk (Frisvad et al., 2007; Walstra and Jenness, 1984)

$$vf_{fat} = \frac{w_{fat}/\rho_{fat}}{w_{sample}/\rho_{milk}} \qquad vf_{casein} = \frac{w_{casein}/\rho_{protein}}{w_{sample}/\rho_{milk}} \tag{5.3}$$

We set the refractive index of fat globules in milk to 1.46 and casein micelles to 1.503 as reported in (Frisvad et al., 2007; Attaie and Richtert, 2000). We then calculate the scattering coefficient using the parameters above as input arguments to Matzler's MATLAB program (Matzler, 2002) as described in Section 5.3. We note that Matzler's software (Matzler, 2002) calculates the scattering coefficient μ_s and anisotropy factor g for each scattering particle. Consequently, we still need to determine the optical properties of the medium as a whole (milk) rather than the components it contains.

To that effect, we accept that we can sum up the scattering coefficients of the particles to calculate the combined scattering coefficient as described in (Van De Hulst, 1981; Frisvad et al., 2007). This is only possible because we assume that the various particles scatter light independently of each other (Frisvad et al., 2007). Once the scattering properties of the individual particles, and the scattering coefficient of the medium are calculated, we can use equation (5.4) to calculate the anysotropy factor of the medium (Frisvad et al., 2007).

$$g_{milk} = \frac{g_{fat} \cdot \mu_{s_{fat}} + g_{casein} \cdot \mu_{s_{casein}}}{\mu_{s_{milk}}} \tag{5.4}$$

Let the unknown parameter be $\boldsymbol{\theta} = (\mathrm{c_{blue}}, \mathrm{c_{milk}})^{\mathrm{T}}$. All other parameters required for our forward model are provided as predefined input arguments. We accept that uncertainty is present in various input parameters such as the properties of milk, the extinction coefficients of the dyes and the absorption coefficients of the gelatin base. We also introduce an additional level of uncertainty by setting d to an average value drawn from the distribution of sample thicknesses.

We prepare a set of six phantoms containing a gelatin solution, milk and a small amount of blue dye. All samples contain the same type of milk (from the same container) but with slightly varying quantities of dye. Table 5.4 describes the quantities used to prepare the phantoms in terms of volume fractions of dye, milk and gelatin as well as sample thickness. Similarly to the experiments described in Section 5.2, we estimate the unknown parameter $\boldsymbol{\theta}$ using two techniques: maximum *a posteriori* and least-squares methods, then compare the results.

Sample	c_{blue} (%)	w_{milk} (g)	c_{gelatin} (%)	d (cm)
B1	$1.91\,e^{-2}$	3.23	3.47	0.41
B2	$4.10\,e^{-2}$	3.23	3.47	0.39
B3	$6.63\,e^{-2}$	3.22	3.47	0.43
B4	$9.69\,e^{-2}$	3.22	3.47	0.43
B5	0.15	3.22	3.47	0.44
B6	0.19	3.22	3.47	0.37

Table 5.4: Structure of Blue Gelatin Phantoms in terms of the main absorbers (blue dye and gelatin base) and scatterers (milk)

Results and Analysis

As depicted in Figure 5.9, the MAP estimates are not as accurate as those obtained from applying the same inversion method to non-scattering phantoms or to simulated skin data. For instance, when considering the estimates of dye volume fraction, we note that the values returned by the least-square method are often closer to the expected values than their MAP counter part. We also note that both LSQ and MAP estimates of dye volume fractions have an unacceptably high error level ranging between $[4 - 53\%]$ and $[26 - 135\%]$ for MAP and LSQ respectively.

However, the MAP estimates for milk concentration are often more accurate than LSQ estimated values as depicted in Figure 5.9. Figure 5.9 also shows that although closer to the expected values than their LSQ counterparts, MAP estimates are quite inaccurate and the error levels, summarised in Table 5.5 are far beyond the values observed when using

Sample	c_{milk} LSQ Error (%)	c_{milk} MAP Error (%)
1	59.06	24.70
2	26.28	52.84
3	94.33	3.87
4	114.56	11.30
5	135.18	24.99
6	35.49	48.31

Table 5.5: Estimation errors generated from LSQ and MAP based methods applied on measured transmittance from the blue gelatin phantoms. These errors are calculated for the blue dye volume fraction estimates as $\frac{\sqrt{(c_{milk} - \hat{c}_{milk})^2}}{c_{milk}}$

simulated data as described in Chapter 4.

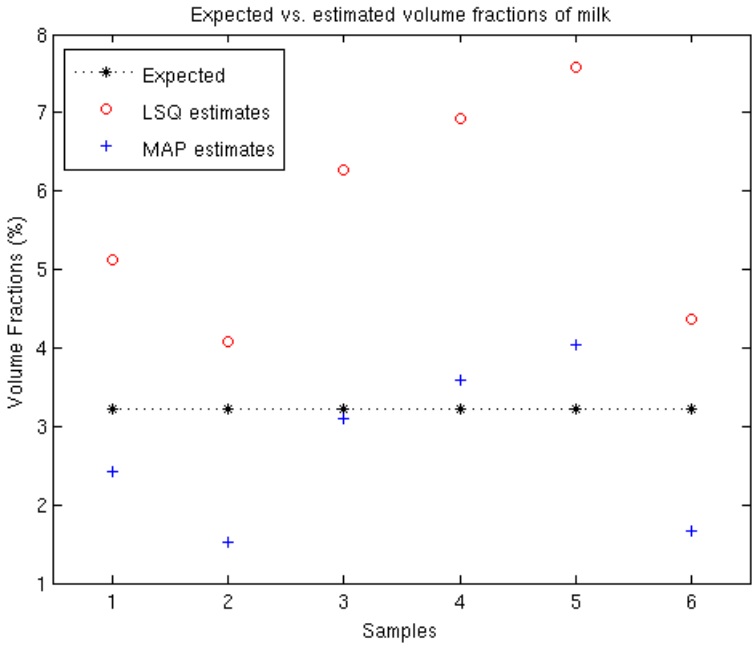

Figure 5.9: Estimates of Milk Volume Fractions in Samples

We thus have to consider these results with caution as they may not accurately reflect the performance of our estimation method due to the high level of inaccuracy in our model. In fact, we believe that the inaccuracy of the forward model is one of the main reasons behind the high level of errors in both estimation methods (LSQ and MAP). Figure 5.10

depicts the measured vs. calculated transmittance spectra, where the expected value of $\boldsymbol{\theta}$ is used to generate T. One can see that the measured spectra does not accurately match the measured data.

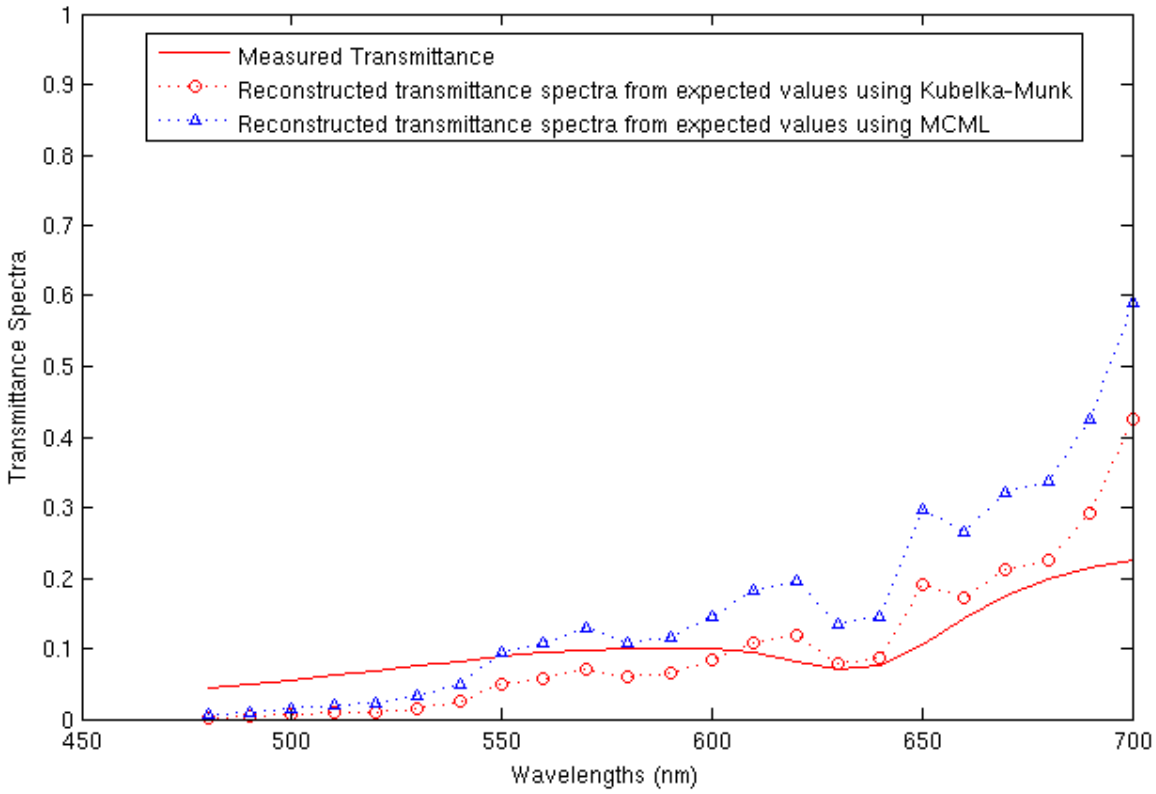

Figure 5.10: Measured transmittance spectra from Sample 5 plotted against reconstructed spectra from the expected value of $\boldsymbol{\theta}$. Transmittance was reconstructed using two methods: a Kubelka-Munk based model and an MCML model. Note that the spectra are considerably distant making both forward models inherently inaccurate.

This is not due to the modelling method used (Kubelka-Munk vs. MCML for example) as both methods were initially used to generated transmittance spectra, and their results were comparable, but equally inaccurate in comparison with the measured data. This is due to the large amount of noise that exists within the imaging setup, as well as the large uncertainty within the absorption spectra used as demonstrated by Figure 5.2a and Figure 5.2b. In fact, obtaining consistent values for these parameters was one of the main challenges encountered during these experiments, which made it very difficult to validate

the forward model.

It is worth noting that although the MAP based estimation is meant to deal with uncertainty within the forward model, it is not meant to solve problems that are incorrectly specified. That is to say, uncertainty in the model's parameters is only tolerated if the underlying model is correct. We can further show that the inaccuracy of the estimates may be due to the high level of inaccuracy in the forward model. This is achieved by estimating the same parameters using spectra reconstructed from ground truth values with added noise. We ensure that the added noise has a high level where SNR ≈ 50.

Figure 5.11 shows that both MAP and LSQ estimates are very close to the expected values when generated from reconstructed spectra where error levels are in the range $5 - 36\%$. We also observe that in this instance, MAP based estimation provides results that are as accurate, if not more accurate than LSQ estimates. This suggests that our inversion method performs well on the simulated data as the model accurately describes the tissue. However, when the model does not match the physical reality, we note that our method does not perform as well as previously observed. One solution would be to use a more advanced model to describe our gelatin phantoms, such as MCML. This would involve defining a larger number of parameters such as the physical and optical characteristics of the petri dishes used to prepare the phantoms.

We also investigated the effect of prior data on MAP estimation for all samples. We note that the original prior data used in this experiment had acceptable ranges of standard deviations of $[26 - 34\%]$ of mean volume fractions. Reducing the width of the prior distribution to $\sim 20\%$ does not improve the accuracy of the results in this case. This is also due to the fact that reducing the width of the distribution makes the expected values fall on the tails of the probability distribution curves, rather than closer to the mean. This further suggests that even though uncertainty in the model's parameters is tolerated by our method, the underlying model must be right for the inversion method to succeed.

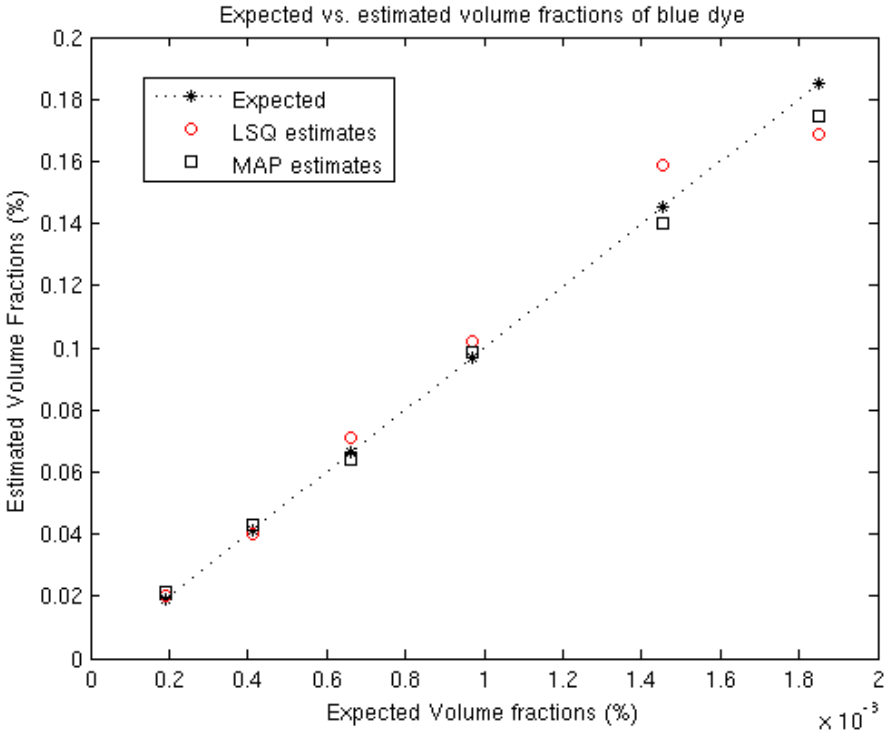

Figure 5.11: Estimates of the value fractions of blue dye in samples. These estimates are obtained from simulated transmittance spectra + Gaussian noise rather than measured data. This is to investigate whether the inaccuracies of the previous estimates where due to the estimation method, prior data, uncertainty level in input parameters or the inaccuracy of the forward model.

5.4 Conclusion

We demonstrated that the use of a Bayesian based method to recover the optical properties of a medium can lead to a substantial increase in the accuracy of the recovery process. We have established that in the presence of a certain level of uncertainty in the underlying model of the tissue, the MAP based estimator provides accurate results both in terms of the recovered parameter and variation. Maximum *a posteriori* also successfully recovers unknown parameters where other classical methods (LSQ) fail. This is potentially important when applied on tissues who's physical characteristics are not described with high precision, or in the presence of variations within the information about the unknown parameter.

However, we note that the accuracy of Bayesian estimation is strongly reliant on the quality of the data contained in the prior information set. In fact, a largely flat prior

distribution, resulting from wide variations within the data, may not lead to any improvement over other statistical methods such as maximum likelihood. This is due to the fact that a wide distribution of the prior data would lead to a very small prior probability even when the estimate is close to the prior mean. This, in turn, suggests that in such cases, the MAP estimator becomes equivalent in its performance to a maximum likelihood based estimator. It is thus important to choose a prior that describes the unknown parameter as accurately as possible.

We also observe that although our inversion method aims to be robust against high levels of uncertainty, it is still important that the forward model is correct. As seen in Section 5.3.1, the use of a model that does not correctly capture the properties of the tissue would lead to inaccurate estimation results. This is not a limitation of the inversion method as one of the fundamental assumptions when using a model-based inversion method is that the model can be defined with some accuracy. It is therefore important to verify that the forward model used is correct even if some of the parameters are uncertain.

We conclude that our inversion method provides excellent results when applied to simulated data. It also provides good results when applied to experimental data when the underlying model is correctly defined, but some parameters are uncertain. However, our inversion method does not overcome the limitations of having the forward model incorrectly describes the physical properties of the sample. We have therefore shown that two main factor that could affect the performance of our estimator are:

- A prior distribution that provides as much information about the parameters as possible.
- A forward model that, albeit open to uncertainty in the parameters, correctly captures the properties of the tissue.

In the next chapter, we describe how we apply our inversion algorithm to measurements collected from colon samples. These same samples were used to validate a model of the

human colon in a previous study (Hidovic-Rowe, 2006), thus removing the effects of using an incorrect forward model as part of the estimation process.

Chapter 6

Application to Multispectral Images of the Colon

6.1 Introduction

The colon is a good example of a multi-layered biological medium that has often been studied due to the fact that colorectal cancer is the third most common cancer (GLOBOCAN, 2008). It is also an excellent example of a medium for which the mapping between its optical properties and its reflectance data is not one-to-one (Hidovic-Rowe, 2006). This makes it very challenging to extract the parameters of the tissue using commonly used inversion methods. We therefore apply our inversion algorithm to multispectral images of the colon in order to recover the mucosal thickness, haemoglobin volume fraction as well as size and density of scattering particles.

In this chapter, we will describe the structure of the colon tissue and some of the disorders that might occur and cause the tissue's parameters to change. We also give a brief description of the forward model that was initially developed by (Hidovic-Rowe, 2006) and used to model light reflectance in the human colon tissue. We will then describe how our inversion method was applied to the simulated and experimental data and evaluate the results obtained.

6.2 Structure of the Human Colon

The colon tissue consists of four layers: the mucosa, submucosa, muscularis propria, and serosa (Day et al., 2003). The mucosa is the innermost layer of the colon. Its thickness varies between 395 and 600 μm in a normal tissue and it can also be broken down into the epithelium, lamina propria and muscularis mucosa (Huang et al., 2004; Hidovic-Rowe, 2006). The epithelium is a single layer of epithelial cells with a diameter of $10 - 20\,\mu m$, making up a thickness of approximately $25\,\mu m$. It is followed by the lamina propria, a layer of loose connective tissue that mainly consists of thin collagen fibrils as well as various other cell types. This layer also has a dense network of small blood capillaries that nourish the epithelium and which become larger deeper in the mucosa. Finally, the muscularis mucosa is a thin and smooth muscle layer that separates the mucosa from the submucosa.

The submucosa is a $415 - 847\,\mu m$ thick layer of dense connective tissue beneath the mucosa. It contains large collagen fibres and blood vessels that are significantly larger than those found in the mucosal layer. It is followed by the muscularis externa (propria), a smooth muscular layer with a thickness of $600 - 1100\,\mu m$ (Huang et al., 2004; Hidovic-Rowe, 2006). It consists of a layer of circular muscle, wrapped around the colon that is aimed at moving waste material through the colon. It also contains an outer layer of longitudinal muscle, that runs lengthwise along the colon and works along the circular muscle to create the wavelike motion. Finally, the serosa is the outermost layer of the colon and consists of a squamous epithelium, loose connective tissue and large blood vessels (Huang et al., 2004; Hidovic-Rowe, 2006).

6.3 Reflectance Model of the colon

When the tissue is exposed to light, it first interacts with the epithelium layer (in the mucosa). As the epithelium layer is very thin, and is characterised by an anisotropy factor of 0.98, the epithelium acts as a strong forward scatterer. This means that most of the light that interacts with the epithelium is propagated to the deeper layers (Hidovic and

Rowe, 2004).

Once the light enters deeper into the mucosa, it is scattered by the loosely connected collagen fibrils. Within the mucosa, a proportion of the light is also absorbed by the oxy- and deoxy haemoglobin present in the capillaries. A small fraction of the light is then reflected at the submucosa boundary while most of it travels deeper into the submucosa which, as previously mentioned, mainly consists of collagen fibres. This makes the submucosa strongly forward scattering (Hidovic-Rowe and Claridge, 2005). Light is further absorbed at this layer due to the haemoglobin present in the arteries and veins. The proportion of light that reaches the muscular layer is further absorbed or scattered with an anisotropy factor estimated to be 0.96 (Hidovic-Rowe, 2006). The large number of scattering events that occur in this layer means that only a very small fraction of the light in the muscular layer reaches the deeper layers of the colon.

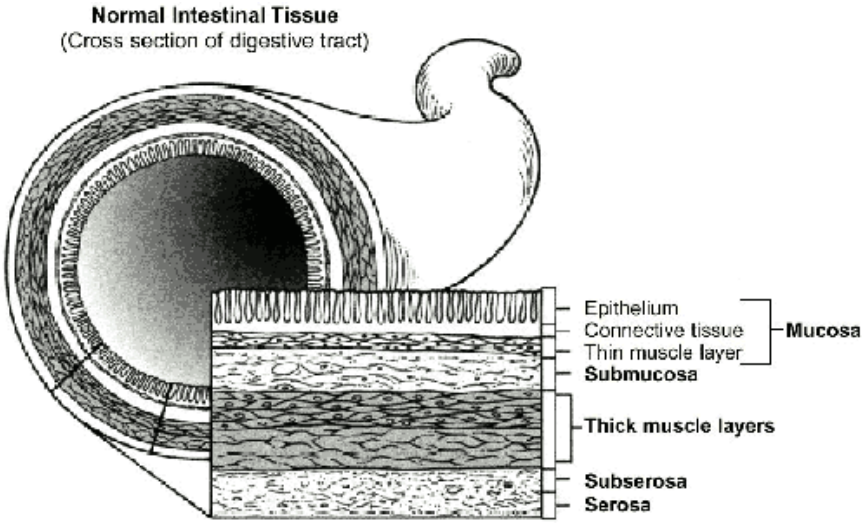

Figure 6.1: Multi-layer structure of the human colon *

Hidovic-Rowe and Claridge (2005) have shown that the exclusion of the epithelium layer and the serosa from a computational model of light propagation in the colon had no significant effect on the amount of light remitted at the colon surface. Consequently, the forward model of light transfer in the colon can be simplified to only include three layers:

*Structure of the Human Colon, http://www.babymed.com/cancer/colon-cancer-diagnosis-and-staging

The mucosa, submucosa and muscularis externa. As the model described in (Hidovic-Rowe, 2006; Hidovic-Rowe and Claridge, 2005) has been validated against real data, we use it with no modifications as part of our inversion process, i.e. to generate the reflectance spectra R. We also use the Monte-Carlo method described in Section 2.4.3 to model light transport in the tissue. To that effect, we require five input parameters for each layer, namely: The absorption and scattering coefficients, refractive index, anisotropy factor and layer thickness. As the scattering and absorption coefficients for the mucosa and submucosa are not readily available in the literature, we model both of these quantities as described in the following section and discussed in detail in (Hidovic-Rowe, 2006). All the property values used in this thesis were collected from (Hidovic-Rowe, 2006).

6.3.1 Modelling absorption

The composition of the colon, as outlined in Section 6.1, indicates that haemoglobin is the main absorber in the colon. We can therefore use Equation (6.1) to represent the absorption coefficient of the various layers of the colon, where i is the layer index, $\mathrm{C}_{i_{\mathrm{HB}*}}$ is the volume fraction of blood in the i^{th} layer, S_i is the oxygen saturation and μ_a^{Hb} and $\mu_a^{\mathrm{HbO_2}}$ are the absorption coefficients of haemoglobin and oxy-haemoglobin respectively. As described in (Hidovic-Rowe, 2006), we will use a value of 120 g/L to represent the concentration of haemoglobin per unit volume of blood in the colon and we use the molar extinction coefficients published by Prahl (Prahl, 2007a).

$$\mu_{a_i}(\lambda) = ln(10).\mathrm{C}_{i_{\mathrm{HB}*}} \Big((1 - S_i)\mu_a^{\mathrm{Hb}}(\lambda) + S_i \mu_a^{\mathrm{HbO_2}}(\lambda) \Big) \tag{6.1}$$

6.3.2 Modelling Scattering

We assume that scattering particles within the various layers of the colon are homogeneous spheres by average size and density. This assumption, though not strictly true, can be used as an approximation as recent studies by Chen *et al.* (Chen et al., 2004) suggest that this is a valid approximation and is generally accepted as a method of modelling scattering in biological tissues. We thus use Metzler's MATLAB program as described in Section 5.3 to calculate the scattering cross section using Mie theory (Matzler, 2002).

This is then used in (5.1) to calculate the scattering coefficient (Mourant et al., 1997).

Throughout the modelling process, we make a number of assumptions regarding the scattering coefficient of the colon. We assume that the absorbance of the scattering particles is negligible, and thus the imaginary part of the refractive index is set to 0. We also assume that the refractive indices of the scattering particles and surrounding medium are equal for all wavelengths in the range of visible light.

Parameter	Mucosa	Submucosa	Muscularis Externa
Blood Volume Fraction	$1 - 10\%$	$5 - 20\%$	–
Haemoglobin Saturation	$50 - 75\%$	$50 - 80\%$	–
Size of Scattering Particles (μm)	$0.1 - 1.74$	$1 - 6$	–
Density of Scattering Particles	$4 - 20\%$	$15 - 60\%$	–
Thickness (μm)	$395 - 603$	$415 - 847$	900
Anisotropy Factor	$0.5 - 0.95$	$0.95 - 0.99$	0.96
Refractive Index of Medium	1.38	1.36	1.36
Refractive Index of Particle	1.46	1.38	–

Table 6.1: Summary of ranges used as model input parameters to generate colon reflectance spectra (Hidovic-Rowe, 2006)

To further simplify the model, we assume that all organelles present in the mucosal layer contribute a negligible amount to scattering, and we thus only use the properties of collagen fibrils in the mucosa to model the parameters of the mucosal layer. Finally, we assume that the sizes, shapes and densities of the scattering particles are the same within each layer. The remaining parameters have been described in details in (Hidovic-Rowe, 2006) and their values and ranges are summarised in Table 6.1.

As stated in (Hidovic-Rowe and Claridge, 2005), the parameters of the mucosa had the highest effect on the reflectance spectra while varying the parameters of the submucosa did not have a significant effect on the shape of the reflectance spectra. It was thus concluded that using a set of predetermined constant values (rather than ranges) for the submucosal parameters would result in a less complex forward model while still maintaining its correctness. This would of course introduce a small error but it was judged to be acceptable

for our purposes. Consequently, we used the values described in Table 6.2 to describes the parameters of the submucosa.

Volume fraction of blood	Oxygen saturation	Diameter of scatterers	Volume fraction of scatterers	Thickness
20%	75%	3.5 μm	50%	700 μm

Table 6.2: Parameters used to model the submucosal layer of the colon. The parameters are within the reported acceptable ranges 6.1. These values were chosen to 1. simplify the forward model used in the estimation process, 2. to introduce uncertainty in the inversion process by taking default values of uncertain parameters rather than taking their exact values, or estimating them as part of the inversion process

6.4 Histological Changes in Cancerous Tissue

For the purposes of this research, we take colorectal adenocarcinoma as the main example of cancer that effects the colon tissue, as 95 % of colorectal cancers are of this type. In this section, we summarise the main changes that occur in the colon due to colorectal adenocarcinoma as described in (Hidovic-Rowe, 2006). Further details about some of the most common histological changes in the colon are described in (Hidovic-Rowe, 2006; Skinner et al., 1995; Ge et al., 1998; Hilska et al., 1998; Furuya and Ogata, 1993; Turnay et al., 1989).

Colorectal adenocarcinoma is thought to develop over a number of years, and is often preceded by a number of changes in the mucosa lining of the colon or rectum. These changes are characterized by cell proliferation and nuclei enlargement (Hidovic-Rowe, 2006). They are also accompanied by changes in the structure and organization of other components, such as the blood and collagen content and thickness of the mucosa. Skinner *et al* (Skinner et al., 1995) found that the blood vessels within a carcinoma would be disorganised, with an increased size and density compared with a normal tissue which leads to an increased blood flow.

Haemoglobin saturation was also found to change in abnormal tissue as depicted in (Hidovic-Rowe, 2006; Ge et al., 1998). In addition, Hilska *et al* report in (Hidovic-Rowe,

2006; Hilska et al., 1998) that the collagen structure is also disturbed in abnormal tissue. This was also supported by Furuya and Ogata (Furuya and Ogata, 1993) whose main finding was that the density of collagen increases in the central region of the cancer, while it decreases towards the margins of the tumour due to the presence of looser networks of thinner collagen fibrils.

This was also confirmed by (Turnay et al., 1989) who found that the collagen content increases in the first stages of adenocarcinoma, and decreases during its development. Finally, the thickness of the mucosal layer can also be affected in the early stages of cancer development, especially if the tumour develops from polyps, in which case, the thickness will increase (Hidovic-Rowe, 2006). However, the mucosal layer will have a smaller thickness in a tumour that developed from suppressed lesions on the tissue surface (Hidovic-Rowe, 2006).

In summary, we note that only four of the parameters used to model light reflectance in the colon tissue exhibit a change between normal and abnormal tissues, namely: blood volume fraction, scatterer density, scatterers diameters and thickness of the mucosal layer. Consequently, we aim to recover these four parameters using our inversion method. This is achieved in two steps. First, we apply our inversion method to simulated reflectance data of the human colon. This allows us to evaluate the accuracy of our method in a controlled setting as described in Section 6.5. We then apply the inversion algorithm to reflectance spectra extracted from multispectral images of the colon. Note that all images used in this thesis were obtained by Hidovic-Rowe in (Hidovic-Rowe, 2006). The details of the image acquisition setup and the algorithm used in (Hidovic-Rowe and Claridge, 2005; Hidovic-Rowe et al., 2006) to extract reflectance spectra are summarised in Section 6.6.

6.5 Simulated Data

As the first stage of our inversion process, we generate simulated reflectance data from the human colon. We use the forward model summarised in Section 6.3 and described in details in (Hidovic-Rowe, 2006) to describe the colon. We take our unknown param-

eter vector to be $\boldsymbol{\theta} = (\mathrm{C}_{\mathrm{HB}*}, \mathrm{diam}_{\mathrm{clg}}, \mathrm{C}_{\mathrm{clg}}, d)^{\mathrm{T}}$. We use the MCML program to generate reflectance spectra for 144 values of $\boldsymbol{\theta}$. The values of $\mathrm{C}_{\mathrm{HB}*}, \mathrm{diam}_{\mathrm{clg}}, \mathrm{C}_{\mathrm{clg}}$ and d are chosen from the range of normal values described in Table 6.1. We use the values in Table 6.2 and those summarised in the "muscularis externa" column of Table 6.1 as input arguments to the MCML program.

To that aim, we generate an MCML input file for each value of $\boldsymbol{\theta}$, describing the refractive indices for the top and bottom ambient layers, namely: air (1.0). The input files also provide the parameters describing each layer of the colon: the refractive index, the absorption coefficient (cm), the scattering coefficient (cm), the anisotropy factor, and the thickness (cm). The absorption and scattering coefficients are calculated using the values of $\boldsymbol{\theta}$ as described in sections 6.3.1 and 6.3.2. Note that when using MCML, we assume that the photons are injected orthogonally into the tissue, leading to collimated beam of photons.

We therefore generate 144 reflectance spectra for wavelengths λ = [480, 506, 514, 522, 540, 548, 560, 564, 568, 574, 580, 586, 594, 610, 620, 630, 640, 676, 700]. We also use the same ranges listed in Table 6.1 as the prior data required for our MAP based estimator as depicted in Table 6.3. Once the simulated reflectance is generated, we add Gaussian noise of a known variance σ^2_{noise}.

θ_i	MEAN	STD (%)
$\mathrm{C}_{\mathrm{HB}*}$	5.40	2.55 (47.21%)
$\mathrm{C}_{\mathrm{clg}}$	12.20	4.63 (37.94%)
$\mathrm{diam}_{\mathrm{clg}}$ (μm)	0.4264	0.1826 (42.82%)
d (cm)	0.0501	0.0060 (11.89%)

Table 6.3: Basic statistical properties of the prior data used in the estimation process. The prior distribution is assumed normal and these values were chosen to include the range of allowed values described in Table 6.1

Next, we apply the inversion method to the simulated data which, as demonstrated in Section 4.4.2, can be reduced to the minimisation problem represented by Equation

(4.15). We use the MATLAB function LSQNONLIN[†] (Optimization Toolbox) with the Levenberg-Marquardt algorithm, to minimise our objective function. LSQNONLIN is a function provided as part of the MathWorks Optimisation Toolbox to solve non-linear least-squares problems, including non-linear data-fitting problems (**?**).

We also use the Parallel Computing Toolbox (MathWorks) to parallelise the process, and thus reduce the time required for the completion of the optimisation procedure. We take x_n to be the noisy simulated data, $R_n(\boldsymbol{\theta})$ as the reflectance spectra and σ^2_{noise} to be the variance of noise we introduced to the reflectance spectra. We summarise the process used to generate the simulated reflectance spectra and apply our inversion method in Algorithm 6.1.

$$objFunc = \frac{1}{2\sigma^2_{noise}} \sum_{n=1}^{N} (x_n - \mathrm{R}_n(\boldsymbol{\theta}))^2 + \sum_{i=1}^{m} \frac{(\theta_i - \mu)^2}{2\sigma^2_{\theta_i}} \tag{6.2}$$

[†]LSQNONLIN, http://www.mathworks.co.uk/help/optim/ug/lsqnonlin.html

Algorithm 6.1 MAP Estimation Process

Data:
$\sim N(\mu_{\mathrm{C_{HB*}}}, \sigma^2_{\mathrm{C_{HB*}}})$: Prior distribution of haemoglobin volume fraction in the mucosa
$\sim N(\mu_{\mathrm{diam_{clg}}}, \sigma^2_{\mathrm{diam_{clg}}})$: Prior distribution of collagen diameter in the mucosa
$\sim N(\mu_{\mathrm{C_{clg}}}, \sigma^2_{\mathrm{C_{clg}}})$: Prior distribution of collagen density in the mucosa
$\sim N(\mu_d, \sigma^2_d)$: Prior distribution of mucosal thickness
$\mathrm{RANGE}_{\mathrm{C_{HB*}}}$ = [0.04; 0.07; 0.1]: Values of haemoglobin volume fractions used.
$\mathrm{RANGE}_{\mathrm{diam_{clg}}}$ = [0.1; 0.3; 0.5; 0.74]: Diameters of scattering particles used.
$\mathrm{RANGE}_{\mathrm{C_{clg}}}$ = [0.04; 0.1; 0.15; 0.2]: Volume fractions of scattering particles used.
RANGE_d = [0.0395; 0.0595; 0.0603]: Mucosal thicknesses
RANGE_λ = [480, 506, 514, 522, 540, 548, 560, 564, 568, 574, 580, 586, 594, 610, 620, 630, 640, 676, 700]: Wavelengths (nm)
$runMCML(\lambda, \theta)$: function to calculate the reflectance spectra at wavelength range λ and parameter vector $\boldsymbol{\theta}$,
σ^2: Variance of the measured spectra (or in this case, the variance of $runMCML(\lambda, \theta)$ + noise
begin
for all $\mathrm{C_{HB*}} \in \mathrm{RANGE}_{\mathrm{C_{HB*}}}$ **do**
  for all $\mathrm{diam_{clg}} \in \mathrm{RANGE}_{\mathrm{diam_{clg}}}$ **do**
    for all $\mathrm{C_{clg}} \in \mathrm{RANGE}_{\mathrm{C_{clg}}}$ **do**
      for all $d \in \mathrm{RANGE}_d$ **do**
        $\mathrm{R_{simulated}} := runMCML(\mathrm{RANGE}_\lambda, \boldsymbol{\theta}) + \text{noise}$
        $$\hat{\boldsymbol{\theta}}_{MAP} := \arg\min_{\boldsymbol{\theta}} \left[\frac{1}{2\sigma^2} \sum_{n=1}^{N} (\mathrm{R_{simulated}} - runMCML(\mathrm{RANGE}_\lambda, \boldsymbol{\theta}))^2 + \frac{(\theta_1 - \mu_{\mathrm{C_{HB*}}})^2}{2\sigma^2_{\theta_{\mathrm{C_{HB*}}}}} + \frac{(\theta_2 - \mu_{\mathrm{diam_{clg}}})^2}{2\sigma^2_{\theta_{\mathrm{diam_{clg}}}}} + \frac{(\theta_3 - \mu_{\mathrm{C_{clg}}})^2}{2\sigma^2_{\theta_{\mathrm{C_{clg}}}}} + \frac{(\theta_4 - \mu_d)^2}{2\sigma^2_{\theta_d}} \right]$$
      end for
    end for
  end for
end for
end

6.5.1 Results and Discussion

Using Algorithm 6.1, we estimate the unknown parameter $\boldsymbol{\theta} = (\mathrm{C}_{\mathrm{HB}*}, \mathrm{diam}_{\mathrm{clg}}, \mathrm{C}_{\mathrm{clg}}, d)^{\mathrm{T}}$ from simulated reflectance spectra. We therefore collected 48, 36, 48 and 36 estimates for each value of $\mathrm{C}_{\mathrm{HB}*}$, $\mathrm{C}_{\mathrm{clg}}$, $\mathrm{diam}_{\mathrm{clg}}$, and d respectively used in our simulations. The results are summarised in Table A.1.

An initial visual inspection of the results indicates that the estimation process did not yield results as accurate as those obtained from simulated skin reflectance data. As shown in Figure 6.2, we note that the range of estimates was much larger than previously reported for simulated skin data. Table 6.4 shows that even though the mean values of the estimates were not very close to the expected values, the distribution of the estimates was reasonably narrow as demonstrated by standard deviation numbers ranging between 6 and 27%. This behaviour was expected due to the wide prior distributions used in our estimator as shown in Table 6.3.

	Expected	MEAN	STD	ERROR mean %	ERROR min-max %
$\mathrm{C}_{\mathrm{HB}*}$(%)	4.0	4.69	1.21 (25.86%)	26.56	$2.3 - 76.00$
	7.0	6.65	1.01 (15.23%)	12.33	$0.36 - 36.01$
	10.0	7.84	1.05 (13.48%)	21.54	$5.55 - 46.24$
$\mathrm{C}_{\mathrm{clg}}$	4.0	3.97	1.07 (27.21%)	22.06	$0.56 - 55.43$
	10.0	8.60	2.13 (24.75%)	20.48	$0.42 - 55.97$
	15.0	11.19	2.74 (24.46%)	25.49	$0.5 - 60.48$
	20.0	13.61	3.27 (24.06%)	31.92	$7.56 - 63.77$
$\mathrm{diam}_{\mathrm{clg}}$	0.10	0.44	0.06 (14.60%)	—	—
	0.30	0.45	0.03 (7.19%)	50.14	$32.05 - 67.82$
	0.50	0.44	0.03 (6.0%)	10.62	$2.30 - 20.62$
	0.74	0.45	0.03 (6.63%)	39.05	$31.14 - 45.68$
d	0.0395	0.0438	0.0099 (22.69%)	24.05	$0.06 - 52.86$
	0.0595	0.0498	0.0104 (20.89%)	16.47	$0.059 - 65.94$
	0.0603	0.0498	0.0109 (21.81%)	17.50	$0.007 - 64.34$

Table 6.4: A summary of a basic statistical analysis of the estimation results in terms of mean, standard deviation and range of errors.

Table 6.4 also shows that the level of errors in the estimates was high. This was exhibited more prominently when the expected values were on the edges of the prior distribution rather than closer to the mean. This can be observed, for example, when $\text{diam}_{\text{clg}} = 0.1$ where the mean of the prior data is 0.4264. We observe that the error level is well beyond 100% which renders the estimate unacceptable. In these circumstances, the PDF is very low, making the MAP estimation almost equivalent to non-Bayesian estimation techniques such as Maximum Likelihood. This is consistent with the results obtained from reflectance in gelatin phantoms, where we observed the same behaviour when the prior distribution is wide. Consequently, we maintain that the results of MAP based estimation are greatly affected by the quality of the prior data used in the estimator.

Finally, we note that the colon model is much more complex and less well characterised than the skin model described in Chapter 4. Consequently, we cannot make any conclusions regarding the accuracy of our method when applied to colon data in comparison with skin reflectance spectra. It would therefore be more meaningful to compare our estimates with those obtained from non-Bayesian estimation techniques such as least-squares or maximum likelihood.

Due to time limitations, however, this could not be achieved within the time frame available. We therefore suggest applying the inversion process described in Algorithm 6.1 to simulated colon reflectance spectra while replacing the MAP-based estimation technique with both ML and LSQ. We would then compare the results of the MAP-based inversion with ML and LSQ results and investigate whether or not the inclusion of prior information offers a significant improvement over classical estimation techniques.

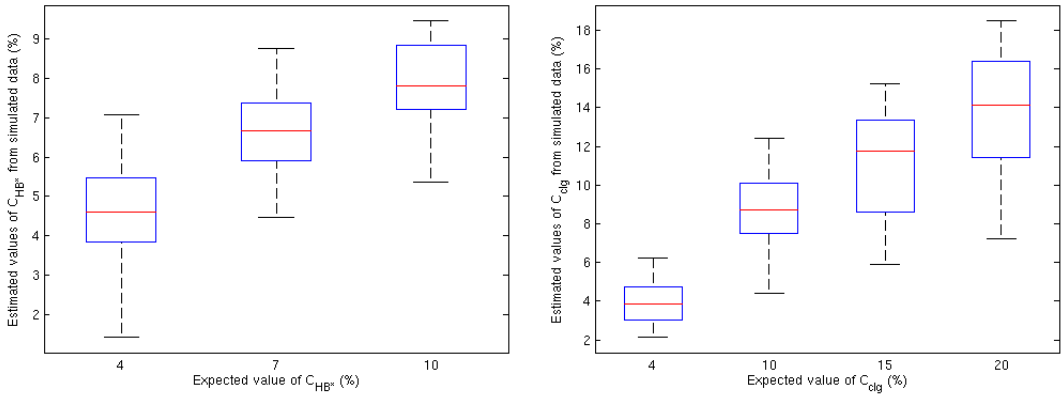

(a) C_{HB*} Estimates (b) C_{clg} Estimates

Figure 6.2: Box plots representing basic statistical information about C_{HB*} (6.2a) and C_{clg} (6.2b) estimates. The estimates are grouped by their respective expected values.

6.6 Multispectral Images of the Colon

We now apply our inversion method to multispectral images of the human colon. All images used in this study were provided by Hidovic-Rowe (Hidovic-Rowe, 2006), and were used as part of her research into the validation of a model of colon reflectance. Note that this section builds on the work previously completed by Hidovic-Rowe and described in details in (Hidovic and Rowe, 2004; Hidovic-Rowe and Claridge, 2005; Hidovic-Rowe, 2006; Hidovic-Rowe et al., 2006). In this section, we describe the imaging setup they used to acquire the colon images and the algorithm they devised to extract reflectance spectra from image values. We then describe how our inversion method was applied to the extracted reflectance and analyse the results.

6.6.1 Modelling the Imaging Setup

For this thesis, we use the colon images acquired by Hidovic-Rowe *et al* in order to test our inversion method. The imaging system used by the authors is described as consisting of *"a Retiga EXi (QImaging, Canada) 12 bit monochrome camera, VariSpec (CRI) liquid crystal tunable filters, and an Integrating Sphere (ProLite, UK) with a Satellite Sphere Illuminator (model SSI-030, Pro-lite, UK)"* (Hidovic-Rowe, 2006). The setup allows the selection of Gaussian-shaped filters of half-width 5-7 nm in the range from 400 to 700 nm.

An integrating sphere was placed between the camera+filter apparatus and the sample as described in Figure 6.3.

The light that originates from the integrating sphere light source is filtered through the VariSpec filter after having interacted with the sample. The camera then collects the light with the desired wavelengths, which in this case were 480, 506, 514, 522, 540, 548, 560, 564, 568, 574, 580, 586, 594, 610, 620, 630, 640, 676, 700. All wavelengths below 450 nm were ignored as the signal-to-noise ratio in this range was low.

The authors used an integrating sphere with a 30 cm diameter where only the illumination port, the sample port and the detector port were left open. All other ports were closed to ensure light would not escape from the sphere. The sample and illumination ports were 2.5 cm in diameter while the detector port had a diameter of 4 cm. The internal wall of the sphere was coated with Spectraflect, a highly reflective form of barium sulphate with a nominal reflectance of $97\% - 98\%$ in the $400 - 700$ nm range.

Hidovic-Rowe used a camera to detect the reflected signal from the sample, and an integrating sphere as a light source. Consequently, calculating the diffuse reflectance of the tissue was more complicated. In fact, the author needed to model the signal detected in each CCD cell as a function of the reflectance of the sample part that was imaged by that particular cell (Hidovic-Rowe et al., 2006). As portions of the light reflected by the sample may be further reflected by the internal sphere walls before being detected by the camera, Hidovic-Rowe used Markov chains to model the imaging setup as described in (Hidovic-Rowe et al., 2006; Hidovic-Rowe, 2006).

A Markov chain is a system that consists of various states where for all possible pairs of states, there exists a fixed probability of the system passing from one state to the other. As described in (Hidovic-Rowe et al., 2006), states in a Markov chain can be either absorbing or non-absorbing, where an absorbing state is a state in which the probability of switching to another state is zero (Hidovic-Rowe et al., 2006; Hidovic-Rowe, 2006). For the purposes of this study, we wish to calculate the reflectance at each point of the tissue

as we accept that the colon is a non-uniform medium where the diffuse reflectance may differ at various points. We also calculate the the reflectance of the whole sample as it represents the mean probability of the light being reflected.

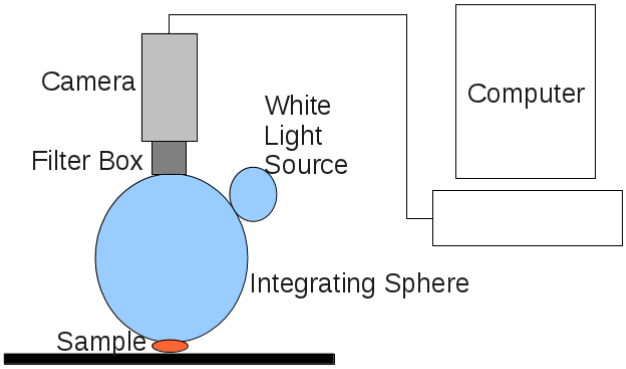

Figure 6.3: Imaging Setup

As described in (Hidovic-Rowe et al., 2006), the imaging system used by Hidovic-Rowe can be modelled as a Markov system that contains the following states:

1. Absorbed by the CCD pixel corresponding to the point of interest.
2. Absorbed by the rest of the camera.
3. Absorbed by the sphere's holes.
4. Absorbed by the sample(excluding the point of interest)
5. Absorbed by the point of interest
6. Absorbed by the sphere walls
7. Reflected by the sample excluding the point of interest
8. Reflected by the sample at the point of interest
9. Reflected by the sphere walls (excluding all ports)

As suggested by the name, the first six stages are absorbing states so a photon that enters any one of these stages cannot enter into another stage (Hidovic-Rowe et al., 2006; Hidovic-Rowe, 2006). Hidovic-Rowe (Hidovic-Rowe et al., 2006) give the transition matrix as:

	1	2	3	4	5	6	7	8	9
1	1	0	0	0	0	0	0	0	0
2	0	1	0	0	0	0	0	0	0
3	0	0	1	0	0	0	0	0	0
4	0	0	0	1	0	0	0	0	0
5	0	0	0	0	1	0	0	0	0
6	0	0	0	0	0	1	0	0	0
7	0	$\frac{c}{1-s}$	$\frac{h}{1-s}$	0	0	$\frac{(1-w)\alpha}{1-s}$	0	0	$\frac{w\alpha}{1-s}$
8	$\frac{c}{1-s}$	0	$\frac{h}{1-s}$	0	0	$\frac{(1-w)\alpha}{1-s}$	0	0	$\frac{w\alpha}{1-s}$
9	0	c	h	$(1-\bar{r})(s-p)$	$(1-r_k)p$	$(1-w)\alpha$	$\bar{r}(s-p)$	$r_k p$	$w\alpha$

Table 6.5: Transition matrix for non-uniform samples

Where d is the area of the detector, s is the area of the sample, h is the area of other holes, w is the reflectance of the sphere walls. Note that the various areas described here are relative areas that were calculated in reference to the total area of the integrating sphere walls (Hidovic-Rowe, 2006; Hidovic-Rowe et al., 2006). Additionally, p represents the size of the point of interest, c is the size of the camera aperture, $\alpha = 1 - (s + c + h)$ is the area of sphere walls excluding all holes, r_k is the reflectance at the point of interest and $\bar{r}$ is the mean reflectance of the sample (Hidovic-Rowe, 2006).

As stated in (Hidovic-Rowe et al., 2006), the amount of light detected by cell k of the CCD (m_k) can be expressed as a function of mean and local reflectance. Equations (6.3), (6.4) and (6.5) describe the amount of light collected by the k^{th} cell, the sample mean reflectance $\bar{r}$ and the local reflectance r_k respectively. Further details about the Markov model and how these equations were constructed are available in (Hidovic-Rowe, 2006; Hidovic-Rowe et al., 2006).

$$m_k = \frac{c\, r_k\, p\, w}{(1-s)(1-w\,\alpha) - r_k\, p\, w\, \alpha - \bar{r}\, w\, \alpha\, (s-p)} \tag{6.3}$$

$$r_k = A_k[(1-s)(1-w\,\alpha) - \bar{r} w\, \alpha\, (s-p)] \tag{6.4}$$

$$\bar{r} = \frac{(1-s)(1-w\,\alpha)\sum_{k=1}^{N} A_k}{N + w\,\alpha\,(s-p)\sum_{k=1}^{N} A_k} \qquad \text{where} \qquad A_k = \frac{m_k}{p\, w\, (c + m_k\, \alpha)} \tag{6.5}$$

We use the same model parameters used in (Hidovic-Rowe, 2006), namely: $w = 97\%$, $p = 1.7941\text{e}-7$, $s = 0.0017$, $c = 0.0011$ and $h = 0.0051$. As done in (Hidovic-Rowe, 2006), the images are also corrected for gain and exposure using Equation (6.6)

$$image_{corrected} = \frac{image_{original} - offset}{gain * exposure} \tag{6.6}$$

Hidovic-Rowe also used a scaling factor that converts the signal recorded by the CCD camera into a number representing the fraction of collected photons. The factor was calculated using a 50% reflectance standard as its reflectance is well documented by the manufacturer. This is necessary as the conversion factor relates image values to the signal modelled by the Markov system m which requires the prior knowledge of the tissue's reflectance. Consequently, we set $c_{50} = \frac{image_{50}}{modelled_{50}}$. This is then used to convert corrected image values to reflectance signal and vice versa (Hidovic-Rowe, 2006).

Figure 6.4 depicts a map constructed from reflectance values at wavelength 574 nm at each point in the sample images. These reflectance maps are constructed for each sample type (cancer, normal and transitional tissue) at various wavelengths between 480 and 700 nm. These maps are then used in the inversion process to extract the values of the unknown optical parameters vector $\boldsymbol{\theta}$.

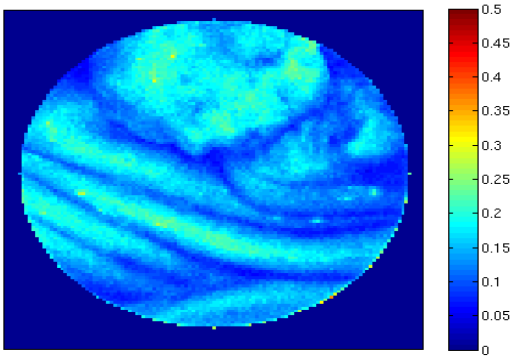

(a) Cancerous Sample

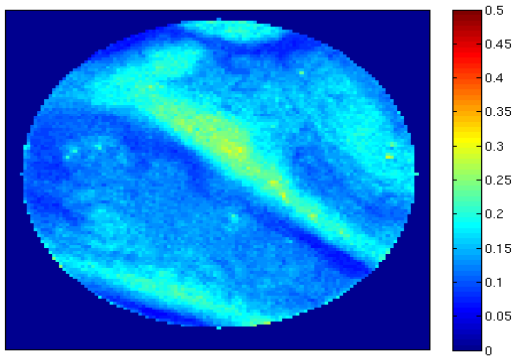

(b) Transitional Tissue Sample

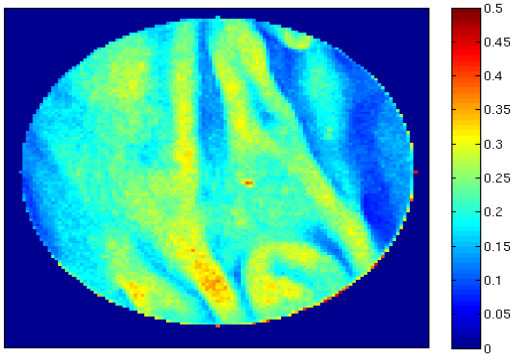

(c) Normal Sample

Figure 6.4: Reflectance values at wavelength 574 nm. These maps represent the reflectance values at every point in the sample images. The image cubes of the three samples were first constructed by aligning all sample images with 50% reflectance standard images. The images are then corrected for different gains and exposure times before the conversion factor c_{50} described above is applied to the resulting multispectral cube. A mask is applied to all images to only keep the reflectance spectra from the colon tissue which is why the area around the central circles appears in these figures as having a 0 reflectance. Equations (6.4) and (6.5) are then applied to generate these maps

6.6.2 The Inversion Algorithm

As described in Section 6.4, tumours in the colon can be characterized by changes in the blood volume fraction, scatterer density, scatterer size and thickness of the mucosa. We thus take these parameters to be of most significance when studying the physiology of the colon and decide whether it is normal or not. Consequently, we aim to recover these parameters from multispectral images of the colon, making our unknown variable $\boldsymbol{\theta} = (\mathrm{C}_{\mathrm{HB}*}, \mathrm{diam}_{\mathrm{clg}}, \mathrm{C}_{\mathrm{clg}}, d)^{\mathrm{T}}$.

To that aim, we construct multispectral cubes from the colon images we acquired from Hidovic-Rowe. The images were taken *ex vivo* of three tissue sites: normal, cancerous and transitional tissue right next to the tumour. The sample were categorised as normal, cancerous and transitional following a histological analysis at the Department of Pathology at the University of Birmingham. This categorisation was then used as the ground-truth against which our results are compared. All images provided by Hidovic-Rowe were taken using the same imaging setup and from the same patient in order to ensure that any differences in the recovered parameters were due to differences in tissue structures rather than inter-subject variability.

We first use the MathWorks Image Processing toolbox to align all colon images with those taken of the 50% reflectance standard. This is necessary for applying the conversion factor mentioned in Section 6.6.1 and which allows us to convert the image values we used to a signal that can be converted to reflectance spectra. We then recover the sample mean reflectance as well as the local reflectance spectra at the area of interest from the spectral cube using equations (6.4) and (6.5).

Ideally, the estimation should be done at every point on the surface, in order to gather a complete representation of the distributions of parameters in the tissue. However, recovering $\boldsymbol{\theta}$ at every point is an extensively time consuming process. In fact, constructing a full parametric map of a single sample would require recovering $\boldsymbol{\theta}$ at 9503 points, with the recovery process at each point lasting for between $3-4$ hours on an average personal computer. This is because recovering $\boldsymbol{\theta}$ at a single point requires $100-400$ iterations as part of the optimisation process.

In each iteration, MCML is used to evaluate the reflectance spectra, which takes a number of minutes to complete. Due to limitations in the currently available computing resources, we opt to do the recovery at a limited number of points. Consequently, we apply the inversion process to 30 points from each cube, as well as on the sample mean reflectance $\bar{r}$.

As described in Section 6.5, the inversion algorithm we use aims to minimise the objective function described by Equation (6.2). As in Section 6.5, we use the MATLAB function LSQNONLIN function with the Levenberg-Marquardt algorithm to minimise the objective function. We use the data in the first column of Table 6.1 as the prior information required for our algorithm. Our inversion method also involves the use of a forward model.

In (Hidovic-Rowe and Claridge, 2005), Hidovic-Rowe demonstrated that the MCML method described in Section 2.4.3 can be used to generate reflectance spectra of the colon. However, our inversion method requires a large number of function evaluations as part of the minimisation process. Each evaluation is essentially a run of the MCML program which takes several minutes to complete. This makes the inversion a very computationally expensive process, and thus, a direct inversion using MCML as a forward model highly inefficient.

As an alternative, we considered using the Kubelka-Munk method as a forward modelling technique as it is much faster than the MCML based model. However, the results of modelling reflectance using the Kubelka-Munk and MCML methods are very different as depicted in Figure 6.5. We therefore decide not to use the Kubelka-Munk based model as it was not validated and its results vary significantly from the MCML based model. Instead, we use the error correction method described in (Hidovic and Rowe, 2004) which combines the speed of the Kubelka-Munk method and the accuracy of MCML. This algorithm is summarised in Appendix B.

In conclusion, the process of applying our inversion algorithm to multispectral images of the colon can be summarised as follows:

1. Construct multispectral image cubes of three colon samples (normal, cancerous and cancer surrounding tissue).

2. Extract the mean reflectance and local reflectance spectra at 30 different points on each sample using equations (6.3), (6.4) and (6.5). For each of these points, apply the steps below for 20 iterations.

(a) Set $S = K$ Where K evaluates the reflectance spectra using the Kubelka-Munk method.

(b) Estimate $\boldsymbol{\theta}_t$ using Equation (4.15) where R is substituted by S.

(c) Evaluate $F(\hat{\boldsymbol{\theta}}_t) = M(\hat{\boldsymbol{\theta}}_t) - S(\hat{\boldsymbol{\theta}}_t)$ where M evaluates the reflectance spectra using MCML.

(d) Evaluate A and B as described in Appendix B

(e) Set $S = K + F(\boldsymbol{\theta}_t)$ and repeat steps (b) – (e)

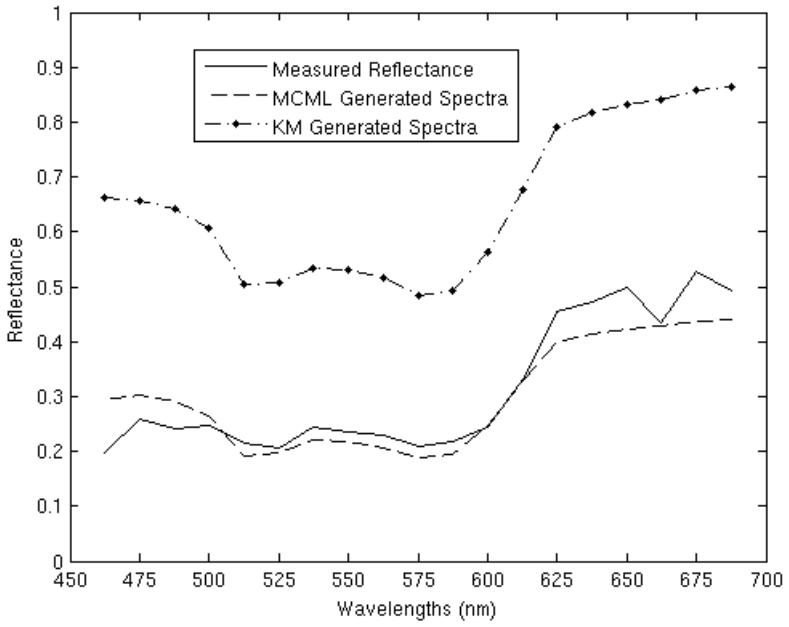

Figure 6.5: Measured vs. reconstructed reflectance spectra using $\boldsymbol{\theta} = (0.049, 0.38, 0.13, 0.049)^{\mathrm{T}}$. This parameter vector was estimated by our inversion method using the MCML based technique as a forward model. The reflectance spectra is reconstructed using two methods based on Kubelka-Munk and MCML respectively. Both methods use exactly the same input parameters and model the tissue as described in Section 6.3. We note that the MCML generated spectra is much closer to the measured reflectance than the Kubelka-Munk based reflectance. However, we also observe that there might be a varying offset between Kubelka-Munk reflectance and the measured spectra. This is discussed further in Chapter 7.

6.6.3 Results and Discussion

As described earlier, we aim to recover the blood volume fraction, diameters of scattering particles, scatterer density and thickness of the mucosal layer from multispectral images

of the colon. We first construct multispectral cubes from colon images taken of three distinct samples: A sample from a normal, cancerous and transitional tissues from the same subject. The samples were imaged *ex vivo* using the setup described in Section 6.6. We then extract reflectance spectra at each point on the cube's surface as described in Section 6.6.1. Finally, we apply our inversion method to individual reflectance spectra and analyse the results. Due to limitations in the currently available computing resources, we opted to recover the unknown parameter $\boldsymbol{\theta}$ at 30 distinct points on each sample as depicted by Figure 6.6.

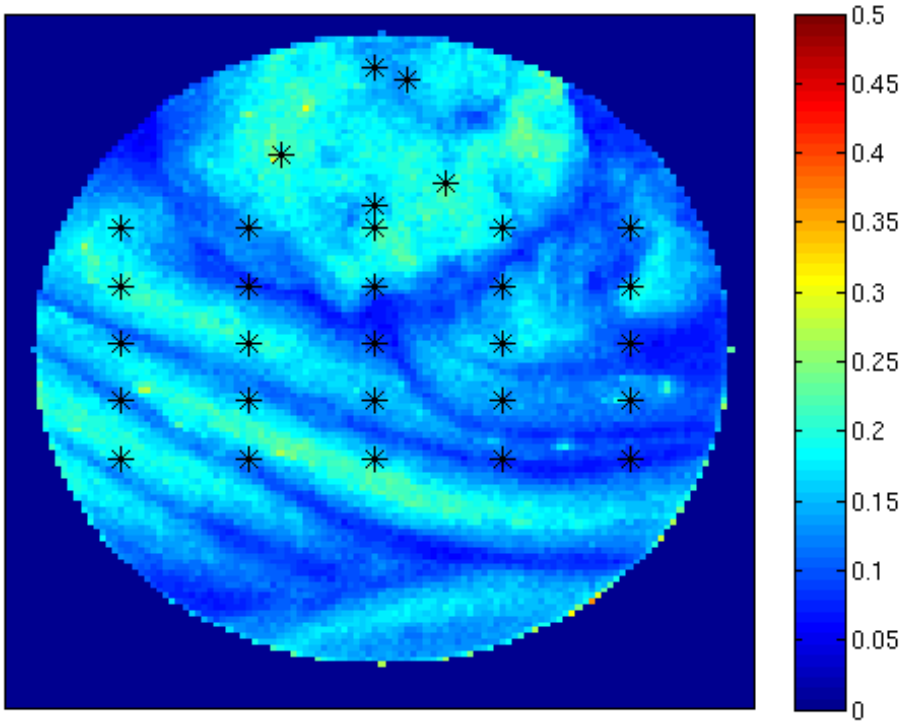

Figure 6.6: Image of the cancer tissue sample taken at wavelength 574 nm. The dots that appear on the image represent the points at which the inversion algorithm was applied. Note that not many points lie on what appears to be the largest abnormality in this tissue. In addition, the points are not spread equally over the whole sample.

As we recover the unknown parameter $\boldsymbol{\theta}$ from real measurements, we cannot verify the accuracy of our inversion method in the same manner that we used with simulated

data. This is due to the fact that we do not know exactly what the value of $\boldsymbol{\theta}$ should be. Consequently, we do not aim to verify that the estimation results are accurate by comparing them against ground-truth values. Rather, we first ensure that the estimated values are within the allowed ranges described in Table 6.1. We then analyse the recovered values of $\boldsymbol{\theta}$ in order to differentiate the normal from abnormal tissue samples.

As a result of our inversion method, we obtain a total of 90 estimates of $\boldsymbol{\theta}$, 30 for each sample. Table 6.6 shows some basic statistics obtained from analysing the three sets of data points corresponding to the three samples. Based on a visual analysis of the results, we observe that with the exception of mucosal thickness, the mean values gathered from cancerous and transitional tissue samples are quite similar, and differ from the parameters describing the normal sample. This, however, is not sufficient to claim, with any certainty, that we can safely differentiate between the normal and abnormal samples. We therefore apply a number of statistical tests in order to evaluate the significance of the differences observed.

Sample	Parameter	Mean	Standard Deviation	Min	Max
Cancer	C_{HB*}	0.0381	0.0169 (44.5%)	0.00	0.0663
	$diam_{clg}$ (μm)	0.6379	0.1706 (26.7%)	0.0583	0.7399
	C_{clg}	0.0833	0.0316 (38%)	0.0183	0.1300
	d (cm)	0.0482	6.375 e-4 (1.32%)	0.0473	0.0497
Normal	C_{HB*}	0.0447	0.0114 (25.6%)	0.0238	0.0763
	$diam_{clg}$ (μm)	0.4636	0.1592 (34.3%)	0.1800	0.7399
	C_{clg}	0.1105	0.0296 (26.8%)	0.0240	0.1354
	d (cm)	0.0488	7.908 e-4 (1.6%)	0.0472	0.0506
Transitional	C_{HB*}	0.0372	0.010 (26.9%)	0.0106	0.0494
	$diam_{clg}$ (μm)	0.6864	0.0697 (10.2%)	0.5121	0.7397
	C_{clg}	0.0891	0.0312 (35%)	0.0291	0.1363
	d (cm)	0.0480	3.955 e-4 (0.8%)	0.0473	0.0490

Table 6.6: Table summarising basic statistical information about the three samples used in the estimation process. We used 30 data points from each sample to generate the statistics summarised in this table.

We also note that all recovered parameters, including those obtained from the cancerous sample, had values within the acceptable ranges described in 6.1. However, this does not mean that the recovery process yielded incorrect results. In fact, the ranges in Table 6.1 are intentionally wide in order to accommodate for inter-subject variabilities. Consequently, we cannot expect the parameters recovered from cancerous tissue to necessarily fall outside these ranges. However, we can aim to differentiate between normal and abnormal tissue samples taken from the same patient as is the case with the colon images used in our analysis. We therefore aim to differentiate between the three tissue samples: normal colon sample, cancerous colon sample, and transitional tissue.

Figure 6.7 represents a box plot[‡] of our estimates grouped by tissue type with each group containing 30 data points. We observe that with the exception of blood volume fraction, the mean values of all other parameters are very close in cancerous and transitional tissue, but different for the normal samples. This suggests that we can use these results to differentiate normal and abnormal samples. However, we can use statistical methods to decide whether the difference is indeed statistically significant or not.

We use the Kruskal-Wallis test to examine whether the observations taken from the three samples have similar distributions or whether these groups are significantly different. The Kruskal-Wallis test is a version of the classical one-way ANOVA. It works by comparing the medians of the analysed data groups to determine whether or not the samples come from the same population or different populations with the same distribution (Corder and Foreman, 2009). Note that this test is not meant to tell which sample is significantly different from the others. Rather, it is used to tell whether at least two groups are significantly different.

To that aim, we use the MATLAB function KRUSKALWALLIS[§], a part of the MathWorks Statistics Toolbox, to complete the Kruskal-Wallis test. This function returns the p value for the hypothesis that the data comes from the same distribution, as well as an

[‡]BOXPLOT, http://www.mathworks.co.uk/help/stats/boxplot.html
[§]KRUSKALWALLIS, http://www.mathworks.co.uk/help/stats/kruskalwallis.html

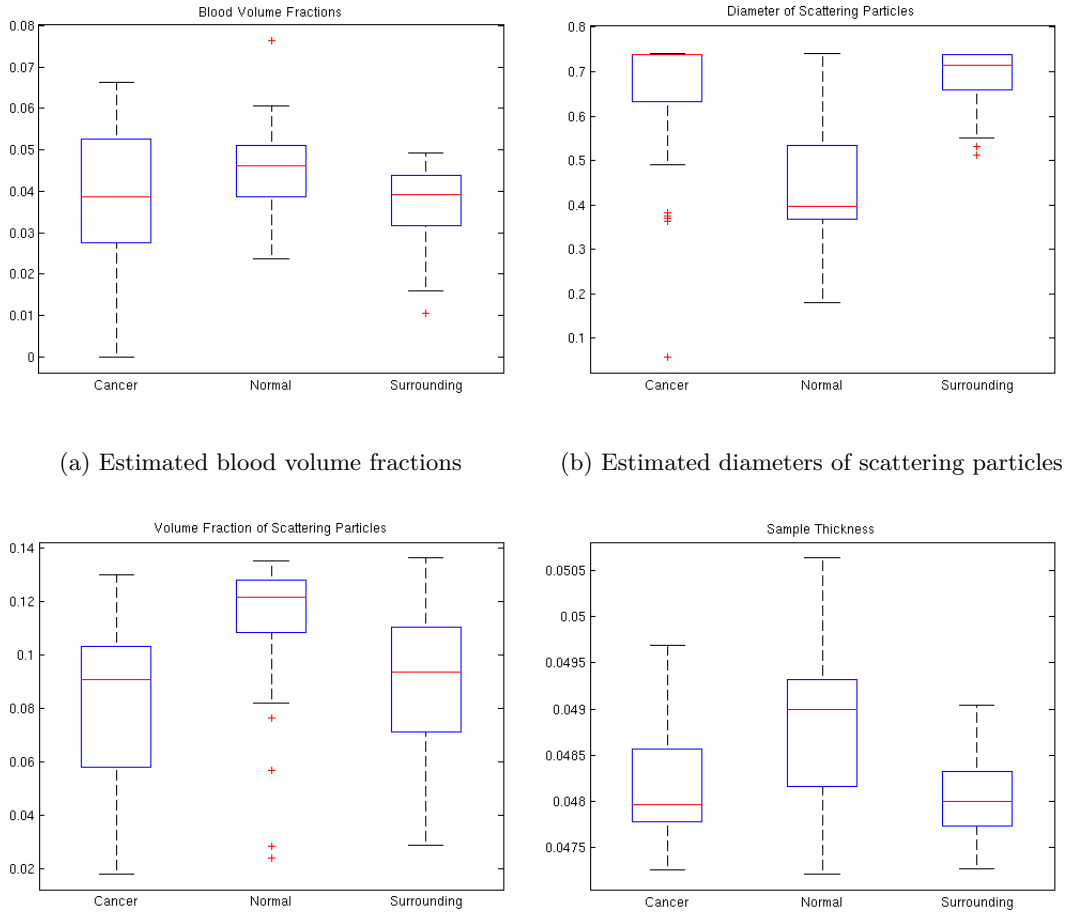

(a) Estimated blood volume fractions

(b) Estimated diameters of scattering particles

(c) Estimated volume fractions of scattering particles

(d) Estimated sample thicknesses

Figure 6.7: Box plots representing a basic statistical analysis of the recovered parameters in all three samples. The data is grouped by tissue type, and each box represents 30 data points. On each box, the central mark is the median, the edges of the box are the 25th and 75th percentiles, the whiskers extend to the most extreme data points not considered outliers, and the red (+) marks represent outliers. The plots indicate that the means recovered from cancerous and transitional tissue samples are different from those obtained from the normal sample. We apply further statistical analysis to establish whether this difference is statistically significant.

ANOVA table and a box plot. The significance level used by the function is 0.01, which indicates that the probability of wrongly rejecting the null hypothesis is 1%. This means that recording a value p that is lower than the significance level 0.01 allows us to doubt the hypothesis that all observations come from a distribution with the same mean.

We also apply the Kruskal-Wallis for individual parameters rather than for the complete unknown parameter $\boldsymbol{\theta}$. As a result, we record p values of 0.051, 5.370 e-6, 0.0007 and 0.0003

for blood volume fraction, diameter of scattering particles, scatterer volume fraction and thickness respectively.

We note that $p < 0.05$ for all parameters but for the blood volume fraction, which is in accordance with the findings recorded in Figure 6.7. This suggests that we can differentiate between the three samples in terms of all properties but the blood volume fraction. This is not consistent with the histological changes reported in Section 6.4 which suggests that a change in the blood volume fraction is often reported in cancerous tissue. These results are further confirmed by conducting the same test but on individual pairs rather than on the triple of all three samples. The results are summarised in Table 6.7.

Pair	$p(\mathrm{C}_{\mathrm{HB}*})$	$p(\mathrm{diam}_{\mathrm{clg}})$	$p(\mathrm{C}_{\mathrm{clg}})$	$p(d)$
Normal vs. Cancer	0.2089	1.95e-4	3.66 e-4	0.0033
Normal vs. Transitional Tissue	0.0071	1.73 e-6	0.0039	9.49 e-5
Cancer vs. Transitional Tissue	0.5742	0.5249	0.4871	0.7562

Table 6.7: Summary of Kruskal-Wallis test results conducted for individual parameters on each pair of tissue samples

These results indicate that the normal and transitional tissue samples are significantly different in terms of all parameters. It also indicate that we cannot accurately differentiate between cancer and transitional tissue samples. However, we also observe that the cancer and normal samples can not be differentiated in terms of blood volume fraction alone. This result is interesting as it suggests that differentiation might be more accurate if performed in terms of a combination of parameters rather than single ones.

Consequently, analysing the statistical difference between samples in terms of a change in a single parameter rather than the change in $\boldsymbol{\theta}$ may not correctly reflect the differences between three samples. Consequently, we analyse the statistical difference between the samples in terms of the vector $\boldsymbol{\theta}$. To that aim, we use K-mean clustering to separate

the estimates into clusters matching the three samples used. This is performed in MATLAB, where all estimates are gathered as a single set of data, and the clustering function KMEANS is applied to the full set of observations.

We initially aim to separate the results into three groups matching our three samples. However, we note that this results in the estimates from cancerous and transitional samples being grouped in the same cluster. Consequently, we run the clustering again with the goal of having two clusters matching normal and abnormal tissues with the abnormal group containing both cancerous and transitional samples. The results are summarised in Figure 6.8 which shows a clear distinction between the two clusters.

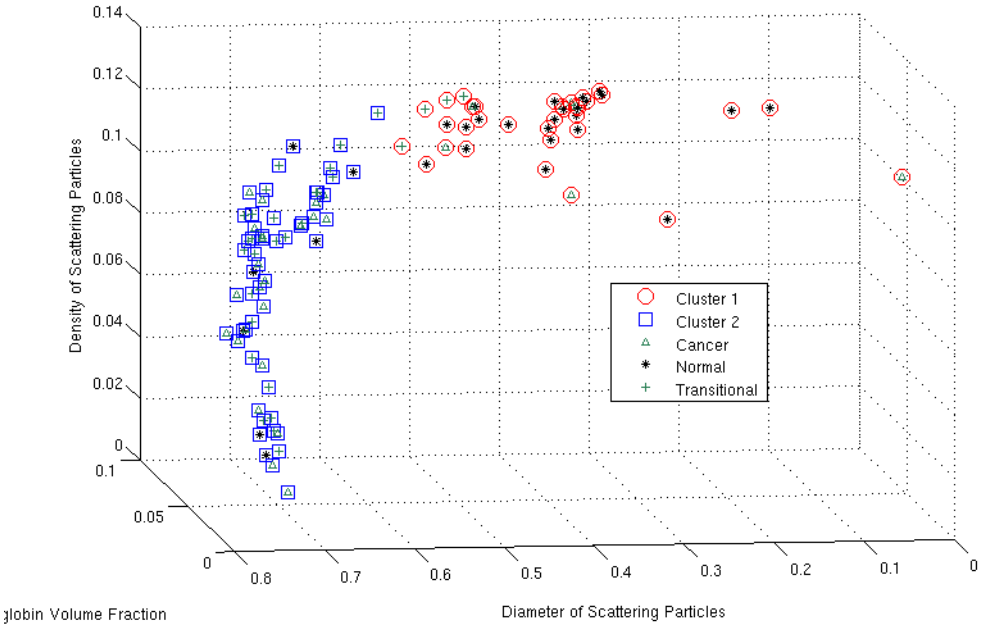

Figure 6.8: Result of K-Mean clustering applied to the set of observations from all samples. Note that most cancer and transitional tissue estimates fall within the same cluster (Cluster1) while normal tissue estimates are part of a different cluster (Cluster1). We also notice that there were estimates that were incorrectly classified.

An initial analysis of the results indicates that 87% of points recovered from transitional tissue and 77% of those estimated from cancer samples fall within the same cluster (Cluster 1) while 77% of estimates recovered from the normal sample fall within the second cluster.

This is consistent with the expected behaviour where the structure of a normal colon should differ from cancerous tissue or a tissue that has undergone significant changes. However, we also note the presence of estimates that were incorrectly classified as depicted in Figure 6.8 by the presence of normal observations ($*$) within Cluster 2 ($\square$), and cancer and transitional tissue observations ($\triangle$, $+$) within Cluster 1 ($\bigcirc$).

We complete further analysis of the results to verify whether the classification we employed was reliable. To that aim, we conduct a basic receiver operating characteristics (ROC) analysis on the results of our clustering operation. We focus on the classification of estimates as being part of the abnormal tissue cluster. We use equations (6.7), (6.8), (6.9), (6.10), (6.11) to calculate common performance metrics that can be used to evaluate our clustering operation as described in (Fawcett, 2006).

$$FP_{rate} = \frac{FP}{N} \tag{6.7}$$

$$TP_{rate} = \frac{TP}{P} \tag{6.8}$$

$$precision = \frac{TP}{TP + FP} \tag{6.9}$$

$$recall = \frac{TP}{P} \tag{6.10}$$

$$accuracy = \frac{TP + TN}{P + N} \tag{6.11}$$

Let cluster A be the cluster describing the observations recovered from cancerous and transitional tissue samples. We take TP to be the number of observations correctly classified as belonging to A, FP to be the number of observations incorrectly classified as members of A, TN to be the number of observations correctly classified as not belonging to A and FN to be the number of observations incorrectly classified as not belonging to A. We also take $P = TP + FN$ and $N = FP + TN$ be the total numbers of positives and negatives respectively.

The results of the ROC analysis indicate a true positive rate of 81.67% and a false positive rate of 23.33%. We also note an accuracy rate of 80% and a precision of 87.5%. The

results are positive, and indicate that we can differentiate between normal and abnormal tissue samples based on the recovered parameter vector $\boldsymbol{\theta}$. However, these results should be taken with caution for a number of reasons. Firstly, the number of points used in the statistical analysis is quite small compared with the number of observations that can be made from each samples.

In fact, the analysis was performed on only 90 observations (30 points from each sample) which may not be enough to draw conclusions about the significant differences between the full samples. Though this was done due to limited computational resources, it may have an effect of the results of our analysis. Secondly, the points used in the analysis were spread around the samples rather than focused on specific areas of interest as depicted by Figure 6.6. However, they are not equally distributed around the sample.

6.7 Conclusion

In this chapter, we briefly described the forward model we used as part of our inversion process. We then outlined how our MAP-based inversion method was applied to simulated data representing colon reflectance spectra. Finally, we applied our inversion method to multispectral images of the colon that were obtained from Hidovic-Rowe as part of the work they completed in (Hidovic-Rowe, 2006).

As stated earlier in this chapter, the inversion method was first applied to simulated reflectance spectra. The aim was then to evaluate the accuracy of our inversion method by comparing the estimates with ground truth values. This process indicated that our method could recover the unknown parameter $\boldsymbol{\theta}$ from reflectance spectra with an error level ranging on average between 7 and 40%. We also noted that the inversion method returned better results when the expected value was nearer to the mean of the prior data, and when the prior distribution had a small standard deviation. This confirms the findings described in Section 5.3.1 which indicated that our method is greatly affected by the prior data used.

We then applied the inversion method to reflectance data extracted from multispectral images of the colon. In this instance, we could not compare the estimates with ground-truth values as those were not available. However, we used the possibility of differentiating normal from abnormal tissues based on the estimates as a way to evaluate our inversion method. We noted that based on the samples used, we could classify the estimates into two categories: normal and abnormal clusters with the abnormal group containing estimates recovered from both the cancerous and transitional tissues samples.

However, we note that when using multispectral colon images, the inversion was conducted on a limited number of samples that were all taken from the same patient. The results described in this chapter indicate that this method has the potential of supporting the diagnosis of abnormalities in human cancer. This is especially true considering that the differentiation and changes reported by the inversion method are consistent with histological changes in the colon tissues reported in the literature. However, we note the use of *ex-vivo* tissues only, and the limited number of points on which the statistical analysis of the results was conducted. These factors render our analysis insufficient to categorically demonstrate that our inversion method could be used to distinguish between normal from abnormal tissue samples.

Ideally, this method should be tested on a larger number of samples, from different patients, and on tissue samples that have undergone various changes, rather than just focusing on adenocarcinomas. We also propose that the method be always applied to differentiate samples taken from the same patient only, i.e. the classification of a tissue as being abnormal should be based on it being compared with a normal sample from the same patient only. This would have two main benefits.

Firstly, this can help ensure that any significant differences between the tissue samples are due to changes in the structure of the tissue, rather than inter-subject variabilities. This is because a parameter value that is considered normal in one patient, may be considered abnormal in another. Secondly, if one recovers the optical properties of a normal tissue sample from a patient, this information can be used as prior data for the inversion

process when applied to the abnormal area of the colon. This would allow us to tailor the inversion process on a per-patient basis, making the prior distribution relevant to each patient separately. This would therefore result in a narrow distribution of the prior data, and should, in effect, improve the results of the estimation process when conducted on an abnormal tissue area. This would also help in the tissue classification efforts as the range of normal values for a given person would be much narrower than a range accounting for inter-subject variabilities.

Chapter 7

Conclusions and Future Work

7.1 Summary of Work Presented

We proposed a Bayesian based inversion method that estimates a number of optical properties parameterising a biological tissue even if some of its underlying physical attributes are uncertain. This method had two main objectives:

1. To retrieve the optical properties of a biological tissue from reflectance or transmittance measurements.

2. To succeed in retrieving the aforementioned values even when the physical attributes of the said tissue are uncertain.

The maximum *a posteriori* estimator was first applied to simulated skin reflectance spectra. The optical properties of interest in that case were the concentrations of chromophores present in the skin, namely melanin and haemoglobin. We generated reflectance spectra using a skin model based on the works described in (Cotton et al., 1997; Matcher, 2001; Meglinski and Matcher, 2003). Gaussian noise was then added to the simulated spectra, and uncertainty was introduced in the inversion method by setting the thickness of the sample to a distribution mean rather than the actual value of the parameter.

To evaluate our estimator, we compared its results with estimates obtained from two widely used techniques: maximum likelihood and least-squares methods. The results obtained from simulated data were very promising as they indicated that MAP-based estimates were more accurate than their ML and LSQ-based counterparts in most instances.

The estimation method was also applied to a number of non-scattering gelatin samples that were constructed in order to test the method on measured rather than simulated data. In this instance, we collected the transmitted light and applied the inversion method on the measured spectra. We also applied our inversion method to scattering gelatin phantoms where we introduced scattering events by adding milk to our gel. We then collected reflectance spectra and compared the results of our estimation technique with LSQ based estimates.

When using simulated spectra and non-scattering phantoms, we demonstrated that the use of a Bayesian-based method to recover the optical properties of tissues can lead to a substantial increase in the accuracy of the recovery process. We have established that even in the presence of some level of uncertainty in the underlying tissue model, the MAP-based estimator provides accurate results. This is potentially important when applied to tissue samples whose physical characteristics are not described with high precision. However, we also noted that the quality of the prior data used in the estimation process can have a significant effect on the accuracy of the results. In fact, we observed that using a prior data set with a wide distribution shows little improvement over other estimator methods such as maximum likelihood. This was particularly notable when the expected value of the unknown parameter falls on the tail of the prior distribution rather than closer to the mean.

Furthermore, we observed that the results of the estimation process when applied to scattering gelatin phantoms were less accurate than those collected from simulated data and non scattering phantoms. This was attributed to the inaccuracy of the forward model itself, rather than the estimation method, the prior information used or the uncertainty level of the known physical properties used in the model. In fact, we demonstrated that the effects of model mismatch cannot be attenuated by our estimation method regardless of the quality of the prior data. We thus concluded that more work needed to be done to validate the forward model describing such phantoms. Due to time limitations, we decided to concentrate our time and efforts to test our method on measurements obtained from human tissue samples whose forward model has already been validated, namely the colon.

To that aim, the MAP-based estimator was applied to multispectral images of the human colon. This was performed on three samples: normal colon tissue, cancerous colon and transitional tissue surrounding the tumour. The original aim was to extract reflectance spectra from every point on the image, and recover the values of parameters of interest from each spectra. Consequently, this would allow us to recover the values of our optical parameters at each point on the image. However, we were unable to complete that for all three samples due to time limitations. We thus opted to apply the inversion method to a limited set of points within the images.

The multispectral images were therefore used to extract reflectance spectra at every point on the image. Thirty spectra from each sample were then used to estimate the optical parameters of interest, namely: blood volume fraction, density and size of scattering particles and thickness of the mucosa. A statistical analysis of the results was then performed in order to decide whether the samples were statistically different or not. We noted that we could not, with any certainty, distinguish between the cancerous and transitional tissue samples based on the recovered parameters. However, we could clearly differentiate between normal and abnormal tissue types even using only a small data set. Note that both cancerous and transitional tissues were grouped together in the "abnormal" category. The observed differences were statistically significant, and consistent with the fact that the structure of a normal colon differs from cancerous tissue or its surrounding transitional colon.

These findings are important as they indicate that our inversion method could potentially be more accurate than its classical counterparts in recovering the optical parameters of a biological tissue. This, in turn, could be of great importance in diagnosing abnormalities in said tissue. The following section describes improvements that could be implemented and used to overcome some of the limitations of this work.

7.2 Future Work

A number of limitations were noted in the previous chapters, namely, the limited number of samples that were used as part of the inversion process and the time required for the estimation process. The following sections describe possible steps that could be used to resolve these limitations.

Larger Experimental Study

When applied to colon images, we noted three main limitations. Firstly, all images were taken *ex vivo*. This can lead to inaccurate results if the sample undergoes important changes due to loss of blood. These changes should therefore be reflected in the forward model of the colon. Alternatively, the inversion method should be applied to *in vivo* images whenever these are available. This would ensure that any parameter values deemed abnormal are not due to changes resulting from tissue extraction.

In addition, only a small number of data points from three samples was used in the inversion process. The results obtained from using these three samples suggest that our inversion method could be used to differentiate normal and abnormal tissue areas. This was based on the statistical analysis conducted on all estimates, namely: 144 data points. However, we would require a larger number of data points in order to make systematic conclusions about the performance of our method. For instance, we believe that the usage of a larger number of estimates from points randomly located on the tissue surface would help ensure that the observations are representative of a wider spectrum of tissues.

Finally, we only differentiated between normal, transitional and adenocarcinoma ridden samples where the histological changes are expected to be relatively large. Our MAP-based inversion method should also be tested on tissues with other abnormalities, that may present with a smaller number of histological changes such as benign epithelial polyps. Consequently, the inversion method should ideally be tested on a larger number of samples, from different patients and with various abnormalities in order to objectively evaluate its capabilities and limitations.

Validating the Transmittance Model of the Gelatin Phantoms

We previously noted that our MAP based estimation was applied to a number of gelatin phantoms. Only a small number of phantoms were prepared, and an even smaller number was designed to exhibit light scattering properties. Furthermore, the absorption coefficients of food dyes and gelatin used in these phantoms may have included a large level of error. This was due to the lack of any information about the optical properties of the food dyes used in the experimental process, and the limited availability of resources that would allow us to safely validate the recovered values. In addition, applying our inversion method to such a small number of samples greatly affects the possibility of accurately verifying the performance of our estimator. In fact, the use of such a small number of estimates reduces the credibility of any statistical analysis of the results.

Consequently, we suggest the use of different absorbers to prepare the phantoms. In particular, the use of absorbers with well documented optical properties such as blood, methylene blue or indocyanine green would be highly beneficial as their properties are well documented in the literature. If food dyes are to be used, a more structured analysis of their absorption coefficients has to be completed before being used in the forward model. The forward model describing light transfer in the gelatin phantoms should also be carefully validated against measurements to ensure that the estimation process is not affected by incorrect assumption.

Speeding Up the Inversion Process

One of the main challenges encountered during the application of our inversion process was the time required to recover the parameters of interest from a single spectrum. This is particularly relevant when the Monte-Carlo method is used as part of the forward modelling phase. As stated earlier, A Monte-Carlo based forward model is often the most accurate mean of modelling light transfer in a multi-layered medium. However, a single run of the MCML software requires a few minutes, depending on the number of wavelengths and photons used. Consequently, the parameter recovery process can be very computationally expensive as demonstrated in the Chapter 6.

There exist a number of possible solutions to overcome this limitation such as the use of high performance clusters, GPUs and the error correction algorithm described in (Hidovic and Rowe, 2004). As part of our research, we only investigated the use of one of these methods, namely, the error correction algorithm designed by Hidovic-Rowe. However, we observed that the time improvements that this method brought was insufficient for our inversion method to be used in real-time. The effects of using this method could be further enhanced by reducing the time required for each evaluation of the forward model. This can be achieved by making use of new advances in GPU computing (MCX (Fang and Boas, 2013)) and high performance clusters for example.

Another option would be to use a simple forward model, such as Kubelka-Munk, and estimate the mismatch between it and the measured data as part of the inversion process. In Chapter 6, we noted that when modelling light travel in the human colon, the reflectance spectra reconstructed using Kubelka-Munk showed a noticeable offset from the measured spectra. The offset varied depending on the values of $\boldsymbol{\theta}$ used for data reconstruction and could therefore not be be directly corrected for. However, we believe that further investigation into this offset and how it can be included in the forward model as another parameter would allow us to speed up the estimation process. This would be achieved through removing the need for a more accurate, but also more computationally expensive method such as MCML, without compromising the accuracy of our estimation.

In conclusion, we advance that although further work needs to be completed before it can be used in real-time, this inversion method shows great promise in its potential to accurately recover the optical properties of a tissue when some of its parameters are not accurately known. In addition, this method could also be used as part of classification efforts aiming to differentiate normal from abnormal tissues. Furthermore, we observed that our method could be applied to any type of biological medium as long as we are able to construct a forward model of light transport in that tissue. We thus suggest that this work could be extended to assist diagnosticians in the early, non-invasive detection of various tissue abnormalities if the limitations described above are addressed.

Appendix A

Estimation Results from Simulated Reflectance Spectra

This table summarises the results of the estimation process conducted on simulated reflectance spectra of the human colon. We first use the forward model summarised in Section 6.3 to generate the reflectance spectra using various values of $\boldsymbol{\theta} = (\mathrm{C}_{\mathrm{HB}*}, \mathrm{diam}_{\mathrm{clg}}, \mathrm{C}_{\mathrm{clg}}, d)^{\mathrm{T}}$. We then apply the inversion method to the generated data. This process is summarised in Algorithm 6.1.

$\mathrm{C}_{\mathrm{HB}*}$	$\hat{\mathrm{C}}_{\mathrm{HB}*}$	$\mathrm{diam}_{\mathrm{clg}}$	$\hat{\mathrm{diam}}_{\mathrm{clg}}$	$\mathrm{C}_{\mathrm{clg}}$	$\hat{\mathrm{C}}_{\mathrm{clg}}$	d	$\hat{d}$
4.0	2.6197	0.1000	0.5459	4.0	2.5184	0.0395	0.0325
4.0	2.9768	0.1000	0.5277	10.0	8.1986	0.0395	0.0186
4.0	1.4453	0.1000	0.5500	15.0	5.9279	0.0395	0.0351
4.0	3.1518	0.1000	0.3623	20.0	8.2901	0.0395	0.0332
4.0	6.8433	0.1000	0.4365	4.0	4.8760	0.0595	0.0203
4.0	5.6960	0.1000	0.3500	10.0	7.9459	0.0595	0.0270
4.0	4.4565	0.1000	0.3697	15.0	8.5137	0.0595	0.0344
4.0	3.6295	0.1000	0.3577	20.0	9.1972	0.0595	0.0408
4.0	6.8780	0.1000	0.4171	4.0	4.6694	0.0603	0.0215
4.0	7.0717	0.1000	0.4137	10.0	9.7090	0.0603	0.0215
4.0	3.8708	0.1000	0.3603	15.0	8.0441	0.0603	0.0362
4.0	4.8758	0.1000	0.3890	20.0	11.8477	0.0603	0.0319
4.0	5.1420	0.3000	0.5027	4.0	4.9583	0.0395	0.0363

4.0	4.7865	0.3000	0.4292	10.0	10.6671	0.0395	0.0395
4.0	3.8265	0.3000	0.4224	15.0	12.9812	0.0395	0.0473
4.0	3.3194	0.3000	0.4053	20.0	15.0381	0.0395	0.0530
4.0	5.0121	0.3000	0.5035	4.0	5.4534	0.0595	0.0464
4.0	5.2484	0.3000	0.4176	10.0	12.2062	0.0595	0.0509
4.0	4.1662	0.3000	0.4154	15.0	14.8891	0.0595	0.0544
4.0	3.4834	0.3000	0.4642	20.0	18.4883	0.0595	0.0559
4.0	6.1183	0.3000	0.4853	4.0	6.2171	0.0603	0.0423
4.0	5.0804	0.3000	0.4422	10.0	12.4221	0.0603	0.0497
4.0	4.1123	0.3000	0.4263	15.0	15.0757	0.0603	0.0554
4.0	3.6272	0.3000	0.4054	20.0	17.3520	0.0603	0.0603
4.0	4.7586	0.5000	0.5115	4.0	4.1311	0.0395	0.0419
4.0	4.1054	0.5000	0.4438	10.0	8.9184	0.0395	0.0442
4.0	4.2479	0.5000	0.4230	15.0	13.0823	0.0395	0.0466
4.0	3.6127	0.5000	0.3992	20.0	14.8039	0.0395	0.0532
4.0	6.1707	0.5000	0.4810	4.0	5.6209	0.0595	0.0440
4.0	5.4670	0.5000	0.4278	10.0	12.0520	0.0595	0.0489
4.0	4.1814	0.5000	0.4307	15.0	14.5755	0.0595	0.0542
4.0	3.7616	0.5000	0.4328	20.0	17.1844	0.0595	0.0597
4.0	6.4548	0.5000	0.4737	4.0	5.8032	0.0603	0.0432
4.0	5.4692	0.5000	0.4253	10.0	11.9739	0.0603	0.0501
4.0	4.6106	0.5000	0.4134	15.0	15.2597	0.0603	0.0550
4.0	3.8447	0.5000	0.3969	20.0	17.3354	0.0603	0.0597
4.0	5.1447	0.7400	0.4988	4.0	3.6858	0.0395	0.0393
4.0	4.5949	0.7400	0.4453	10.0	8.3500	0.0395	0.0405
4.0	4.2817	0.7400	0.4226	15.0	11.4447	0.0395	0.0448
4.0	3.8772	0.7400	0.4224	20.0	14.0779	0.0395	0.0479
4.0	6.0951	0.7400	0.4760	4.0	4.7090	0.0595	0.0445
4.0	6.0146	0.7400	0.4195	10.0	10.9263	0.0595	0.0472
4.0	4.8585	0.7400	0.4019	15.0	13.5157	0.0595	0.0545

4.0	4.0919	0.7400	0.4124	20.0	15.7375	0.0595	0.0584
4.0	7.0306	0.7400	0.4931	4.0	5.4428	0.0603	0.0394
4.0	5.8721	0.7400	0.4163	10.0	10.8844	0.0603	0.0473
4.0	4.9166	0.7400	0.4154	15.0	13.8138	0.0603	0.0539
4.0	4.1923	0.7400	0.4272	20.0	16.2799	0.0603	0.0557
7.0	8.7602	0.1000	0.4093	4.0	3.0455	0.0395	0.0254
7.0	5.8719	0.1000	0.3576	10.0	4.8053	0.0395	0.0317
7.0	6.9518	0.1000	0.3702	15.0	8.3649	0.0395	0.0245
7.0	4.4792	0.1000	0.3505	20.0	7.2455	0.0395	0.0355
7.0	5.4903	0.1000	0.5283	4.0	2.8809	0.0595	0.0339
7.0	7.8529	0.1000	0.3891	10.0	6.1562	0.0595	0.0319
7.0	6.7538	0.1000	0.4521	15.0	8.3427	0.0595	0.0325
7.0	6.6867	0.1000	0.4247	20.0	9.7017	0.0595	0.0359
7.0	4.9924	0.1000	0.4914	4.0	2.8180	0.0603	0.0315
7.0	4.7679	0.1000	0.4935	10.0	5.1888	0.0603	0.0363
7.0	5.6360	0.1000	0.3756	15.0	6.4321	0.0603	0.0423
7.0	7.2107	0.1000	0.3957	20.0	9.9918	0.0603	0.0357
7.0	6.1864	0.3000	0.4988	4.0	3.7908	0.0395	0.0450
7.0	6.0125	0.3000	0.4336	10.0	8.4399	0.0395	0.0473
7.0	5.7857	0.3000	0.4104	15.0	11.6835	0.0395	0.0506
7.0	5.2245	0.3000	0.4054	20.0	14.0654	0.0395	0.0551
7.0	7.6209	0.3000	0.4783	4.0	4.7511	0.0595	0.0495
7.0	7.0591	0.3000	0.4362	10.0	9.9585	0.0595	0.0549
7.0	6.2797	0.3000	0.3961	15.0	12.8547	0.0595	0.0598
7.0	5.9429	0.3000	0.4387	20.0	16.9391	0.0595	0.0595
7.0	7.9742	0.3000	0.4887	4.0	5.1518	0.0603	0.0475
7.0	6.9467	0.3000	0.4557	10.0	10.2497	0.0603	0.0558
7.0	6.6034	0.3000	0.4251	15.0	13.8922	0.0603	0.0588
7.0	5.6144	0.3000	0.4543	20.0	16.5804	0.0603	0.0597
7.0	7.8417	0.5000	0.4568	4.0	3.8047	0.0395	0.0430

7.0	6.6363	0.5000	0.4516	10.0	8.7481	0.0395	0.0449
7.0	5.8776	0.5000	0.4343	15.0	11.4364	0.0395	0.0507
7.0	5.2348	0.5000	0.4344	20.0	13.7045	0.0395	0.0543
7.0	8.1276	0.5000	0.4781	4.0	4.5709	0.0595	0.0499
7.0	7.6344	0.5000	0.4522	10.0	10.3154	0.0595	0.0543
7.0	6.7473	0.5000	0.4254	15.0	13.1876	0.0595	0.0593
7.0	6.3252	0.5000	0.4688	20.0	17.7008	0.0595	0.0566
7.0	8.2423	0.5000	0.4711	4.0	4.5686	0.0603	0.0510
7.0	7.4158	0.5000	0.4148	10.0	9.4779	0.0603	0.0573
7.0	6.9750	0.5000	0.4300	15.0	13.7133	0.0603	0.0585
7.0	6.3921	0.5000	0.4411	20.0	17.0936	0.0603	0.0587
7.0	6.3548	0.7400	0.5070	4.0	2.8994	0.0395	0.0476
7.0	6.8418	0.7400	0.4794	10.0	7.9344	0.0395	0.0432
7.0	6.3752	0.7400	0.4325	15.0	10.4173	0.0395	0.0477
7.0	5.6447	0.7400	0.4221	20.0	12.2113	0.0395	0.0525
7.0	8.7533	0.7400	0.4982	4.0	4.1723	0.0595	0.0490
7.0	7.3606	0.7400	0.4547	10.0	8.5901	0.0595	0.0543
7.0	6.8219	0.7400	0.4468	15.0	11.9169	0.0595	0.0557
7.0	6.0518	0.7400	0.4506	20.0	14.2296	0.0595	0.0597
7.0	8.0802	0.7400	0.4766	4.0	3.8412	0.0603	0.0504
7.0	7.3907	0.7400	0.4626	10.0	8.6984	0.0603	0.0548
7.0	7.0499	0.7400	0.4227	15.0	11.7948	0.0603	0.0588
7.0	6.4497	0.7400	0.4403	20.0	14.8459	0.0603	0.0593
10.0	6.1102	0.1000	0.4850	4.0	2.1580	0.0395	0.0324
10.0	5.9313	0.1000	0.4870	10.0	5.0589	0.0395	0.0264
10.0	6.7517	0.1000	0.4530	15.0	6.8171	0.0395	0.0277
10.0	7.1897	0.1000	0.4405	20.0	8.1725	0.0395	0.0302
10.0	6.4573	0.1000	0.4934	4.0	2.3937	0.0595	0.0356
10.0	5.3762	0.1000	0.5218	10.0	4.4035	0.0595	0.0402
10.0	7.0181	0.1000	0.4383	15.0	6.2134	0.0595	0.0398

10.0	7.9236	0.1000	0.4270	20.0	8.3358	0.0595	0.0384
10.0	6.3143	0.1000	0.5608	4.0	2.3217	0.0603	0.0404
10.0	7.6233	0.1000	0.4965	10.0	5.6637	0.0603	0.0318
10.0	7.3716	0.1000	0.4492	15.0	6.6316	0.0603	0.0375
10.0	6.6128	0.1000	0.4930	20.0	7.9196	0.0603	0.0416
10.0	8.5930	0.3000	0.5014	4.0	3.7873	0.0395	0.0450
10.0	7.4563	0.3000	0.4553	10.0	7.7042	0.0395	0.0503
10.0	6.7316	0.3000	0.4688	15.0	10.6572	0.0395	0.0530
10.0	6.3142	0.3000	0.4424	20.0	12.7619	0.0395	0.0571
10.0	8.8241	0.3000	0.4993	4.0	4.1557	0.0595	0.0543
10.0	8.8233	0.3000	0.4319	10.0	8.8598	0.0595	0.0602
10.0	7.6648	0.3000	0.4696	15.0	12.4001	0.0595	0.0588
10.0	7.7783	0.3000	0.4727	20.0	16.7783	0.0595	0.0583
10.0	8.8301	0.3000	0.4803	4.0	4.0222	0.0603	0.0557
10.0	8.1032	0.3000	0.4734	10.0	8.8226	0.0603	0.0602
10.0	8.5979	0.3000	0.4594	15.0	13.5619	0.0603	0.0579
10.0	7.6996	0.3000	0.4202	20.0	15.1840	0.0603	0.0603
10.0	7.8364	0.5000	0.4695	4.0	2.9607	0.0395	0.0508
10.0	7.4755	0.5000	0.4653	10.0	7.2268	0.0395	0.0517
10.0	7.6255	0.5000	0.4249	15.0	10.3207	0.0395	0.0545
10.0	6.4433	0.5000	0.4076	20.0	11.5881	0.0395	0.0588
10.0	9.0187	0.5000	0.4860	4.0	3.7687	0.0595	0.0558
10.0	8.9417	0.5000	0.4640	10.0	8.7709	0.0595	0.0598
10.0	8.1527	0.5000	0.4581	15.0	12.0069	0.0595	0.0602
10.0	8.2100	0.5000	0.4502	20.0	15.7493	0.0595	0.0594
10.0	9.3466	0.5000	0.4815	4.0	3.8352	0.0603	0.0562
10.0	8.9149	0.5000	0.4750	10.0	8.9595	0.0603	0.0582
10.0	7.4900	0.5000	0.4474	15.0	10.8364	0.0603	0.0603
10.0	8.1815	0.5000	0.4643	20.0	15.9920	0.0603	0.0595
10.0	8.9305	0.7400	0.4223	4.0	2.5091	0.0395	0.0510

10.0	7.3537	0.7400	0.4692	10.0	6.0731	0.0395	0.0521
10.0	7.2295	0.7400	0.4471	15.0	8.7062	0.0395	0.0534
10.0	7.2033	0.7400	0.4378	20.0	11.2786	0.0395	0.0560
10.0	9.1491	0.7400	0.4696	4.0	3.1286	0.0595	0.0556
10.0	8.9681	0.7400	0.4565	10.0	7.3421	0.0595	0.0598
10.0	9.1938	0.7400	0.4692	15.0	11.6826	0.0595	0.0576
10.0	8.1225	0.7400	0.4413	20.0	13.0905	0.0595	0.0603
10.0	9.4143	0.7400	0.5095	4.0	3.3582	0.0603	0.0552
10.0	9.4256	0.7400	0.4722	10.0	7.9732	0.0603	0.0569
10.0	9.4452	0.7400	0.4791	15.0	12.0159	0.0603	0.0564
10.0	8.4490	0.7400	0.4181	20.0	13.3582	0.0603	0.0603

Table A.1: Results of the estimation process conducted on simulated reflectance spectra of the human colon

Appendix B

Error Correction Algorithm

In this chapter, we summarise the error correction algorithm devised by Hidovic-Rowe and described in details in (Hidovic-Rowe, 2006; Hidovic-Rowe et al., 2006). We use K to represent the fast, yet not suitably accurate, Kubelka-Munk based model. We also represent the far more accurate but also more computationally expensive model (MCML) as M. We thus define the error function E as the function describing the difference between M and K: $E(\boldsymbol{\theta}) = M(\boldsymbol{\theta}) - K(\boldsymbol{\theta})$. We then define a surrogate model S that encapsulates our knowledge of the error function as $S = K(\boldsymbol{\theta}) + E(\boldsymbol{\theta})$. When estimating the error function for the next cycle, we need to find the differential dE at $\boldsymbol{\theta}$ as $\mathbf{A}$, which we the use to define the vector $b = E(\boldsymbol{\theta}) - \mathbf{A}(\boldsymbol{\theta})$, making the error function $E(x) = \mathbf{A}(x) + b$. We update the surrogate model at each cycle using the following algorithm:

1. Initially set $\mathbf{A}$ and b to a matrix and vector of zeros respectively. This makes our surrogate model identical to the Kubelka-Munk based function.

2. At cycle t, find an estimate $\hat{\boldsymbol{\theta}}$ using our inversion method, and S as the forward model required.

3. Let $F(\hat{\boldsymbol{\theta}}) = M(\hat{\boldsymbol{\theta}}) - S(\hat{\boldsymbol{\theta}})$ be the surrogate error function, between the accurate model M and the present surrogate S at point $\hat{\boldsymbol{\theta}}$ found in the previous step.

4. Estimate the differential dF at $\hat{\boldsymbol{\theta}}$ by the matrix $\mathbf{B}$ which can be calculated using the following algorithm:

   For each parameter k:

   - Set e_k as a zeros vector of the same length as $\hat{\boldsymbol{\theta}}$. Set the element at position k to be one.

- To determine the k^{th} column of matrix $\mathbf{B}$, we simply approximate F so $F(\hat{\boldsymbol{\theta}} + \delta e_{_k}) = \mathbf{B}(\delta e_{_k} + \hat{\boldsymbol{\theta}} - \hat{\boldsymbol{\theta}}) + F(\hat{\boldsymbol{\theta}})$. Each column can therefore be defined as:

$$\mathbf{B}(:, k) = \frac{1}{\delta}(M(\hat{\boldsymbol{\theta}} + \delta e_{_k}) - S(\hat{\boldsymbol{\theta}} + \delta e_{_k}) - F(\hat{\boldsymbol{\theta}}))$$

  where the accurate model M and the surrogate S are run on the perturbed vector $\hat{\boldsymbol{\theta}} + \delta e_{_k}$, and δ is small compared with the bounds chosen for $\hat{\boldsymbol{\theta}}$.

5. Set $\mathbf{A} = \mathbf{A} + \mathbf{B}$
6. Set $b = b + F(\hat{\boldsymbol{\theta}}) + \mathbf{B}(\hat{\boldsymbol{\theta}})$
7. Repeat steps $2 - 5$ as often as necessary

This means that each cycle requires $n + 1$ runs of the accurate model M where n is the number of parameters in our unknown vector $\boldsymbol{\theta}$. We run 20 iterations of this algorithm, with each run requiring $n+1$ evaluations of M, making the inversion process far less time consuming than a direct inversion that may require around 200 - 300 iterations.

References

Igor Aleksander and Helen Morton. *Introduction to Neural Computing*. Cengage Learning EMEA, 1995.

R. Anderson, , and J.A. Parrish. The optics of human skin. *Journal of Invistigative Dermatology*, 77:13–19, 1981a.

R. Anderson, B. S. Parrish, and J. Parrish. The optics of human skin. *The Journal of Investigative Dermatology*, 77(1), 1981b.

S. R. Arridge and M. Schweiger. A gradient-based optimisation scheme for optical tomography. *Optics Express*, 1998.

S. R. Arridge and M Schweiger. Use of multiple data types in time-resolved optical absorption and scattering tomography. volume 2035, 1993.

S. R. Arridge, M. Schweiger, M. Hiraoka, and D. T. Delpy. A finite element approach for modeling photon transport in tissue. *Medical Physics*, 20:299–309, 1993.

S.R. Arridge. Optical tomography in medical imaging. *Inverse Problems*, 15:R41–R93, 1999.

S.R. Arridge and J.C. Hebden. Optical imaging in medicine: II. modelling and reconstriction. *Physics in Medicine and Biology*, 42:841–853, 1997.

R. Attaie and R. L. Richtert. Size distribution of fat globules in goat milk. *Journal of Dairy Science*, 83:940–944, 2000.

Andrew P Bagshaw, Adam D Liston, Richard H Bayford, Andrew Tizzard, Adam P Gibson, A Thomas Tidswell, Matthew K Sparkes, Hamid Dehghani, Colin D Binnie, and David S Holder. Electrical impedance tomography of human brain function using reconstruction algorithms based on the finite element method. *NeuroImage*, 20(2):752–764, 2003.

A. N. Bashkatov, E. A. Genina, and V. V. Tuchin. Optical optical properties of skin, subcutaneous, and muscle tissues: A review. *Journal of Innovative Optical Health Sciences*, 4(1):9–38, 2011.

T. Binzoni, A. Vogel, A.H. Gandjbakhche, and R. Marchesini. Detection Limits of Multispectral Optical Imaging under the Skin Surface. *Physics in Medicine and Biology*, 53: 617–636, 2008.

Ake Bjõrck. *Numerical Methods for Least Squares Problems*. Society for Industrial and Applied Mathematics, 1996.

Abhijit J Chaudhari, Felix Darvas, James R Bading, Rex A Moats, Peter S Conti, Desmond J Smith, Simon R Cherry, and Richard M Leahy. Hyperspectral and multispectral bioluminescence optical tomography for small animal imaging. *Physics in medicine and biology*, 50(23):5421, 2005.

Z. Chen, A. Taflove, and V. Backman. Concept of equiphase sphere for light scattering by non-spherical dielectric particles. *J. Opt. Soc. Am. A. Opt. Image. Sci. Vis.*, 21:88–97, 2004.

W. F. Cheong, S. A. Prahl, and A. J. Welch. A review of the optical properties of biological tissues. *IEEE Journal of Quantum Electronics*, 26(12):2166–2185, 1990.

E. Claridge and S.J Preece. An inverse method for the recovery of tissue parameters from colour images. *Information Processing in Medical Imaging*, LNCS 2732:306–317, 2003.

Ela Claridge, Symon Cotton, Per Hall, and Marc Moncrieff. From colour tissue histology: Physics-based interpreation of images of pigmented skin lesions. *Medical Image Analysis*, 7:489–502, 2003.

G. W. Corder and D. I. Foreman. *Nonparametric Statistics for Non-Statisticians*. John Wiley & Sons, 2009.

A. Corlu, T. Durduran, and R. Choe. Uniqueness and wavelength optimisation in continuous-wave multispectral diffuse optical tomography. *Optics Letters*, 28:2339–2341, 2003.

A. Corlu, R. Choe, T. Durduran, K. Lee, M. Schweiger, S.R. Arridge, E.M.C Hillman, and A.G. Yodh. Diffuse optical tomography with spectral constraints and wavelength optimization. *Applied Optics*, 44:2082–2093, 2005.

S. Cotton, E. Claridge, and P. Hall. A skin imaging method based on a colour formation model and its application to the diagnosis of pigmented skin lesions. In *Proceeding of Medical Image Understanding and Analysis*, 1999.

Symon Cotton, Ela Claridge, and Per Hall. Assisting diagnosis of melanoma through the "noninvasive" biopsy of skin lesions. In *Proceedings of Medical Image Understanding and Analysis*, 1997.

Symon D'Oyly Cotton. *A non-invasive imaging system for assisting in the diagnosis of malignant melanoma*. PhD thesis, School of Computer Science.
The University of Birmingham, 1998.

Beatriz Morales Cruzado, Sergio Vazquez y Montiel, and Jose Alberto Delgado Atencio. Genetic algorithms and mcml program for recovery of optical properties of homogeneous turbid media. *Biomed Opt Express*, 4(3):433–446, 2013.

J. B. Dawson, D. J. Barker, J. D. Ellis, E. Grassam, J.A. Cotterill, G. W. Fisher, and J.W. Feather. A theoretical and experimental study of light absorption and scattering by in vivo skin. *Phys. Med. Biol*, 25:695–709, 1980.

D. W. Day, J. R. R. Jass, A. B. Price, N. A. Shepherd, J. M. Sloan, N. J. Talbot, G. T. Williams, and B. F. , Warren. *Morson and Dawson's Gastrointestinal Pathology*. Wiley-Blackwel, 2003.

H. C. Van de Hulst. *Multiple Light Scattering*. Academic Press, New York, 1980.

A.R. De Pierro and M.E.B. Amagishi. Fast EM like methods for maximum "*A Posteriori*" estimates in emission tomography. *IEEE Transaction on Medical Imaging*, 20:280–288, 2001.

Hamid Dehghani, Brian W Pogue, Steven P Poplack, and Keith D Paulsen. Multiwavelength three-dimensional near-infrared tomography of the breast: initial simulation, phantom, and clinical results. *Applied Optics*, 42(1):135–145, 2003.

Hamid Dehghani, Matthew E Eames, Phaneendra K Yalavarthy, Scott C Davis, Subhadra Srinivasan, Colin M Carpenter, Brian W Pogue, and Keith D Paulsen. Near infrared optical tomography using nirfast: Algorithm for numerical model and image reconstruction. *Communications in numerical methods in engineering*, 25(6):711–732, 2009.

A.P. Dempster, N.M. Laird, and D.B. Rubin. Maximum likelihood from incomplete data via the EM algorithm. *Journal of the Royal Statistical Society. Series B*, 39:1–38, 1977.

R.M.P. Doornbos, R. Lang, M.C. Aslders, F.W. Cross, and H.J.C.M. Sterenborg. The determination of *in vivo* human tissue optical properties and absolute chromophore concentrations using spacially resolved steady-state diffuse reflectance spectroscopy. *Physics in Medicine and Biology*, 44:967–981, 1999.

F. A. Duck. *Physical Properties of Tissue: A Comprehensive Reference Book*. Academic Press, London (1990), 1990.

W. G. Egan and T. W. Hilgeman. *Optical Properties of Inhomogeneous Materials*. Academic Press, 1979.

J. P. Elisee. *Innovative Boundary Integral and Hybrid Methods for Diffuse Optical Imaging*. PhD thesis, Department of Computer Science. University College London, 2011.

Qianqian Fang and David A. Boas. Monte carlo simulation of photon migration in 3d turbid media accelerated by graphics processing units. *Opt. Express*, 17:20178–20190, 2013.

W.G. Faris. Lectures on statistics. http://math.arizona.edu/ faris/stat.pdf, July 2009.

T.J. Farrell, M.S. Patterson, and B. Wilson. The use of a neural network to determine tissue optical properties from spatially resolved diffuse reflectance measurements. *Physics in Medicine and Biology*, 37(12):2281–2286, 1992a. URL `http://stacks.iop.org/0031-9155/37/2281`.

T.J. Farrell, M.S. Patterson, and B. Wilson. A diffusion theory model of spacially resolved, steady-state diffuse reflectance for the noninvasive determination of tissue optical properties *in vivo*. *Medical Physics*, 19:879–888, 1992b.

Tom Fawcett. An introduction to roc analysis. *Pattern Recogn. Lett.*, 27(8):861–874, June 2006. doi: 10.1016/j.patrec.2005.10.010. URL `http://dx.doi.org/10.1016/j.patrec.2005.10.010`.

M. Firbank, S. R. Arridge, M. Schweiger, and D. T. Delpy. An investigation of light transport through scattering bodies with non-scattering regions. *Physics in Medicine and Biology*, 41(4):767, 1996.

R. (Roger) Fletcher. *Practical methods of optimization*. Wiley-Interscience, 2001.

P. F. Fox and P. L. H. McSweeny. *Dairy Chemistry and Biochemistry*. Blackie Academic and Professional, London, 1998.

J. R. Frisvad, N. J. Christensen, and H. W. Jensen. Computing the scattering properties of participating media using lorenz-mie theory. In *ACM Transactions on Graphics (TOG) - Proceedings of ACM SIGGRAPH*, volume 26(3), 2007.

Y. Furuya and T. Ogata. Scanning electron microscopic study of the collagen networks of the normal mucosa, hyperplastic polyp, tubular adenoma and adenocarcinoma of the human large intestine. *Tohoku Journal of Experimental Medicine*, 169:1–19, 1993.

Henri P. Gavin. The levenberg-marquardt method for nonlinear least squares curve-fitting problems. 2013.

E. Ge, K. T. Schomacker, and N. S. Nishioka. Identification of colonic dysplasia and neoplasia by diffuse reflectance spectroscopy and pattern recognition techniques. *Applied Spectroscopy*, 52:833–839, 1998.

S.C. Gebhart, W.C. Lin, and A. Mahadevan-Jansen. In vitro determination of normal and neoplastic human brain tissue optical properties using inverse adding-doubling. *Physics in Medicine and Biology*, 51:2011–2027, 2006.

S. Geman and D.E. McClure. Bayesian image analysis: An application to single photon tomography. In *Proceedings of the AMerican Statistical Society*, pages 12–18, 1985.

A.P. Gibson, J.C. Hebden, and S.R. Arridge. Recent advances in diffuse optical imaging. *Physics in Medicine and Biology*, 50:R1–R43, 2005.

Gavin J Gibson. Statistical inference : Notes, tutorials and solutions. 2005. URL `http://www.ma.hw.ac.uk/~gavin/stats5/`.

P.E. Gill and W. Murray. Algorithms for the solution of the nonlinear least-squares problem. *SIAM Journal on Numerical Analysis*, 15:977–992, 1978.

GLOBOCAN. Colorectal cancer incidence, mortality and prevalence worldwide in 2008. GLOBOCAN 2008, 10 2008. URL `http://globocan.iarc.fr/factsheet.asp`.

C. Gondro and B.P. Kinghorn. A simple genetic algorithm for multiple sequence alignment. *Genetic Molecular Research*, 6:964–82, 2007.

J.A. Gualtieri and B.K. Pursi. Solving inversion problems with neural networks. *Neural Networks*, 3:955–960, 1990.

M. Hammer and D. Schweitzer. Quantitative reflectance spectroscopy at the human ocular fundus. *Journal of Atmospheric Sciences*, 33:2452–2459, 1976.

M. Hammer, A. Roggan, D. Schweitzer, and G. Muller. Optical properties of ocular fundus tissues - an in vitro study using the double integrating sphere technique and inverse Monte Carlo simulation. *Physics in Medicine and Biology*, 40:963–978, 1995.

K.M. Hanson. Introduction to bayesian image analysis. In *Medical Imaging: Image Processing*, number 1898 in SPIE, pages 716–731, 1993.

L. G. Henyey and J.L. Greenstein. Diffuse radiation in the galaxy. *Astrophysical Journal*, 93:70–83, 1941.

D. Hidovic and J. E. Rowe. Validating a model of colon colouration using an evolution strategy with adaptive approximations. In *Genetic and Evolutionary Computation Conference*, pages 1005–1017, 2004.

D. Hidovic-Rowe and E. Claridge. Model based recovery of histological parameters from multi spectral images of the colon. In Flynn M.J., editor, *Proceedings SPIE*, volume 5745, pages 127–137, 2005.

Dzena Hidovic-Rowe. *Model based analysis of colon reflectance.* PhD thesis, School of Computer Science. The University of Birmingham, 2006.

Dzena Hidovic-Rowe, Jonathan E. Rowe, and Manuela Lualdi. Markov models of integrating spheres for hyperspectral imaging. *Applied Optics*, 45(21):5248–5257, 2006.

M. Hilska, Y. Collan, J. Peltonen, R. Gullichsen, H. Paajanen, and M. Laato. The distribution of collagen types i, iii and iv in normal and malignant colorectal mucosa. *European Journal of Surgery*, 164:457–464, 1998.

Z. Huang, W. Zheng, S. Xie, R. Chen, H. Zeng, D. I. McLean, and H. Lui. Laser induced autofluorescence microscopy of normal and tumor human colonic tissue. *Int. J. Oncol*, 24:59–63, 2004.

H.M. Hudson and R.S. Larkin. Accelerated image reconstruction using orderd subsets of projection data. *IEEE Transactions on Medical Imaging*, 13:601–609, 1994.

S. L. Jacques, C. A. Alter, and S. A. Prahl. Angular dependence of hene laser light by human dermis. *Laser Life Science*, 1:309–333, 1987.

Steven Jacques. Skin Optics, 1998. http://omlc.ogi.edu/news/jan98/skinoptics.html (February 2008).

G. Jagajothi and S. Raghavan. Estimation and measurement of biological tissues using optical simulation method. *Progress In Electromagnetics Research M*, 6:155–165, 2009.

Steven M. Kay. *Fundamentals of Statistical Signal Processing: Estimation Theory.* Prentic Hall, 1993.

P. Kearney, R. E. Smith, C. Bonacina, and T. Eymann. Integration of computational models inspired by economics and genetics. *BT Technology Journal*, 18:150–61, 2000.

Robert E. Keller and Wolfgang Banzhaf. Genetic programming using genotype-phenotype mapping from linear genomes into linear phenotypes. In *Genetic Programming 1996: Proceedings of the First Annual Conference*, pages 116–122. MIT Press, 1996.

A. Kienle, L. Lilge, M.S. Patterson, R. Hibst, R. Steiner, and B.C. Wilson. Spatially resolved absolute diffuse reflectance measurements for noninvasive determination of the optical scattering and absorption coefficients of biological tissue. *Applied Optics*, 35(13): 2304–2314, 1996.

A. Kienle, M.S. Patterson, N. Dognitz, R. Bays, G. Wagniere, and H. Van den Berg. Noninvasive determination of the optical properties of two-layered turbid media. *Applied Optics*, 37:779–791, 1998.

Alwin Kienle and Michael S. Patterson. Improved solutions of the steady-state and the time-resolved diffusion equations for reflectance from a semi-infinite turbid medium. *Journal of Optics Society*, 14:246–254, 1997.

Vitaly P. Kutavichus, Valery V. Filippov, and Vitali H. Huzouski. Determination of optical parameters and thickness of weakly absorbing thin films from reflectance and transmittance spectra. *Appl. Opt.*, 45(19):4547–4553, Jul 2006. doi: 10.1364/AO.45.004547. URL `http://ao.osa.org/abstract.cfm?URI=ao-45-19-4547`.

Ivo W. Kwee. *Towards a Bayesian Framework for Optical Tomography.* PhD thesis, Department of Medical Physics and Bioengineering, University College London, 1999.

Kenneth Levenberg. A method for the solution of certain non-linear problems in least squares. *The Quarterly of Applied Mathematics*, 2:164–168, 1944.

Y. Li, K.H. Ang, G.C.Y. Chong, W. Feng, K.C. Tan, and H Kashiwagi. Cautocsd-evolutionary search and optimisation enabled computer automated control system design. *International Journal of Automation and Computing*, 1:76–88, 2004.

David MacKay. *Information Theory , Inference And Learning Algorithms.* Cambridge University Press, 2003. ISBN 9780521670517. URL `http://www.inference.phy.cam.ac.uk/itila/book.html`.

Donald Marquardt. An algorithm for least-squares estimation of nonlinear parameters. *SIAM Journal on Applied Mathematics*, 11:431–441, 1963.

S. J. Matcher. *Handbook of Optical Biomedical Diagnostics*, chapter 9:Signal Quantification and Localization n Tissue Near-Infrared Spectroscopy. SPIE Optical Engineering Press, 2001.

S.J. Matcher, M. Cope, and D.T. Delpy. In vivo measurements of the wavelength dependence of tissue scattering coefficients between 760 and 900 nm measured with time resolved spectroscopy. *Applied Optics*, 36(1):386–396, 1997.

Christian Matzler. Matlab functions for mie scattering and absorption. Technical report, Universitas Bernensis, 2002.

I. V. Meglinski and S. J. Matcher. Computer simulation of the skin reflectance spectra. *Computer Methods and Programs in Biomedicine*, 70:179–186, 2003.

J.R. Mourant, T. Fuselier, J. Boyer, T.M. Johnson, and I.J. Bigio. Predictions and measurements of scattering and absorption over broad wavelength ranges in tissue phantoms. *Applied Optics*, 36:949–957, 1997.

James H Nobbs. Kubelka-Munk Theory and the Prediction of Reflectance. *Review of Progress in Coloration and Related Topics*, 15:66–75, 1985.

Jorge Nocedal and Stephen Wright. *Numerical Optimization.* Springer Series in Operations Research and Financial Engineering. Springer, 1999.

D.J. Olive. A course in statistical theory. http://www.math.siu.edu/olive/irun.pdf.

G.M. Palmer and N. Ramanujam. Monte Carlo-based inverse model for calculating tissue optical properties. part i: Theory and validation on synthetic phantoms. *Applied Optics*, 45(5):1062–1071, 2006.

G.M. Palmer, C. Zhu, T.M. Breslin, F. Xu, K.W. Gilchrist, and N. Ramanujam. Monte Carlo-based inverse model for calculating tissue optical properties. part ii: Application to breast cancer diagnosis. *Applied Optics*, 45(5):1072–1078, 2006. URL `http://ao.osa.org/abstract.cfm?URI=ao-45-5-1072`.

M.S. Patterson, B. Chance, and B.C. Wilson. Time resolved reflectance and transmittance for the noninvasive measurement of tissue optical properties. *Applied Optics*, 28(12): 2331–2336, 1989.

M.S. Patterson, J.D. Moulton, B.C. Wilson, K.W. Berndt, and J.R. Lakowicz. Frequency domain reflectance for the determination of the scattering and absorption properties of tissue. *Applied Optics*, 30(31):4474–4476, 1991.

T.J. Pfefer, L.S. Matchette, C.L. Bennett, J.A. Gall, J.N. Wilke, A.J. Durkin, and M.N. Ediger. Reflectance-based determination of optical properties in highly attenuating tissue. *Journal of Biomedical Optics*, 8:206–215, 2003.

S. Prahl. *Optical-Thermal Response of Laser Irradiated Tissue*, chapter 5, pages 101–129. Plenum Press, 1995a.

S. A. Prahl. Optical absorption spectra for haemoglobin. Oregon Medical Laser Centre, 10 2007a. URL `http://omlc.ogi.edu/spectra/hemoglobin/index.html`.

S. A. Prahl. Optical absorption spectra for melanin. Oregon Medical Laser Centre, 12 2007b. URL `http://omlc.ogi.edu/spectra/melanin/mua.html`.

S. A. Prahl. A user's manual for the inverse adding-doubling program: a compendium of worries. 1993.

S. A. Prahl. The adding-doubling method. In A. J. Welch and M. J. C. van Gemert, editors, *Optical-Thermal Response of Laser Irradiated Tissue*, chapter 5, pages 101–129. Plenum Press, 1995b.

S. A. Prahl, M. Keijzer, S. L. Jacques, and A. J. Welch. A Monte Carlo model of light propagation in tissue. In G. J. Müller and D. H. Sliney, editors, *SPIE Proceedings of Dosimetry of Laser Radiation in Medicine and Biology*, volume IS 5, pages 102–111, 1989.

S. A. Prahl, M. J. C. Van Gemert, N. Van Wieringen, and A. J. Welch. Iterated adding-doubling to determine optical properties. San Jose, nov 1991.

S. A. Prahl, M. J. C. Van Gemert, and A. J. Welch. Determining the optical properties of turbid media by using the adding-doubling method. *Appl. Opt.*, 32:559–568, 1993a.

S.A. Prahl, M.J.C. Van Gemert, and A.J. Welch. Determining the optical properties of turbid media using the adding-doubling method. *Applied Optics*, 32:559–568, 1993b.

S.J. Preece and E. Claridge. Physics-based approach to geometry-insensitive recovery of quantitative scene parameters from images. Technical report, School of Computer Science. The University of Birmingham, 2004.

S.J. Preece, I.B. Styles, S.D. Cotton, E. Claridge, and A. Calcagni. *Medical Image Computing and Computer-Assisted Intervention*, volume 3750/2005 of *Lecture Notes in Computer Science*, chapter Model Based Parameter Recovery from Uncalibrated Optical Images, pages 509–516. Springer Berlin / Heidelberg, 2005.

W.H. Press, B.P. Flannery, S.A. Teukolsky, and W.T. Vetterling. *Numerical Recipes in Pascal: The Art of Scientific Computing*. Cambridge University Press, 1989.

J. Qin and R. Lu. Measurement of the absorption and scattering properties of turbid liquid foods using hyperspectral imaging. *Applied Spectroscopy*, 61(4):388–396, 2007.

Gustav Quade. Cutaneous layers, 2008. URL `http://www.meb.uni-bonn.de/Cancernet/CDR0000062713.html`.

T. Reuter, S. Karl, M. Hoffmann, B. Dietzek, and J. Popp. Determination of the optical properties of native joint cartillage with nir-spectroscopy. *Biomed Tech*, 58(Suppl. 1), 2013.

Stuart J. Russel and Peter Norvig. *Artificial Intelligence: A modern Approach*. Upper Saddle River, New Jersey: Prentice Hall, 2003.

T. J. Ryan. *Physiology, Biochemistry and Molecular Biology of the Skin*, volume 1, chapter Cutaneous Circulation, pages 1019–84. Oxford University Press, 1991.

E. Salomatina and A. N. Yaroslavsky. Evaluation of the *in vivo* and *ex vivo* optical properties in a mouse ear model. *Phys. Med. Biol*, 53:2797–2807, 2008.

Jane Sandby-Moller, Thomas Poulsen, and Hans Christian Wulf. Epidermal thickness at different body sites: Relationship to age, gender, pigmentation, blood content, skin type and smoking. *Acta Derm Benereol*, 83:410–413, 2003.

M. Schweiger, S.R. Arridge, M. Hiraoka, and D.T. Delpy. The finite element method for the propagation of light in scattering media: boundary and source conditions. *Medical physics*, 22(11):1779–1792, 1995.

Martin Schweiger and Simon Arridge. The toast++ software suite for forward and inverse modeling in optical tomography. *Journal of Biomedical Optics*, 19(4):040801, 2014. URL `http://web4.cs.ucl.ac.uk/research/vis/toast/intro.html`.

C. R. Simpson, M. Kohl, M. Essenpreis, and M. Cope. Near-infrared optical properties of ex vivo human skin and subcutaneous tissues measured using the monte carlo inversion technique. *Phys. Med. Biol*, 43:2465–2478, 1998.

S. A. Skinner, G. M. Frydman, and P. E. O'Brien. Microvascular structure of benign and malignant tumors of the colon in humans. *Digestive Diseases and Sciences*, 40:373–384, 1995.

Jan A. Snyman. *Practical Mathematical Optimization: An introduction to basic optimization theory and classical and new gradient-based algorithms*. Springer, Cambridge, Massachusetts, 2005.

Subhadra Srinivasan, Brian W Pogue, Shudong Jiang, Hamid Dehghani, and Keith D Paulsen. Spectrally constrained chromophore and scattering near-infrared tomography provides quantitative and robust reconstruction. *Applied optics*, 44(10):1858–1869, 2005.

Peter F. Stadler. Genotype-phenotype maps.

C.V. Stewart. Robust parameter estimation in computer vision. *SIAM Review (Society for Industrial and Applied Mathematics)*, 41:513–537, 1999.

I.B. Styles, A. Clacagni, E. Claridge, F. Orihuela-Espina, and J.M. Gibson. Quantitative analysis of multispectral fundus images. *Medical Image Analysis*, 10(4):578–597, 2006.

T. Tarvainen, M. Vauhkonen, V. Kolehmainen, and J. P. Kaipio. Finite element model for the coupled radiative transfer equation and diffusion approximation. *International journal for numerical methods in engineering*, 65(3):383–405, 2006.

Valery Tuchin. *Tissue Optics: Light Scattering methods and Instruments for Medical Diagnosis*. SPIE PRESS, 2000.

J. Turnay, N. Olmo, J. G. Gavailanes, and M. A. Lizarbe. Collagen metabolism in human colon adenocarcinoma. *Connective Tissue Research*, 23:251–260, 1989.

H. C. Van de Hulst. A new look at multiple scattering. Technical report, NASA Institute for Space Studies, New York, 1962.

H. C. Van De Hulst. *Light Scattering by Small Particles*. Dover Publications, Inc., New York, 1981.

H. C. Van de Hulst and K. Grossman. *Multiple light scattering in planetary atmospheres*. Gordon and Breach Science Publishers Inc, New York, 1968.

M. J. C. Van Gemert, S. L. Jacques, H. J. C. M. Sterenborg, and W. M. Star. The optics of human skin. *IEEE Transactions on Biomedical Engineering*, 36(12):1146–1154, 1989.

P. Walstra and R. Jenness. *Dairy Chemistry and Physics*. John Wiley and Sons, New York, 1984.

L. Wang, S.L. Jacques, and L. Zheng. MCML - Monte Carlo modeling of light transport in multi-layered tissues. *Computer Methods and Programs in Biomedicine*, 47:131–146, 1995.

L. V. Wang and H. I. Wu. *Biomedical Optics: Principles and Imaging*. John Wiley, 2007.

Lihong Wang and Steven L. Jacques. *Monte Carlo Modeling of Light Transport in Multi-layered Tissues in Standard C*.

Q. Wang, H. Yang, A. Agrawal, N.S. Wang, and T.J. Pfefer. Measurement of internal tissue optical properties at ultraviolet and visible wavelengths: Development and implementation of a fiberoptic-based system. *Optics Express*, 16(12):8685–8703, 2008.

L Ward, A Nag, and L C W Dixon. Hill-climbing techniques as a method of calculating the optical constants and thickness of a thin metallic film. *Journal of Physics D: Applied Physics*, 2(2):301, 1969. URL `http://stacks.iop.org/0022-3727/2/i=2/a=419`.

Thomas Weise. *Global Optimization Algorithms - Theory and Application*. Thomas Weise, 2007-05-01 edition, 2007.

A. J. Welch and M. C. J. Van Gemert, editors. *Tissue Optics*. Academic Press, New York (1992), 1992.

Q.R. Williams and J.A. Noble. A spatio-temporal analysis of contrast ultrasound image sequences for assessment of tissue perfusion. In *MICCAI (2)*, pages 899–906, 2004.

Q.R. Williams, J.A. Noble, A. Ehlgen, and H. Becher. Tissue perfusion diagnostic classification using a spatio-temporal analysis of contrast ultrasound image sequences. In *IPMI*, pages 222–233, 2005.

Wiscombe. Doubling initialization revisited, w. j. *J. Quant. Spectrosc. Radiat. Transfer*, 18:245–248, 1977a.

W. J. Wiscombe. On initialization, error and flux conservation in the doubling method. *J. Quant. Spectrosc. Radiat. Transfer*, 16:637–658, 1976.

W. J. Wiscombe. The delta-M method: Rapid yet accurate radiative flux calculations for strongly asymmetric phase functions. *J. Atmos. Sci.*, 34:1408–1422, 1977b.

I. V. Yaroslavsky, A. N. Yaroslavsky, T. Goldbach, and H. J. Schwarzmaier. Inverse hybrid technique for determining the optical properties of turbid media from integrating-sphere measurements. *Applied Optics*, 35:6797–6809, 1996.

K. M. Yoo, Feng Liu, and R. R. Alfano. When does the diffusion approximation fail to describe photon transport in random media? *Phys. Rev. Lett.*, 64:2647–2650, May 1990.

Y. Yuan. Step-sizes for the gradient method. *AMS/IP Studies in Advanced Mathematics*, 42:785, 2008.

D. Yudovsky and L. Pilon. Retrieving skin properties from in vivo spectral reflectance measurements. *Applied Optics*, 4:305–314, 2011.

Deniz Yuret and Michael de la Maza. Dynamic hill climbing: Overcoming the limitations of optimization techniques. In *The Second Turkish Symposium on Artificial Intelligence and Neural Networks*, 1993.

George Zonios, Julie Bykowski, and Nikiforos Kollias. Skin Melanin, Haemoglobin, and Light Scattering Properties Can Be Quantitatively Assessed In Vivo using Diffuse Reflectance spectroscopy. *Investigative Dermatology*, 117:1452–1457, 2001.